Mechanical Response of Lattice Structures under High Strain-Rate and Shock Loading

Thesis by
John S. Weeks

In Partial Fulfillment of the Requirements for the
Degree of
Doctorate of Philosophy in Mechanical Engineering

Caltech

CALIFORNIA INSTITUTE OF TECHNOLOGY
Pasadena, California

2023
Defended September 9, 2022

ACKNOWLEDGEMENTS

I will fondly recall the years I have spent at Caltech and the people I met during my time at this institute. The culture and community here have given me countless opportunities to learn and grow as a researcher and person, for which I will always be grateful. The work conducted in this thesis would not have been possible without the help of many individuals.

First and foremost, I would like to thank my advisor, Guruswami Ravichandran, for his support and mentorship. I deeply appreciate not only the academic freedom and advice that Ravi has given me over the course of my PhD but also the conversations we have had about life outside of the lab. I would not have been able to accomplish this without his guidance and positive perspectives after a failed experiment or confusing result. It has been an absolute pleasure working with and learning from Ravi, especially through the experimental mindset of "Just do it!"

I would also like to thank Kaushik Bhattacharya for his additional advising and support. Our combined Ravi/Kaushik group meetings were always a highlight of my week. These meetings made me a better researcher and taught me to truly enjoy presenting my work. It was reassuring to know Kaushik's door was open just down the hall and I always appreciated and enjoyed our conversations and interactions.

I would like to thank my other committee members: Nadia Lapusta and Ares Rosakis for serving in this capacity and providing valuable feedback on my thesis. Nadia and Ares have also been a large part of my introduction and background to the field of mechanics; Nadia, through teaching multiple courses in solid mechanics, and Ares for whom I was a teaching assistant in continuum mechanics.

The Ravi/Kaushik group has been an incredible group of people who provided their support and feedback over the years. Vatsa Gandhi, Andy Akerson, and Suraj Ravindran have been a large part of my journey since the beginning and have been

ABSTRACT

Lattice structures are a class of architected cellular materials composed of similar unit cells with structural components of rods, plates, or sheets. Current additive manufacturing (AM) techniques allow control and tunability of unit cell geometries, which enable lattice structures to demonstrate exceptional mechanical properties such as high stiffness- and strength-to-mass ratios and energy absorption. Lattice structures exist on two length scales corresponding to the unit cell and continuum material, and therefore demonstrate mechanical behavior dependent on structural geometry and base material. These effects extend to the dynamic regime where lattice structures demonstrate distinct deformation modes under varying strain-rate loading. Experimental investigation of the dynamic and shock compression behavior of lattice structures remains largely unstudied and is the central focus of this thesis where the *high strain-rate*, *transient dynamic*, and *shock compression* behaviors of different topologies of lattice materials are explored.

The first part of this thesis investigates the *high strain-rate* behavior of lattice structures via polymeric Kelvin lattices with rod- and plate-based geometries and relative densities of 15-30%. High strain-rate behavior is characterized by deformation modes similar to that of low strain-rate behavior. High strain-rate experiments ($\dot{\epsilon} \approx 1000 s^{-1}$) are performed and validated using a viscoelastic polycarbonate split-Hopkinson (Kolsky) pressure bar system coupled with high-speed imaging. Both low and high strain-rate experiments show the formation of a localized deformation band which initiates in the middle of the specimen. Strain-rate effects of lattice specimens are observed to correlate with effects of the base polymer material and mechanical properties depend strongly on the relative density of the lattice specimen and exhibit distinct scaling with geometry type (rod, plate) and loading rate despite a similar unit cell shape. Explicit finite element simulations with a tensile failure material model are then used to validate deformation modes and scaling/property trends, and match those observed in experiments.

The second part of this thesis explores the *transient dynamic* and transition to *shock compression* behavior of lattice structures using polymeric lattices with cubic, Kelvin, and octet-truss topologies with relative densities of about 8%. Transient dynamic behavior is characterized by a compaction wave initiating at an impact surface and additional deformation bands with modes similar to low strain-rate modes of deformation. Dynamic testing is conducted through gas gun direct impact

experiments (25 – 70 m/s) with high-speed imaging coupled with digital image correlation (DIC) and a polycarbonate Hopkinson pressure bar. Full-field DIC measurements are used to characterize distinct mechanical behaviors induced by topology such as elastic wave speeds, deformation modes, and particle velocities. At lower impact velocities, a transient dynamic response is observed. At higher impact velocities, shock compression behavior occurs and is characterized by a sole compaction wave initiating and propagating from the impact surface of the lattice. One-dimensional continuum shock theory with Eulerian forms of the Rankine-Hugoniot jump conditions is used with full-field measurements to quantify a non-steady shock response and the varied effect of topology on material behaviors.

The final part of this thesis examines the steady-state *shock compression* behavior of lattice structures through stainless steel 316L (SS316L) octet-truss lattices with relative densities of 10-30%. Powder gun plate impact experiments (270 – 390 m/s) with high-speed imaging and DIC are conducted and reveal a two-wave structure consisting of an elastic precursor wave and a planar compaction (shock) wave. Local shock parameters of lattice structures are defined using full-field DIC measurements and a linear shock velocity (u_s) versus particle velocity (u_p) relation is found to approximate measurements with a unit slope and linear fit constant equal to the crushing speed. One-dimensional continuum shock analysis is again performed using Eulerian forms of the Rankine-Hugoniot jump conditions to extract relevant mechanical quantities. Explicit finite element simulations of the lattice specimens using the Johnson-Cook constitutive model exhibit similar shock behavior to experiments. The simulations reveal a linear $u_s - u_p$ relation and corresponding Hugoniot calculations agree with experimental trends. Notably, 1D shock theory is applied to simulations without resorting to a $u_s - u_p$ relation for the base material, which characterizes this deformation regime and compaction wave as a 'structural shock.'

Major contributions of this thesis include experimental demonstration of ranged strain-rate behaviors for lattice structures of various base materials and topologies including low strain-rate, high strain-rate, transient dynamic, and shock compression regimes; use of full-field quantitative visualization techniques for local mechanical behavior and shock analysis; and finally, characterization of a 'structural' shock compression regime in lattice structures.

PUBLISHED CONTENT AND CONTRIBUTIONS

[1] J.S. Weeks and G. Ravichandran. "High strain-rate compression behavior of polymeric rod and plate Kelvin lattice structures." *Mechanics of Materials* 166 (2022): 104216, doi:10.1016/j.mechmat.2022.104216

Contributions: J.S.W participated in the conception of the project, designed and fabricated specimens, designed and conducted experiments, performed the numerical simulations, analyzed the data, and wrote the manuscript.

[2] J.S. Weeks, and G. Ravichandran. "Effect of topology on transient dynamic and shock response of polymeric lattice structures." Submitted to: *Journal of Dynamic Behavior of Materials* (2022)

Contributions: J.S.W participated in the conception of the project, designed and fabricated specimens, designed and conducted experiments, analyzed the data, and wrote the manuscript.

[3] J.S. Weeks, V. Gandhi, and G. Ravichandran. "Shock compression behavior of stainless steel 316L octet-truss lattice structures." *International Journal of Impact Engineering* 169 (2022): 104324, doi:10.1016/j.ijimpeng.2022.104324

Contributions: J.S.W participated in the conception of the project, designed specimens, participated in designing and conducting of experiments, performed the numerical simulations, analyzed the data, and wrote the manuscript.

TABLE OF CONTENTS

LIST OF ILLUSTRATIONS

LIST OF TABLES

Chapter 1

INTRODUCTION

1.1 Motivation

Cellular materials have long been used by engineers across a range of industries including automotive, aerospace, and biomedical for a variety of applications such as thermal insulation and heat exchangers, packaging, crash energy absorption, vibration damping, implants, and lightweight structural materials [1–8]. Cellular materials are composed of space-filling unit cells with solid edges or faces and with relatively low densities which allows them to realize engineering design space typically inaccessible to fully dense materials. Under compressive loading, these types of materials demonstrate crushing deformation at low internal stresses which makes them desirable for dynamic applications such as impact mitigation and energy absorption [1].

Architected cellular materials with engineered microstructures [9, 10] have emerged in recent years as an exciting new class of materials due to advancements in additive manufacturing (AM) [11]. Control of material microstructure on small (nm, mm) length scales allows design and tunability of mechanical properties of cellular solids for engineering applications on relevant length scales (cm, m) to the designer.

Lattice structures are a class of architected cellular material composed of periodic unit cells with structural components such as rods, plates, or shells [4, 12–15]. Figure 1.1 shows examples of rod-based lattice structures with octet-truss and Kelvin unit cells which exist on two length scales corresponding to the structural length scale of the unit cell and bulk material length scale of the solid. Through careful design of unit cell microstructure, lattice structures demonstrate superior mechanical properties such as stiffness and yield strength over conventional cellular materials such as stochastic foams [4, 16]. Modern computational design techniques and manufacturing capabilities have greatly expanded the design space of lattice structures and make them prime material candidates for lightweight strength, multifunctional, and dynamic engineering applications.

Under dynamic loading, materials support elastic, plastic, and shock waves as well as mechanical phenomena such as strain-rate stiffening and strain-rate strengthening [17]. These phenomena exist too in cellular materials [18], however, their inherent
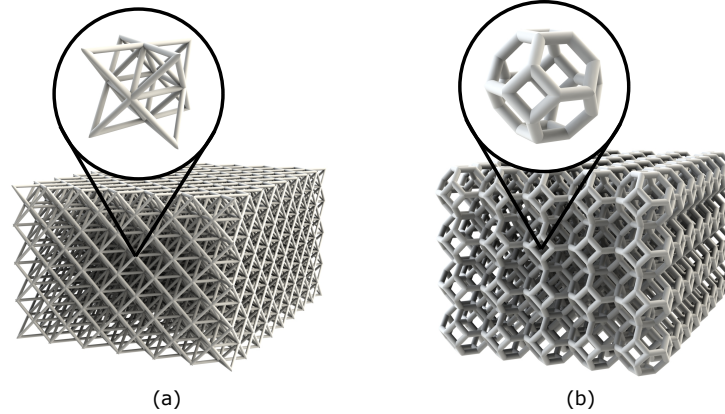
Figure 1.1: Rod-based lattice structures with (a) octet-truss and (b) Kelvin unit cell topologies.

structural nature also induces mechanical effects related to unit cell architecture in addition to effects of the base material. Deformation behavior in cellular materials varies depending on strain-rate, base material, and structure, and it is important to understand the contributions and coupling of these factors, including the role of architected structures on the macroscopic mechanical response. Experimental investigation of the dynamic and shock compression behavior of lattice structures remains largely unstudied and is the central focus of this thesis.

1.2 Background

1.2.1 Classification of Lattice Structures

Lattice structure topology may be rod-based, plate-based, or sheet-based with examples shown in Fig. 1.2. Rod-based lattice structures may be classified into *bending-dominated* or *stretching-dominated* structures based upon deformation mechanism of the unit cells. The deformation mechanism of a unit cell may be determined using structural analysis and Maxwell's stability criterion [19] in three dimensions given by:

$$M = b - 3j + 6, \tag{1.1}$$

where M determines whether a structure is a mechanism (i.e., has more than one degrees of freedom), b is the number of struts, and j is the number of joints. This relation may be further generalized with the concept of self-stress [20]:

$$M = b - 3j + 6 = s - m, \tag{1.2}$$

where s is the number of states of self-stress, and m is the number of mechanisms.

When $M < 0$, the structure behaves as a mechanism with one or more degrees of freedom and is representative of the behavior of open-cell foams. Deformation will occur through bending of unit cell members which is demonstrated by the Kelvin geometry shown in Fig. 1.2(a) and the structure is classified as "bending-dominated."

When $M \geq 0$ and a load or displacement is applied to the structure, a state of self-stress (stress within members of the unit cell) is induced. Tensile or compression forces act within members and the structure is thereby classified as "stretching-dominated" and rigid. The mechanics of stretching-dominated and bending-dominated structures are further discussed in Section 1.2.3.

Maxwell's stability criterion is a necessary, but not a sufficient condition; this is demonstrated for M = 0 where there may be many states of self-stress and mechanisms that are equal in number but not zero. It has been shown by Desphande et al. [16] that a node connectivity of $Z = 12$ is a necessary and sufficient condition for stretching-dominated behavior in a 3D framework such as with the octet-truss unit cell shown in Fig. 1.2(b).

(a) **Rod-based:** Bending-dominated
(Kelvin)

(c) **Plate-based**
(Kelvin)

(b) **Rod-based:** Stretching-dominated
(Octet-Truss)

(d) **Sheet-based**
(Gyroid)
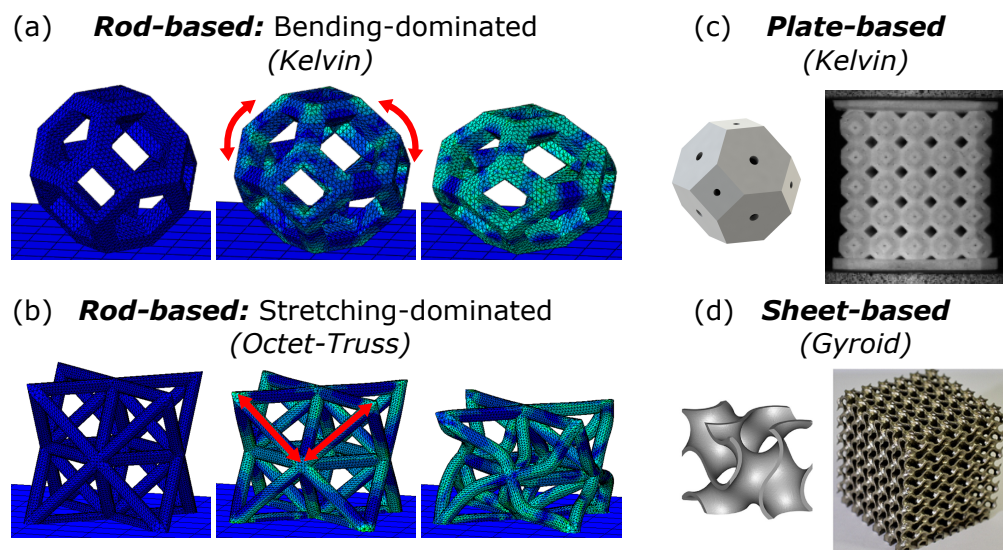
Figure 1.2: Examples of various lattice structure topology: (a) rod-based bending-dominated Kelvin unit cell, (b) rod-based stretching-dominated octet-truss unit cell, (c) plate-based Kelvin lattice structure, and (d) sheet-based gyroid lattice structure [21].

Plate-based and sheet-based lattice structures have been realized and gathered recent research interest due to superior stiffness and strength properties compared to rod-based counterparts [21–25]. Plate-lattices have been shown to computationally attain [26] the Hashin-Shtrikman [27] bounds for stiffness of isotropic materials,

which has been experimentally realized using glassy nanolattices [28]. An example of a plate-based topology is the plate-Kelvin lattice structures shown in Fig. 1.2(c) which is designed by placing plate-like structures along the faces of a Kelvin unit cell.

Sheet-based lattice structures have also been experimentally and computationally realized to show superior mechanical properties to their rod-based counterparts [25, 29]. An example of this type of lattice is the gyroid geometry [21] shown in Fig. 1.2(d). Plate-lattices and sheet-lattices may also be characterized as stretching-dominated or bending-dominated structures through determination of their scaling coefficents of stiffness and initial yield strength with relative density, which is discussed in Section 1.2.3.

1.2.2 Additive Manufacturing Techniques

Additive manufacturing (AM), or 3D printing, has greatly advanced in the last decade in terms of print resolution, manufacturing speed, build volume, and material variety [30]. AM permits complex designs by manufacturing components in a layer-by-layer fashion from a computer-aided-design (CAD) model without the need for casting, forging, or machining. The ability to manufacture features on sub-millimeter length scales enables intricate unit cell design and fast build speeds allow realization of lattice structures with relevant engineering dimensions, $O(cm)$. AM includes techniques on the nano-scale such as electron beam lithography, microstereolithography, and two-photon polymerization with feature resolution down to 100 nm which has also enabled studies of nano-architected materials [31].

The International Organization for Standardization (ISO)/American Society for Testing and Materials (ASTM) 52900:2021 classifies AM into seven categories: binder jetting, direct energy deposition, material extrusion, material jetting, powder bed fusion, sheet lamination, and vat polymerization. These techniques enable manufacturing of polymers, ceramics, composites, metals, as well as hybrid combinations with typical build volumes ranging from 200x200x200 mm^3 to 1x1x1 m^3 [11]. Work in this thesis utilizes digital light processing vat polymerization and direct metal laser sintering powder bed fusion technologies to manufacture polymeric and metallic lattice structures on the centimeter length scale.

Vat polymerization (VP) entails polymerization of a liquid light-curable photoresin into solid photopolymer through exposure to ultraviolet (UV) light and resultant cross-linking of polymer chains [32]. VP technologies are classified according to

the method of curing: two common technologies are stereolithography (SLA) and digital light processing (DLP). SLA uses a point-based laser to trace out and cure a printing layer while DLP uses a digital light projector to cure a full layer at once. Due to a larger projected light source, DLP printers offer higher speeds than SLA printers. Both these techniques may be performed using desktop 3D printers at a low cost and are effective for rapid prototyping of materials. A large drawback of VP is poor mechanical properties of photopolymer material; for example, specimens in this thesis demonstrated properties such as swelling from submersion in isopropyl alcohol baths and embrittlement due to drying.

Powder bed fusion (PBF) enables AM of metallic materials by fusing thin layers of powder onto a build plate using a point-based energy source such as a laser or electron beam [33]. PBF can be categorized into melting and sintering technologies based upon the strength of the energy source and whether the powder fully melts during the manufacturing process. Technologies include electron beam melting (EBM), selective laser melting (SLM), selective laser sintering (SLS), and direct metal laser sintering (DMLS). In contrast to melting, sintering does not fully melt the powder; SLS is used as a general term and may be used to form structures made of plastics, glasses, or ceramics, while DMLS refers to sintering using metallic alloys [34]. The melting/sintering process introduces microstructural effects on grain sizes and shapes in the material–as a result, there is currently a large research focus on these effects and characterization of AM metals which demonstrate different mechanical properties than conventionally manufactured counterparts [35–37].

1.2.3 Low Strain-Rate Behavior of Lattice Structures

Cellular solids are characterized by relative density, ρ^*/ρ_s: the density of the cellular material (ρ^*) divided by the density of the base material (ρ_s), or similarly, the volume of actual material divided by the space-filling volume of the solid. When loaded, cellular materials exhibit an initial linear elastic regime followed by plastic yield, fracture, or buckling of cell walls determined by unit cell topology and base material. After yield, cellular materials subsequently show a crushing deformation at a relatively constant plateau stress until densification, and eventual contact of cell walls causes steep stiffening. A generalization of this stress-strain response is shown schematically in Fig. 1.3(a).

Conventional scaling laws for bending-dominated and stretching-dominated lattice structures may be derived through simple mechanical arguments found in Gibson

and Ashby [1] and Ashby [4]. Scaling laws for bending-dominated structures are derived by considering an open-cell foam as a cubic array with members of length, L, and square cross-sectional thickness, t, as shown in Fig. 1.3(b). Typical bending-dominated deformation is illustrated through the dashed blue lines.
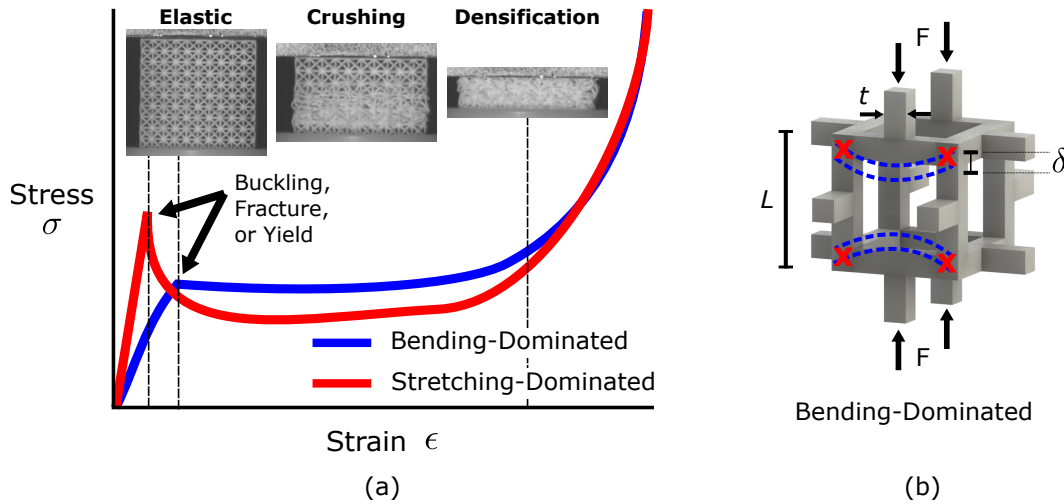
Figure 1.3: General mechanical behavior of lattice structures: (a) general stress-strain response and (b) simple cubic foam used for modeling bending-dominated scaling laws.

A first-order approximation for relative density of the cubic foam (including double-counting at edges) is calculated by considering the total volume of the strut members ($V^* = 12Lt^2$) and space-filling volume of the cube ($V_{space} = L^3$) such that:

$$\rho^*/\rho_s = V^*/V_{space} \propto (t/L)^2 . \tag{1.3}$$

Based on Eq. (1.3), dimensional analysis of mechanical properties using L and t allows relation of these properties to relative density.

Given a nominal compressive stress acting on the unit cell, σ, a corresponding force, $F \propto \sigma L^2$ is exerted and produces a bending deflection, δ. Following standard beam theory [38], the displacement, δ, is proportional to $\delta \propto FL^3/(E_s I)$ where E_s is the Young's modulus of the strut material and I is the second moment of area of the strut where $I \propto t^4$ in a square cross-section with dimension t. The strain in the cell, ϵ, is related to the displacement $\epsilon \propto \delta/L$. A relation for the stiffness of a bending-dominated open-cell foam, E^*_{bend}, is therefore given by:

$$E^*_{bend} = \sigma/\epsilon \propto E_s(t/L)^4 \propto E_s(\rho^*/\rho_s)^2 . \tag{1.4}$$

Collapse of this structure occurs through plastic hinges developing at the locations marked 'X' in Fig. 1.3(b). Plastic moment, M_p, of a square cross-section beam is given by $M_p = \sigma_y(t^3/4)$ where σ_y is the yield strength of the strut material, which is assumed to be elastic-perfectly plastic. Assuming the plastic moment is related to the stress implies $M_p \propto FL \propto \sigma L^3$, then the plastic yield stress of the open-cell structure may be found:

$$\sigma_{bend}^* \propto \sigma_y(t/L)^3 \propto \sigma_y(\rho^*/\rho_s)^{3/2}\,. \tag{1.5}$$

Base material of the cellular solid plays a role in the mechanical response through the elastic modulus, E_s, and yield stress, σ_y. This agrees with intuition that a metallic foam would demonstrate a stiffer and stronger response than a polymeric or elastomeric foam.

Similar dimensional analysis may be carried out on stretching-dominated structures. Since there are no mechanisms in a stretching-dominated structure, it is assumed that struts are loaded and fail in tension or compression, and therefore the stiffness and yield stress are related to average properties of a strut member and scale linearly with relative density. The structure is initially loaded by elastic stretching of the struts, followed by yield of one or more sets of struts [4].

This may be interpreted by considering volume fraction of the lattice. As volume fraction increases in each strut (i.e., the unit cell approaches full density), the stiffness and yield stress will increase. The relative stiffness and yield for a stretching-dominated structure scale linearly such that:

$$E_{stretch}^* \propto E_s(\rho^*/\rho_s)\,, \tag{1.6}$$

$$\sigma_{stretch}^* \propto \sigma_y(\rho^*/\rho_s)\,. \tag{1.7}$$

This linear scaling behavior has been demonstrated analytically for the octet-truss topology by Deshpande et al. [39] who expressed the stiffness along the normal direction to the front face as $E^* = E_s(\rho^*/\rho_s)/9$ and experimentally on the μm scale by Al-Ketan et al. [40] with a scaling coefficient of 1.16. Al-Ketan et al. noted the deviation from 1 may be attributed to non-rigid node geometries which have also been demonstrated to affect the mechanical behavior of lattice structures by Portela et al. [41]

The scaling law coefficients for both types of structures demonstrate an increased stiffness and initial yield strength of a stretching-dominated over bending-dominated structure; (stiffness: stretching = 1 vs. bending = 2; yield strength: stretching = 1 vs. bending = 3/2). However, stretching-dominated structures also show post-yield softening illustrated in Fig. 1.3(b) such as post-buckling softening. A lower scaling exponent with relative density reflects a less severe decrease in stiffness and initial yield strength as relative density decreases. The general behavior of these structures demonstrates stretching-dominated lattices are effective for lightweight strength and offer improved behavior at lower relative densities. However, bending-dominated structures, while they may show a lower stiffness and initial yield strength, are better for applications of energy absorption due to a constant crushing strength and absence of post-yield softening.

1.2.4 High Strain-Rate Behavior of Lattice Structures

The high strain-rate behavior of lattice structures has been explored for a variety of topologies and strain-rates and exhibits a dependency on both the geometry and base material. Some examples of this coupled behavior for metallic and polymeric lattice structures follow.

Metallic Ti-6Al-4V lattice structures have demonstrated strain-rate strengthening which agrees with effects observed in bulk AM Ti-6Al-4V [42], but also show dependence on geometry such as increased strain-rate effects in smaller unit cell sizes [43], increased strain-rate effects in specimens with multiple layers of unit cells (opposed to a single layer), and consistent effects with the behavior of bulk material in graded specimens [44]. Inconel 718 lattice structures with similar microstructures have demonstrated effects related to heat-treatment of the base material and strain-rate independent deformation trends related to flow stress enhancement [45]. Stainless steel 316L (SS316L) octet-truss lattice structures have demonstrated strain-rate strengthening [46] and hollow strut SS316L lattices have shown varying strain-rate sensitivities depending on the microstructure [47]. Considering polymers, octet-truss lattice structures made of two types of polymer material with the same AM technology have demonstrated strain-rate effects in one material, but not the other [48].

While for some metallic lattices the deformation modes do not change under dynamic loading [43, 46], polymer plate-like Kelvin lattices have demonstrated varying position of deformation bands dependent upon loading rate [49]. It is apparent

the geometry, base material, and their coupled behavior plays a large role in the dynamic response and strain-rate sensitivities of lattice structures. But, while many case studies like these exist for the dynamic response of lattice structures, a relatively unexplored regime is their shock compression behavior.

Shock Compression Behavior

Under high velocity impact loading, cellular solids demonstrate a compaction front that propagates from the impact surface along the direct of impact as seen in Fig. 1.4. This compaction front is the densification of material as the structure is compressed and the cell walls are pressed into each other. This compaction wave is modeled as a 'shock' wave initially proposed by Reid and Peng [50] for the dynamic crushing of wood.

It has been established that shocks form in cellular materials when impacted above some critical velocity [18, 51, 52] which has been demonstrated in honeycombs [53], open-cell aluminum foams [54, 55], and more recently, lattice structures [56–61].

Reid and Peng [50] initially proposed a model with a rigid-perfectly-plastic-locking (RPPL) response which assumes rigid (no elastic), perfectly plastic deformation behavior with the strain behind the compaction front as a constant value. This RPPL model was later extended to model the shock response of closed-cell aluminum foams [62, 63] and has also been extended in contexts to elastic (elastic-perfectly-plastic-locking) [64] and linear plastic hardening (rigid-linear-hardening-plastic-locking) [52] behaviors. This uniform (locked) strain behind the shock is a key assumption for utilizing one-dimensional uniaxial planar shock theory.
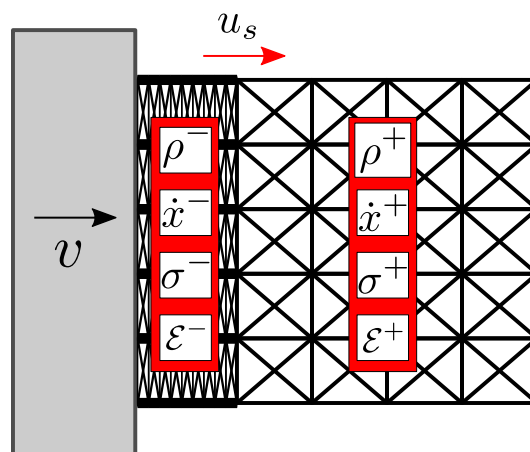
Figure 1.4: Schematic of shock wave in lattice structure.

One-dimensional uniaxial planar shock theory recognizes a shock wave as a discontinuity in field variables in the material [17, 65] illustrated in Fig. 1.4. This may be most intuitively recognized in cellular materials by considering density. 1D shock theory relies on the conservation of mass, momentum, and energy to determine field variables of density (ρ), particle velocity ($\dot{x}$), stress (σ), and specific internal energy ($\mathcal{E}$) in a material without resorting to a constitutive relation.

Integral forms of the conservation of mass, momentum, and energy may be expressed in terms of quantities behind and ahead of the shock using Rankine-Hugoniot jump relations. These relations may be derived in both the Lagrangian (undeformed, X) and Eulerian (deformed, x) coordinates and are shown for Eulerian coordinates in Eqs. (1.8), (1.9), and (1.10) which represent the conservation of mass, momentum, and energy, respectively:

$$\llbracket \rho \rrbracket u_s = \llbracket \rho \dot{x} \rrbracket , \tag{1.8}$$

$$\llbracket \rho \dot{x} \rrbracket u_s = \llbracket \rho \dot{x}^2 - \sigma \rrbracket , \tag{1.9}$$

$$\llbracket \rho \left(\mathcal{E} + \frac{1}{2} \dot{x}^2 \right) \rrbracket u_s = \llbracket \rho \left(\mathcal{E} + \frac{1}{2} \dot{x}^2 \right) \dot{x} - \sigma \dot{x}^2 \rrbracket . \tag{1.10}$$

In typical conventional shock analysis, assumption of quantities ahead of the shock, measurement of one field variable, a relation between shock speed (u_s) and one field variable such as particle velocity ($\dot{x}$) (a Hugoniot relation), and the three conservation equations are used to determine the state of the shock compressed material. However, variations of this analysis exist and it will be shown in this thesis that the state ahead of the shock in lattice structures is non-quiescent and full-field measurements of field variables ahead of the shock may be used to carry out full characterization.

1.3 Thesis Outline

This thesis presents an exploration of the compressive mechanical response of lattice structures under high strain-rate and shock loading investigated primarily through experiments and supplemented with numerical simulations. A range of strain-rates, lattice topologies, and lattice base materials are investigated and chapters are presented in order of increasing strain-rate (Fig. 1.5).

In Chapter 2, the high strain-rate behavior of rod and plate-based polymeric Kelvin lattice structures is studied. Experimental methods for design and manufacturing, low strain-rate testing, and high strain-rate testing of lattice structures using a poly-

carbonate split-Hopkinson (Kolsky) pressure bar technique are presented along with corresponding numerical simulations. The strain-rate behavior of lattice specimens is analyzed with respect to the base material and mechanical failure properties using experimental and simulation results.

In Chapter 3, the behavior of polymeric lattice structures is explored at higher strain-rates. The transient dynamic and shock response of polymeric lattice structures with Kelvin, octet-truss, and cubic topologies is studied experimentally using direct impact experiments with a polycarbonate Hopkinson pressure bar coupled with high-speed imaging. Mechanical properties and deformation behaviors are extracted using full-field measurements and the transition to shock-like behavior in lattice structures is examined.

In Chapter 4, the shock compression behavior of stainless steel 316L octet-truss lattice structures at high impact velocities is investigated using experiments and numerical simulations. Powder gun plate impact experiments with high-speed imaging and digital image correlation are used to define and analyze the shock compression response of lattice structures. Numerical simulations are carried out to validate experimental results and further study the mechanical response of a 'structural shock.'

Finally, Chapter 5 provides a summary of the work and future outlook on research in this field.
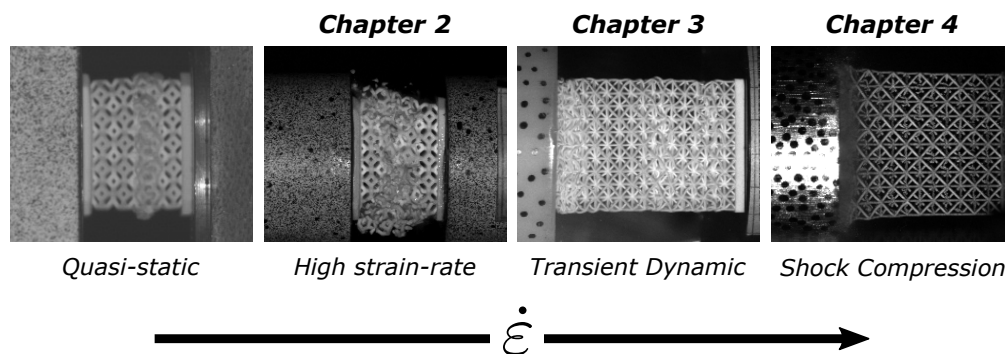
Figure 1.5: Illustration of response of lattice structures explored in successive chapters of this thesis with increasing strain-rate.

Chapter 2

HIGH STRAIN-RATE COMPRESSION BEHAVIOR OF POLYMERIC ROD AND PLATE LATTICE STRUCTURES

Contributions: J.S.W participated in the conception of the project, designed and fabricated specimens, designed and conducted experiments, performed the numerical simulations, analyzed the data, and wrote the manuscript.

Abstract

The compressive high strain-rate behavior of polymeric Kelvin lattice structures with rod-based and plate-based unit cells is investigated through experimental techniques and finite element simulations. Polymeric lattice structures with 5x5x5 unit cell geometries are manufactured on the millimeter scale using vat polymerization additive manufacturing and tested at low ($0.001\ s^{-1}$) and high ($1000\ s^{-1}$) strain-rates. High strain-rate experiments are performed and validated for a viscoelastic split-Hopkinson (Kolsky) pressure bar system (SHPB) coupled with high-speed imaging and digital image correlation (DIC). Experimental results at both low and high strain-rates show the formation of a localized deformation band which is more prevalent in low relative density specimens and low strain-rate experiments. Strain-rate effects of lattice specimens strongly correlate with effects of the base polymer material; both bulk polymer and lattice specimen demonstrate strain-rate hardening, strain-rate stiffening, and decreased fracture strain under dynamic loading. Results show mechanical failure properties and energy absorption depend strongly on the relative density of the lattice specimen and exhibit distinct scaling between relative density, geometry type (rod, plate), and loading rate. High relative density plate-lattices demonstrate inferior mechanical properties to rod-lattices; however, there exists a critical relative density for a given mechanical property (17%-28%) below which plate-lattices outperform rod-lattices of similar mass. Finally, high strain-rate explicit finite element simulations are performed and show good agreement with mechanical failure trends and deformation modes observed in experiments.

2.1 Introduction

Plate-lattices have been shown through simulation and experiment to demonstrate exceptional mechanical properties of stiffness and yield strength and to outperform rod-lattices of equal mass [22–24]. For instance, geometries such as the octet-cubic plate-lattice have computationally attained the theoretical Hashin-Shtrikman (H-

S) [27] upper bounds on isotropic elastic stiffness [26] which has been supported experimentally with pyrolytic carbon octet-cubic nanolattices whose quasi-static stiffnesses and strengths are close to the H-S and Suquet upper bounds [28]. Sheet-lattices have also been shown to outperform particular rod-lattices of equal mass [25, 40] and experiments on milliscale metallic lattices of varying topology show superior mechanical performance in sheet-triply periodic minimal surface (TPMS)-based geometries than rod- or skeletal-TPMS based geometries [21]. Rod-, plate-, and sheet-lattices also appear in nature through biological cellular materials: cancellous bone, toucan beak, and woodpecker cranial skull all exhibit combinations of rod, plate and sheet structures [66–68].

Lattice structure mechanics inherently depend upon lattice topology and base material behavior and many researchers have explored both material and geometric effects. Studies have taken advantage of material size effects on the nanoscale to attain high specific-strengths [69, 70] and flaw insensitivity [71, 72], and geometric effects from node geometry [41] and manufacturing imperfections such as strut waviness or thickness variation [73] have been shown to affect mechanical properties. Geometric defects also affect lattice behavior and defects such as missing struts weaken the mechanical response and demonstrate different strength and stiffness scaling properties than ideal geometries [74, 75].

Dynamic experiments on lattice structures have shown lattice strain-rate behavior is material dependent. Both strain-rate strengthening and weakening effects have been observed in polymeric octet-truss lattice specimens depending on the base material used [48]. Experimental work by Tancogne-Dejean et al. suggests that the dynamic-strengthening effect present in stainless steel 316L octet-truss lattice specimen is attributed to the strain-rate effects of the base material [46]. Hazeli et al. reports dynamic experiments on metallic heat-treated lattice structures that exhibit strain-rate hardening and similar deformation trends at low and high strain-rates for octet-truss, rhombic dodecahedron, and dode-medium unit cells [45]. Experiments on polymeric plate-Kelvin lattices have shown the position of deformation bands can be dependent on strain-rate, with high strain-rate deformation occurring at lattice edges and low strain-rate deformation occurring in the middle of the specimen [49].

The behavior of various rod- and plate-lattices has been individually explored, but not actively compared for a single unit cell geometry under dynamic loading. Low-velocity impact experiments have been carried out on polymeric plate-lattices [76] and high strain-rate experiments have been carried out on a single unit cell
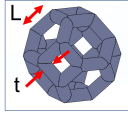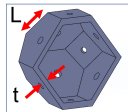
of a metallic plate-lattice [23], but high strain-rate experimental characterization of full plate-lattices is lacking. In this chapter, we perform high and low strain-rate experiments and simulations on polymeric rod- and plate-lattices with a 5x5x5 Kelvin unit cell geometry. Lattice specimens are manufactured using digital light processing (DLP) vat polymerization and loaded at low strain-rates using a servo-hydraulic machine and at high strain-rates using a polycarbonate split-Hopkinson (Kolsky) pressure bar. The mechanical strength and failure properties are extracted and the dynamic effects on lattice specimen are studied. Finally, finite element simulations performed with Abaqus/Explicit are used to complement experiments, which show good qualitative agreement with high strain-rate results.

2.2 Materials and Methods

2.2.1 Specimen Design and Manufacturing

Lattice specimens were designed using rod and plate structures with a Kelvin unit cell [77]. Rod (R) geometries were designed by placing rod structures along the edges of a unit cell and plate (P) geometries were designed by placing plate structures along the faces of a unit cell. Computer-aided design (CAD) models were constructed in SolidWorks (Dassault Systems) using a 5x5x5 Kelvin unit cell geometry composed of rod or plate structures with relative densities of 15%, 20%, 25%, and 30%. Unit cell lengths were kept constant and the thickness of the structural elements was varied to obtain different relative densities. Relative density, ρ^*/ρ_s, was calculated in SolidWorks by taking the volume fraction of each unit cell specimen within a space-filling bounding box. Table 2.1 shows the CAD dimensions for each of the lattice unit cell specimen and the calculated relative densities.

Table 2.1: Dimensions of Kelvin cell characteristic length L, structure thickness t, relative density ρ^*/ρ_s, as-designed mass m_{CAD}, and experimental mass m_{exp} for each lattice specimen.

Specimen: *Rod (R), Plate (P)*		L (mm)	t (mm)	ρ^*/ρ_s (-)	m_{CAD} (g)	m_{exp} (g)
R15		1.10	0.51	0.15	1.48	1.49 ± 0.06
R20		1.10	0.63	0.20	1.80	1.80 ± 0.06
R25		1.10	0.75	0.25	2.16	2.16 ± 0.02
R30		1.10	0.89	0.30	2.58	2.57 ± 0.13
P15		1.25	0.18	0.15	1.64	1.64 ± 0.09
P20		1.25	0.25	0.20	1.93	1.92 ± 0.15
P25		1.25	0.34	0.25	2.20	2.22 ± 0.22
P30		1.25	0.43	0.30	2.45	2.50 ± 0.15

Manufacturing of closed-cell structures remains an active challenge for the AM community. In these plate-like specimens, small holes were placed in the plate faces to avoid trapping of liquid photoresin inside of unit cells. Baseplates were also attached on two opposite faces to improve manufacturability and ensure planar loading during testing.

Specimens (Fig. 2.1) were manufactured using vat polymerization additive manufacturing (3D printing) with Digital Light Processing (DLP) technology. DLP 3D printers utilize a layer-by-layer manufacturing technique to cure liquid photoresin into solid photopolymer using UV light [11]. An Autodesk Ember DLP 3D printer was used with Colorado Photopolymer Solutions PR57-W photoresin. The printer uses a 405 nm wavelength light for 2.8 s exposure time per 25 μm layer. Specific machine parameters are detailed in Appendix A.1.
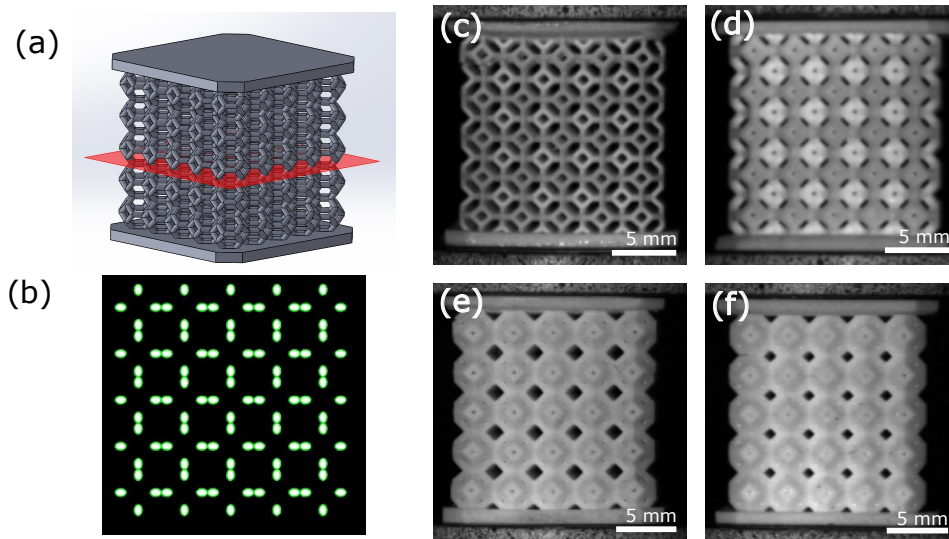
Figure 2.1: Design and manufacture of rod and plate lattice specimens: (a) CAD model of R15 specimen; (b) cross-sectional illumination of DLP manufacturing technique for layer highlighted in (a); manufactured photopolymer lattice specimen with (c) R15, (d) R30, (e) P15, and (f) P30 geometries.

Figure 2.1(b) shows an example of the cross-sectional illumination during printing of a rod specimen. Manufacturing supports were attached to the baseplates to improve print success and later removed. The print build area allowed for two lattice specimens to be printed from one manufacturing run. After fabrication, specimens were rinsed in an isopropyl alcohol bath to remove any excess photoresin. The small holes in plate specimen (square faces – 0.225 mm diameter, hexagonal faces – 0.300 mm diameter) allow uncured photoresin to be removed from the interior of

the unit cells. Lattice dimensions showed around 5% shrinkage from as-designed CAD values in the print direction and < 5% in lateral directions.

The density of the photopolymer was calculated as 1200 kg/m^3 and used to approximate the as-designed masses of each specimen in SolidWorks. The as-designed and average experimental masses with standard deviation for each specimen are listed in Table 2.1. The small difference between masses and low shrinkage demonstrate that the resolution of the printer can resolve the as-designed dimensions and indicate the experimental relative densities are consistent with the as-designed values.

In addition to the lattice structures, bulk photopolymer specimens were printed for mechanical characterization of the base material. Cylindrical specimens with 10 mm diameter and 5 mm width were manufactured using the same print parameters as the lattice specimens.

2.2.2 Low Strain-Rate Experiments

Low strain-rate experiments were performed using a servo-hydraulic actuator machine (MTS Model 358.10) with a 13.3 kN axial load capacity. Lattice specimens were compressed at a rate of 1 mm/min and bulk photopolymer specimen were compressed at a rate of 0.2 mm/min until the load capacity of the machine was reached. These loading rates correspond to a nominal strain-rate of $\dot{\epsilon} \approx 0.001/s$. A Fastec IL5 High-Speed Camera with a 100 mm Tokina AT-X Pro lens was used to take experimental images at 24 frames per second with a continuous light source (Techniquip FOI-150-UL). Images were resampled and analyzed at 1 fps to limit the amount of data collected from the long timescale of the experiment. 2D digital image correlation (DIC) software (Vic2D, Correlated Solutions, Columbia, SC) was used to determine the displacement of the hydraulic crosshead. A random speckle was placed on the crosshead and a subset size of 55 pixels with a step size of 5 pixels was used in the DIC analysis.

2.2.3 High Strain-Rate Experiments

High strain-rate experiments were performed using the split-Hopkinson (Kolsky) pressure bar (SHPB) technique [78]. Figure 2.2 shows a general diagram of the SHPB set-up composed of an impactor, input, and output bar with strain gauge locations. A pressurized gas gun is used to propel the impactor into the input bar which generates a stress wave that compresses the sample between the input and output bars. An 7075 aluminum SHPB system was used for testing of bulk photopolymer specimens and a polycarbonate (PC) system was used for testing

of lattice specimens. A Vishay 2310B signal conditioning amplifier and 2.5 GHz Tektronix DPO 3014 digital oscilloscope were used for both SHPB systems to record raw strain gauge voltage data.
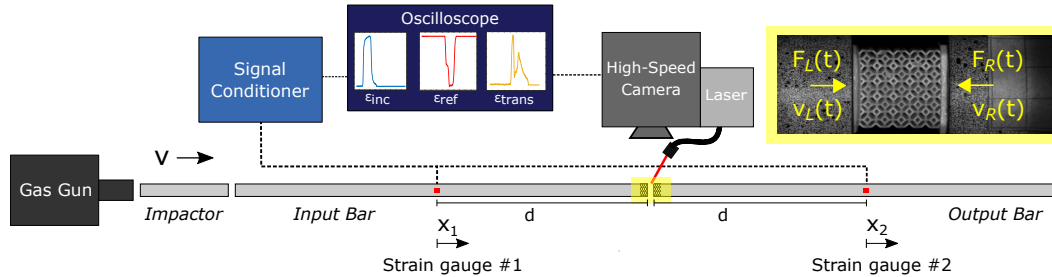
Figure 2.2: Schematic of split-Hopkinson (Kolsky) pressure bar set-up for high strain-rate experiments with example of an experimental image and incident, reflected, and transmitted strain signals shown.

A Shimadzu HPV-X2 camera with a 100 mm Tokina AT-X Pro lens was used to take high-speed images of the lattice during dynamic deformation. A Cavitar Cavilux Smart laser unit was used as a light source to send 20 ns incoherent laser pulses. A field of view of 55 mm x 32 mm (7 pixels/mm) was used to capture 128 images at 100,000 fps. 2D DIC code (Vic2D) was used to extract the displacements and velocities of the input- and output-bar interfaces. A random speckle was applied to the ends of the input and output bars (Fig. 2.2) and low-pass imaging with an average subset size of 35 pixels with a step size of 3 pixels was used in the DIC analysis.

7075 Aluminum SHPB System

The Al 7075 SHPB system consisted of impactor (0.45 m), input (1.83 m), and output (1.83 m) bars of diameter 19.05 mm with Omega SGD-2D/350-LY11 strain gauges (1/4 bridge circuit) located at the midpoints of the bars. Bending effects are eliminated by taking the average of two strain gauges on diametrically opposing sides of the bar. Conventional one-wave SHPB analysis [78] was used to obtain the macroscopic stress-strain response of the test specimen. It is assumed excessive dispersion or attenuation does not occur and no dispersion correction was applied.

Polycarbonate SHPB System

The polycarbonate system consisted of impactor (0.46 m), input (1.83 m), and output (1.83 m) bars of diameter 24.50 mm with Vishay EA-06-031DE-350/LE strain

gauges (1/4 bridge circuit) located at the midpoints of the bars, in a similar arrangement to the Al 7075 system. Due to poor heat conduction in the polycarbonate, the strain gauges were operated at a low input voltage (1.4 V) to avoid thermal drift in measurements. In a viscoelastic medium such as polycarbonate there is considerable dispersion and attenuation of stress waves. Corrections of strain measurements are necessary to extract accurate specimen stress-strain response in a viscoelastic SHPB. A non-conventional SHPB analysis technique is thus required and is briefly described here.

The dispersion and attenuation effects inherent in a viscoelastic medium are corrected by applying a phase shift in the frequency domain to the strain measurements. Following the work of Bacon [79]: the velocities (v) and forces (F) (for some position x) in a viscoelastic SHPB can be written in the frequency domain in terms of angular frequency, $\omega = 2\pi f$, where f is frequency in Hz:

$$\hat{v}(x, \omega) = \frac{-i\omega}{\gamma} [\hat{P}(\omega)e^{-\gamma(\omega)x} + \hat{N}(\omega)e^{\gamma(\omega)x}] \,, \tag{2.1}$$

$$\hat{F}(x, \omega) = \frac{-\rho A \omega^2}{\gamma^2} [\hat{P}(\omega)e^{-\gamma(\omega)x} + \hat{N}(\omega)e^{\gamma(\omega)x}] \,, \tag{2.2}$$

$$\gamma(\omega) = \alpha(\omega) + i\frac{\omega}{c(\omega)} \,. \tag{2.3}$$

$\hat{P}(\omega)$ and $\hat{N}(\omega)$ represent the Fourier transforms of the strains at $x = 0$ (corresponding to the measurement location) due to the waves traveling in the directions of increasing and decreasing x, respectively. $\gamma(\omega)$ is the wave propagation coefficient defined by attenuation coefficient $\alpha(\omega)$ and phase velocity $c(\omega)$. Velocity and force time histories in the bars are obtained using an Inverse Fourier Transform on Eqs. (2.1) and (2.2). The wave propagation coefficient is found using a one-point measurement experimental technique [79] and the average wave propagation coefficient computed over 10 experiments is used in the analysis (see Appendix A.2).

We validate the polycarbonate SHPB by comparing bar-interface velocities computed using SHPB (i.e., Eq. (2.1)) and DIC techniques. Error in measurement is defined in time as the percent difference of the velocity measurements at the bar-interfaces and is propagated onto force measurements. Figure 2.3(a) compares the input bar and output bar interface velocities for a R20 specimen. There is good agreement of peak velocities within $5-8\%$ on the input bar and within $3-4\%$ on the output bar over the course of loading. Considering force equilibrium, Fig. 2.3(b)

shows the incident and transmitted (left and right, respectively) force-time histories of rod specimen. We observe good agreement between the right-interface and left-interface forces for all specimen geometries. This indicates dynamic equilibrium is attained during high strain-rate loading experiments. An improvement in dynamic equilibrium is observed for higher relative density specimen. Additionally, plate specimen demonstrated similar force-time histories to rod specimen.
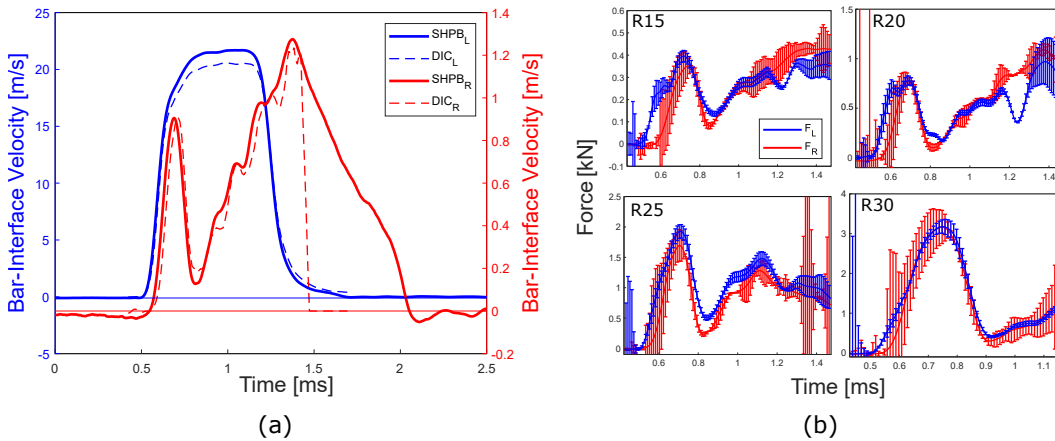
Figure 2.3: Validation of polycarbonate SHPB experimental technique: (a) SHPB-computed and DIC-computed interface velocities of a R20 specimen experiment showing good agreement; and (b) force-time histories of rod specimens of various relative densities (15%, 20%, 25%, 30%) during loading.

2.2.4 Numerical Simulations

Numerical simulations were carried out using Abaqus/Explicit (Dassault Systems, Providence, RI) finite element analysis. The simulation framework included a 5x5x5 lattice specimen geometry compressed between two rigid plates (Fig. 2.4(a)). The bottom plate remained fixed while a constant velocity was applied to the top plate. The velocity was implemented as a smoothed amplitude step during the initial 10% of loading to decrease numerical oscillations. The "Brittle Cracking" Abaqus/Explicit material definition was used; this model assumes linear elastic behavior with damage from tensile cracking. This constitutive relation and the material parameters used in the numerical model were chosen to match the qualitative macroscopic stress-strain response and deformation behavior in dynamic experiments. A critical stress σ_C is defined using values for stiffness, E = 1000 MPa (Young's modulus) and ϵ_C = 0.2 (strain). A linear loss of strength is assumed from ϵ_C up to some ϵ_D = 0.3 (strain) at which the element is removed from the simulation (Fig. 2.4(b)). Mass density was experimentally determined and defined as 1200 kg/m^3 and Poisson's ratio was taken as ν = 0.35, which is a typical value for polymers. A general

contact algorithm was defined for self-contact of the specimen and surface-to-surface contact properties with no normal separation were defined for the rigid plate-lattice interactions. Tetrahedral meshing with a local mesh size of 0.20 mm and quadratic C3D10M elements with deletion was used. Mass scaling was used to increase the computational timestep which corresponded to $< 0.1\%$ percent change in mass for all specimens.
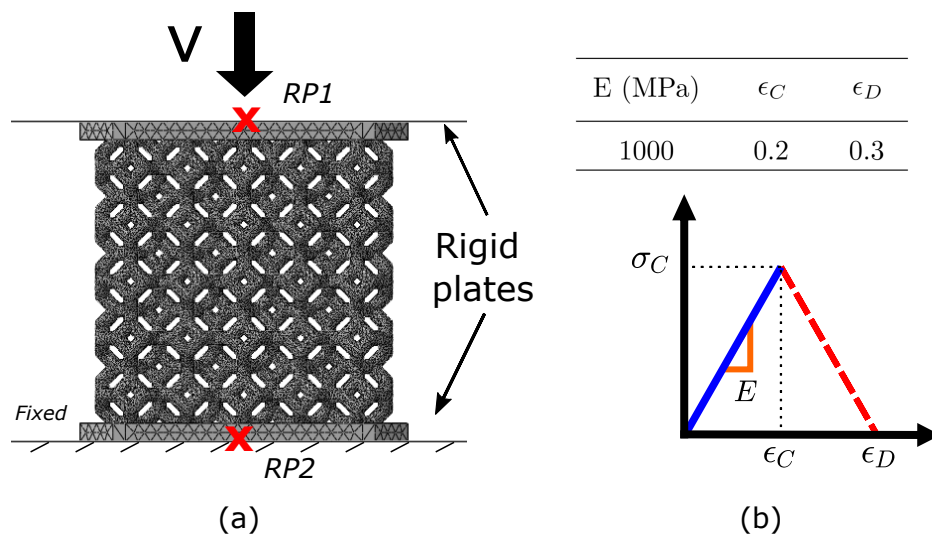
Figure 2.4: Numerical simulation (a) framework with two rigid plates (defined by a reference point RP) and a 5x5x5 lattice specimen imported from SolidWorks; and (b) parameters used in "Brittle Cracking" material model and material response.

2.3 Results and Discussion

2.3.1 Base Material Characterization

The mechanical behavior of lattice structures is known to depend on both the structural unit cell geometry and base material behavior [14, 15]. Therefore, strain-rate characterization of the base photopolymer material is necessary to understand the mechanical response of the lattice specimen. Low strain-rate experiments on bulk photopolymer specimen were performed with a servo-hydraulic MTS testing machine and DIC-computed displacements. High strain-rate experiments were performed using an Al 7075 SHPB system with one-wave analysis [78]. Force equilibrium was observed during high strain-rate experiments and it is assumed the specimens were in dynamic equilibrium.

Figure 2.5 shows the compressive true stress-strain response ($\bar{\sigma} - \bar{\epsilon}$) for the photopolymer at various average strain-rates. Strain-rate was calculated for each specimen using one-wave analysis and taken as the average value from the start of loading until unloading of the stress wave. Specimens experienced approximately

uniform strain-rate for $\bar{\epsilon} > 0.03$. All specimens demonstrated elastic, yielding, and strain-hardening material responses. Strain-rate stiffening in modulus and strain-rate hardening effects are observed. The dynamic enhancement factor D (defined as the ratio of the high strain-rate value over the corresponding low strain-rate value) for material strength for $\dot{\bar{\epsilon}} = 0.001 - 1000/s$ is $D \approx 6$ at strain $\bar{\epsilon} = 0.05$ and $D \approx 3.5$ at $\bar{\epsilon} = 0.10$. Brodnik et al. has performed crack propagation experiments and simulations on a dyed form of the base photopolymer (PR-57 Black) and demonstrated brittle material behavior with a fracture toughness of $0.2\ MPa\sqrt{m}$ [80]. High-speed experimental images revealed fracture of specimens during dynamic testing. Specimens that were observed to fracture in a typical brittle failure mode of axial splitting during compressive loading are marked in Fig. 2.5. Fracture was observed during high strain-rate experiments with $\bar{\epsilon} > 0.25$ and no fracture was observed during low strain-rate experiments.
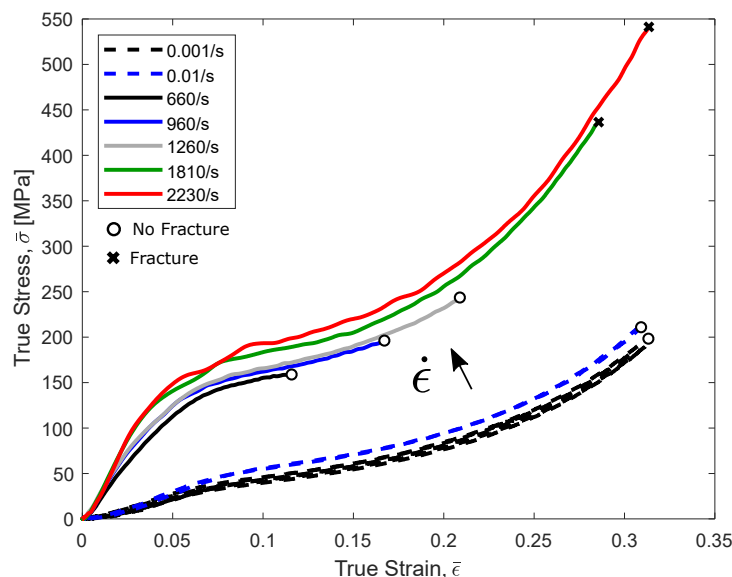
Figure 2.5: Compressive true stress ($\bar{\sigma}$) – true strain ($\bar{\epsilon}$) response of the bulk photopolymer at various strain-rates.

2.3.2 Low Strain-Rate Experiments on Lattice Specimens

Low strain-rate experiments were performed on rod and plate specimen with relative densities of 15%, 20%, 25%, and 30% at a nominal strain-rate of $\dot{\epsilon} \approx 0.001s^{-1}$. Each geometry was tested with at least two specimens. The nominal stress, σ_N, of the specimen was computed using force measurements from the load cell divided by the full area of the lattice and the nominal strain, ϵ_N, was computed using crosshead displacements obtained using DIC divided by the length of the specimen. The use of DIC-measured displacements allowed for correction of undesired crosshead motion.

Figure 2.6(a) shows the low strain-rate nominal stress-strain response ($\sigma_N - \epsilon_N$) of lattice specimens. Good repeatability of the results is demonstrated by the modest differences across stress-strain response for each specimen geometry. All lattice specimens demonstrated a general mechanical response with five distinct regions: I) an initial linear response at low strains around 0.05; II) a monotonically increasing non-linear response until a peak stress is reached; III) a large drop in stress following the peak stress; IV) a long approximately constant plateau 'collapse stress'; and V) followed by steep stiffening. These regions represent the I) nominally elastic response, II) yielding and strain-hardening of the specimen until failure, III) specimen collapse into a localized band, IV) crushing of the localized band, and V) densification. Approximate regions for R30 specimen are shown in Fig. 2.6(a).
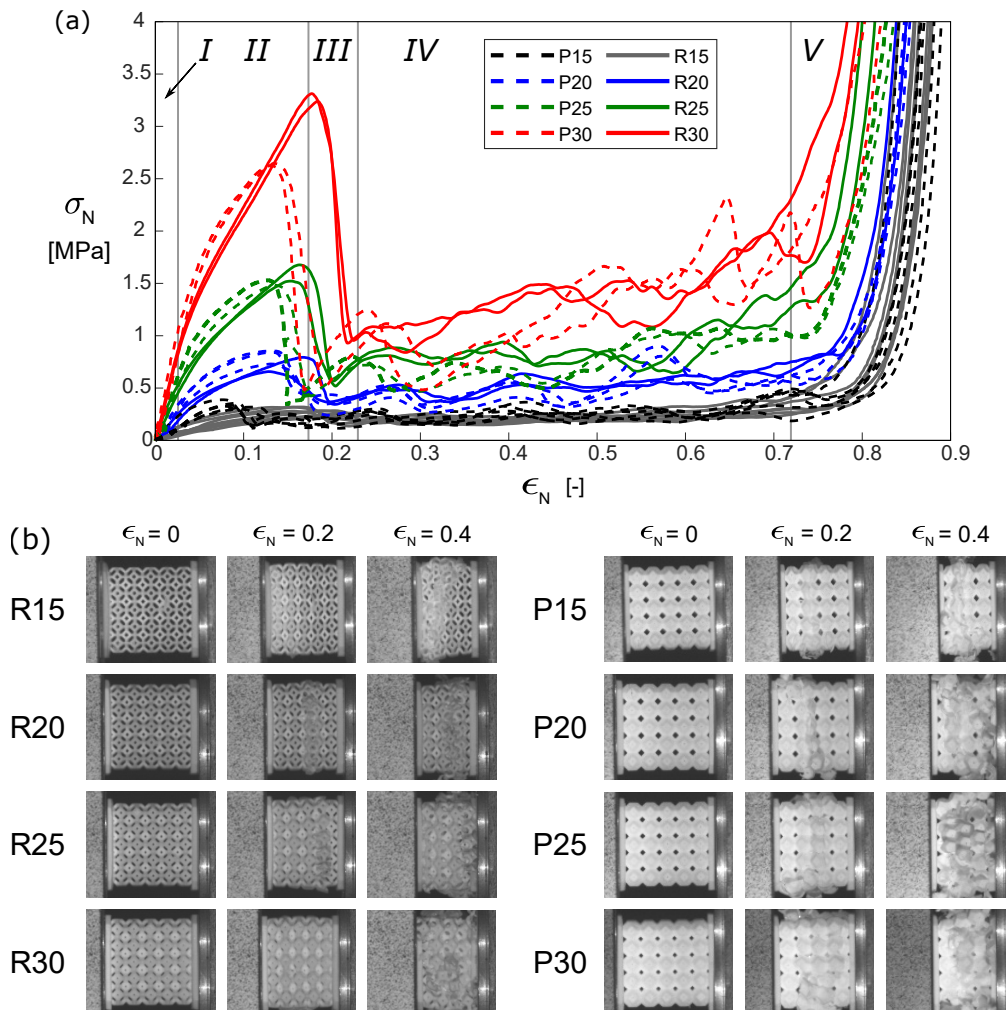
Figure 2.6: Low strain-rate (0.001 s^{-1}) (a) nominal stress (σ_N) – nominal strain (ϵ_N) response of lattice specimens with approximate regions of the mechanical response (I, II, III, IV, and V) for R30 shown; and (b) deformation images for rod (R) and plate (P) specimens with $\rho^*/\rho_s = 15\%, 20\%, 25\%, 30\%$ at $\epsilon_N = 0, 0.2$, and 0.4.

The local stress fluctuations of the crushing region represent the microstructural response and individual failure of each layer normal to the loading. It is observed that densification strain decreases with relative density and stiffening occurs sooner; this is expected due to the increase in material volume of the higher density specimens.

Experimental images as seen in Fig. 2.6(b) show that the specimens initially deformed uniformly, and slight misalignments of baseplates were corrected during low strains less than 0.1. See Supplementary Video S1 for visualization of the full deformation. As loading continued, individual strut failures started to occur and initiation was largely sensitive to and would localize at any geometric defects present from manufacturing. As the lattice localized at initial failures, the loss of strength developed over the formation of a deformation band. The lattice then progressively crushed from the localized band until densification, which led to the sharp steepening of the stress-strain curve (Fig. 2.6(a)). Lower relative density (15%, 20%) specimens were observed to have sharper localizations and narrower collapse bands than higher relative density (25%, 30%) specimens. Mostly transverse (normal) deformation bands were present at lower relative densities and a combination of normal and shear deformation was observed at higher relative densities.

2.3.3 High Strain-Rate Experiments on Lattice Specimens

High strain-rate experiments using a polycarbonate SHPB system were carried out on rod and plate specimens with relative densities of 15%, 20%, 25%, and 30% at an average nominal strain-rate of $\dot{\epsilon} \approx 1000 s^{-1}$. At least two specimens were tested for each geometry to ensure repeatability and consistency of material behavior. The nominal stress, σ_N, of each specimen was computed using the transmitted SHPB force obtained following dispersion correction (Section 2.2.3, Eq. (2.2)) divided by the full area of the lattice. The nominal strain, ϵ_N, was computed using net displacements of the SHPB interfaces measured using DIC divided by the initial axial length of the specimen, L_s. The instantaneous strain-rate experienced by specimens was calculated as the net difference in velocity of the SHPB interfaces measured using DIC divided by the length of the specimen: $\dot{\epsilon}_N(t) = (v_L(t) - v_R(t))/L_s$. During a given experiment, the instantaneous strain-rate reached a mostly uniform value for $\epsilon_N > 0.15 - 0.20$. The average nominal strain-rate was then calculated as the average value of measurements during initial loading (for $\epsilon_N > 0.01$) until unloading of the stress wave. This value varied from $930 \ s^{-1}$ to $1180 \ s^{-1}$ for all specimens.

Figure 2.7(a) shows the compressive high strain-rate nominal stress-strain response ($\sigma_N - \epsilon_N$). Again, we observe repeatability across specimen geometries. Similar to low strain-rate experiments, specimens demonstrated a four-region response with a I) initial linear region, II) yielding and strain-hardening, III) strut fracture and failure, and IV) localization collapse. Densification was not fully observed due to the finite loading pulse of the SHPB. Approximate regions for R30 specimen are shown in Fig. 2.7(a).
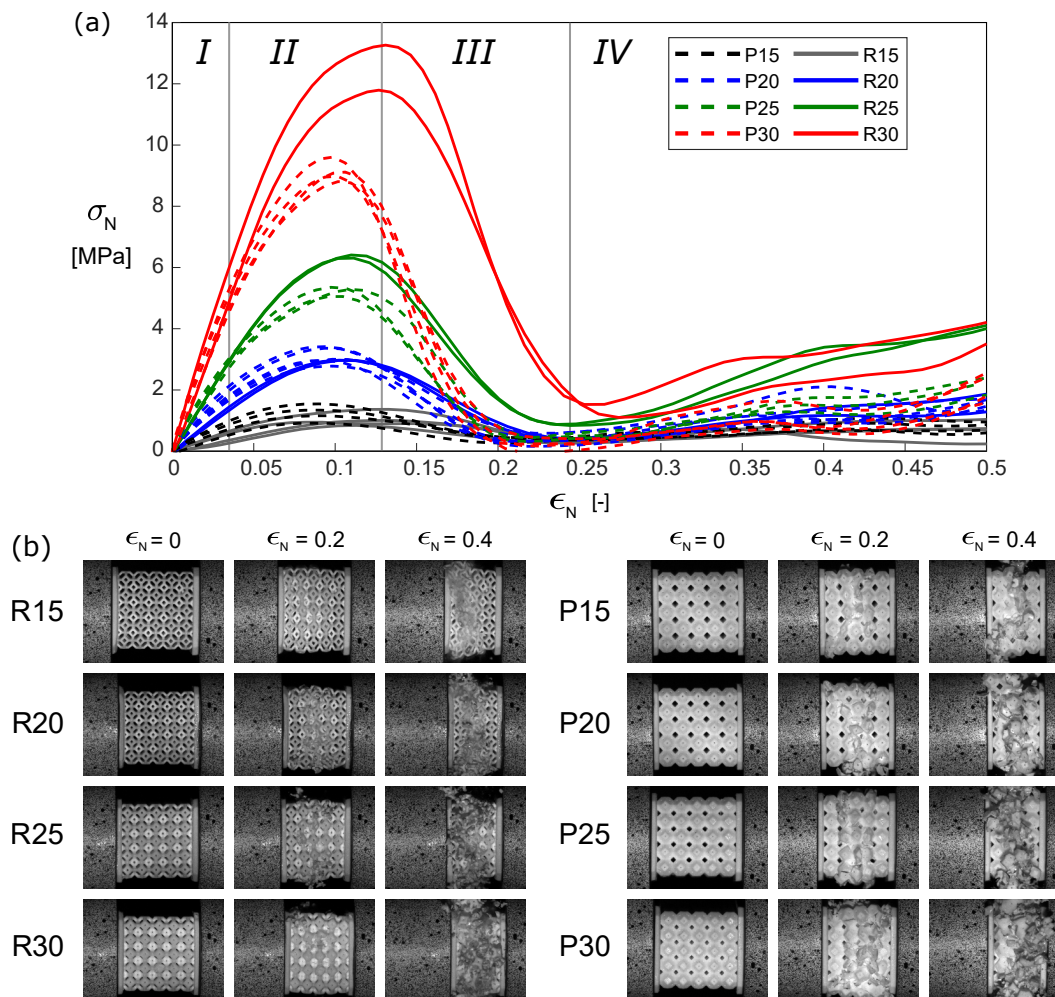
Figure 2.7: High strain-rate (1000 s^{-1}) (a) nominal stress (σ_N) – nominal strain (ϵ_N) response of lattice specimens with approximate regions of the mechanical response (I, II, III, and IV) for R30 shown; and (b) deformation images for rod (R) and plate (P) specimens with $\rho^*/\rho_s = 15\%, 20\%, 25\%, 30\%$ at $\epsilon_N = 0, 0.2$, and 0.4.

In contrast to the low strain-rate response, the drop in stress experienced as the localization band forms is less steep. The lack of local stress peaks shows a progressive crushing (rather than individual layer failure) for the duration of loading. High strain-rate experiments produced high velocity debris which appeared to increase in

volume with relative density. The high velocity debris produced an interesting result in the P30 specimen which experienced no stress in the strain range of 0.2-0.25 due to complete ejection of the material.

Figure 2.7(b) shows the high strain-rate experimental images at $\epsilon_N = 0$, 0.2, and 0.4 for all specimens. Images show large localizations followed by progressive crushing at these strains. See Supplementary Video S2 for visualization of the full deformation. Deformation bands for R15 and P15 specimen appeared nearly planar and normal to the loading direction. An interesting observation is the progressive 'folding' of the P15 specimen unit cells onto each other during crushing compared to the strut fracture of the R15 specimen. Some non-axial shearing failure was observed in higher density specimens, leading to an 'X'-shaped deformation band in the P30 specimen.

2.3.4 Mechanical Properties and Energy Absorption

The mechanical properties of lattice specimens were evaluated from the stress-strain response. The following mechanical properties were identified: (1) failure stress, σ_f, (2) failure strain, ϵ_f, (3) stiffness, S, and (4) specific energy absorption, E_{abs}. σ_f is defined as the maximum value of stress the specimen sustains and ϵ_f the corresponding strain. Stiffness, S, is defined as the secant modulus (σ_N/ϵ_N) of the stress-strain curve at $\epsilon_N = 0.03$. The specific energy absorption is defined as: $E_{abs} = \frac{1}{\rho^*} \int_0^{0.5} \sigma_N d(\epsilon_N)$, where ρ^* represents the mass density of the lattice specimen. We note that all specimens demonstrate dynamic equilibrium (as seen in the force-time histories in Fig. 2.3(b)) by the time the specimen experiences failure. However, by this definition, force equilibrium is not attained at the time the stiffness S is calculated. We assume because the transmitted strain is used in the analysis this can serve as a comparative measure across experiments. We can further assume this is an appropriate approximation based upon the initial linear shape of the curves up to $\epsilon_N = 0.03$.

Cellular materials and lattice structures are widely characterized by scaling laws with relative density [1, 4]. Figure 2.8 shows the mechanical failure properties plotted against relative density on a log-log scale. For some property, $X \propto (\rho^*/\rho_s)^k$ where the scaling exponent, k, can be extracted from the slopes of the lines in Fig. 2.8 and the results for the defined mechanical failure properties are shown in Table 2.2.

Figure 2.8 shows the mechanical properties are clearly affected by strain-rate. σ_f, S, and E_{abs} increase and ϵ_f decreases during high strain-rate loading for all specimens. These trends draw parallels to the mechanical behavior of the polymeric materials, which exhibit stiffening, strengthening, and decreased fracture strains under dynamic loading [81].
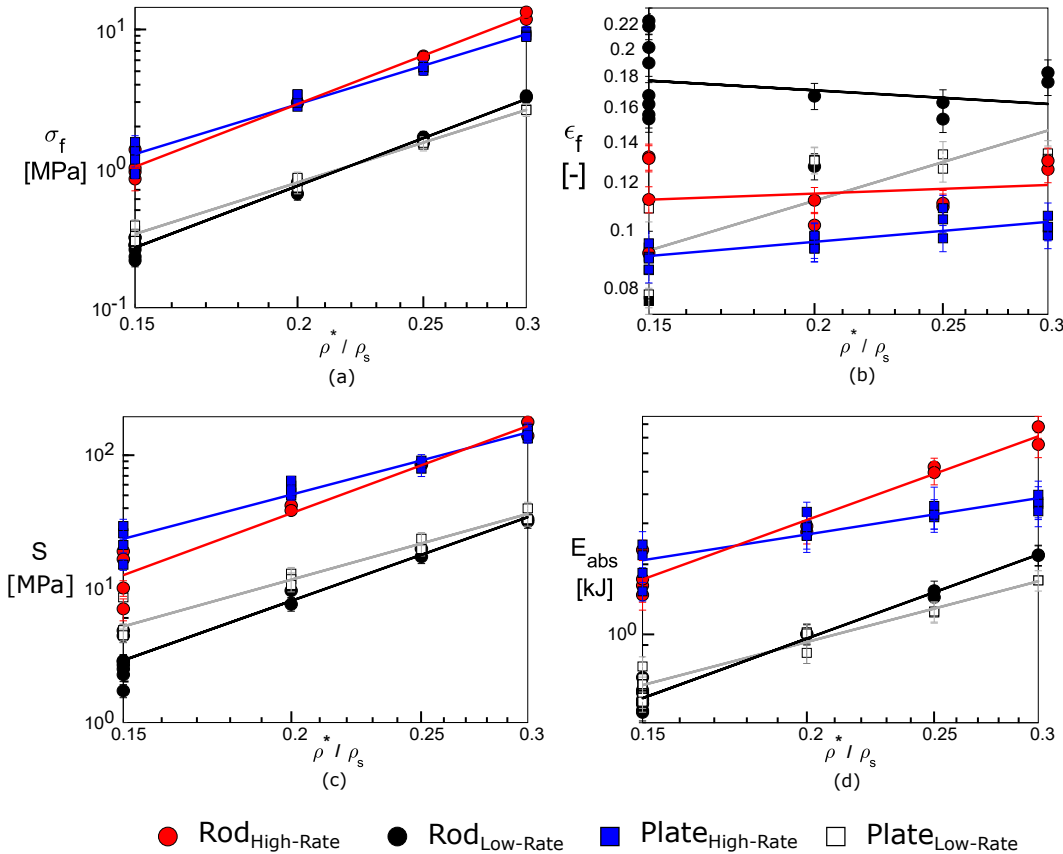
Figure 2.8: Mechanical properties of (a) failure stress σ_f, (b) failure strain ϵ_f, (c) stiffness S, and (d) specific energy absorption E_{abs}, at high and low strain-rates for all lattice specimens as a function of relative density (ρ^*/ρ_s).

Scaling exponents shown in Table 2.2 show a strong correlation between mechanical properties and the relative density of lattice specimens. A higher value of the exponent represents a larger effect of relative density. At both low and high strain-rates, σ_f, S, and E_{abs} show strong positive scaling (dependence) with relative density while ϵ_f appears to be independent of relative density. Rod specimens also exhibited higher values of σ_f, S, and E_{abs} at higher relative densities while plate specimens exhibited higher values at lower relative densities. The transition density at which rod or plate specimens outperform the other is represented by the intersection of the scaling fit-lines and varies from about 0.17 to 0.28 depending on the property. The trends in properties show plate specimens perform well at low

relative densities, but are less effective than rod specimens for energy absorption at higher relative densities. High strain-rate plate specimens show a slightly lower scaling for E_{abs} than low strain-rate plate specimen (0.89 vs 1.48) which may be explained by poor mechanical performance due to complete ejection of the material for $\epsilon_N = 0.2 - 0.25$. Stress concentrations on plate unit cells may also be more prone to failure by fracture. Failure strain ϵ_f was observed to be lower in plate specimens than rod specimens at both loading rates and all relative densities.

Table 2.2: Scaling exponents (k) of experimental mechanical failure properties with relative density (ρ^*/ρ_s) of the lattice specimens: $(\rho^*/\rho_s)^k$.

$Geometry^{Rate}$	σ_f	ϵ_f	S	E_{abs}
Rod^{High}	3.30	0.08	3.70	2.04
Rod^{Low}	3.54	0.13	3.55	2.05
$Plate^{High}$	2.86	0.19	2.64	0.89
$Plate^{Low}$	2.96	0.66	2.79	1.48

Scaling laws have been largely developed through cellular models derived by Gibson and Ashby [1] and have been applied to metallic foams [3]. Bending-dominated open-cell foams scale with relative density, (ρ^*/ρ_s) with stiffness, $S_{open} \propto (\rho^*/\rho_s)^2$ and compressive strength, $\sigma_{c,open} \propto (\rho^*/\rho_s)^{3/2}$. Closed-cell foams scale with relative density with $S_{closed} \propto (\rho^*/\rho_s)^2 + (\rho^*/\rho_s)$ and $\sigma_{c,closed} \propto (\rho^*/\rho_s)^{2/3} + (\rho^*/\rho_s)$. Adaptation of these scalings laws to brittle foams produce mostly similar results but with $\sigma_{c,closed} \propto (\rho^*/\rho_s)^{3/2} + (\rho^*/\rho_s)$. Experiments on open- and closed-cell foams show a range of scaling exponents from $k = 1 - 3$ for stiffness, and $k = 1 - 2$ for compressive strength. The results from the present investigation demonstrate higher scaling values for stiffness and compressive strength in the lattice specimens than metallic foams. These values indicate the lattice specimens have a higher dependence on relative density than metallic foams and are not well-modelled within this density regime using classical approaches.

Dynamic Rate Effects

Strain-rate effects on the mechanical properties can be quantified using a dynamic enhancement factor, D. The factor D for each property is defined as the ratio of the average high strain-rate value to the corresponding average low strain-rate value. These ratios are plotted in Fig. 2.9 for each relative density and specimen type. Error in the factor D was found using error propagation from measurement uncertainty

(determined from the percent difference in bar-interface velocities as shown in Fig. 2.3).
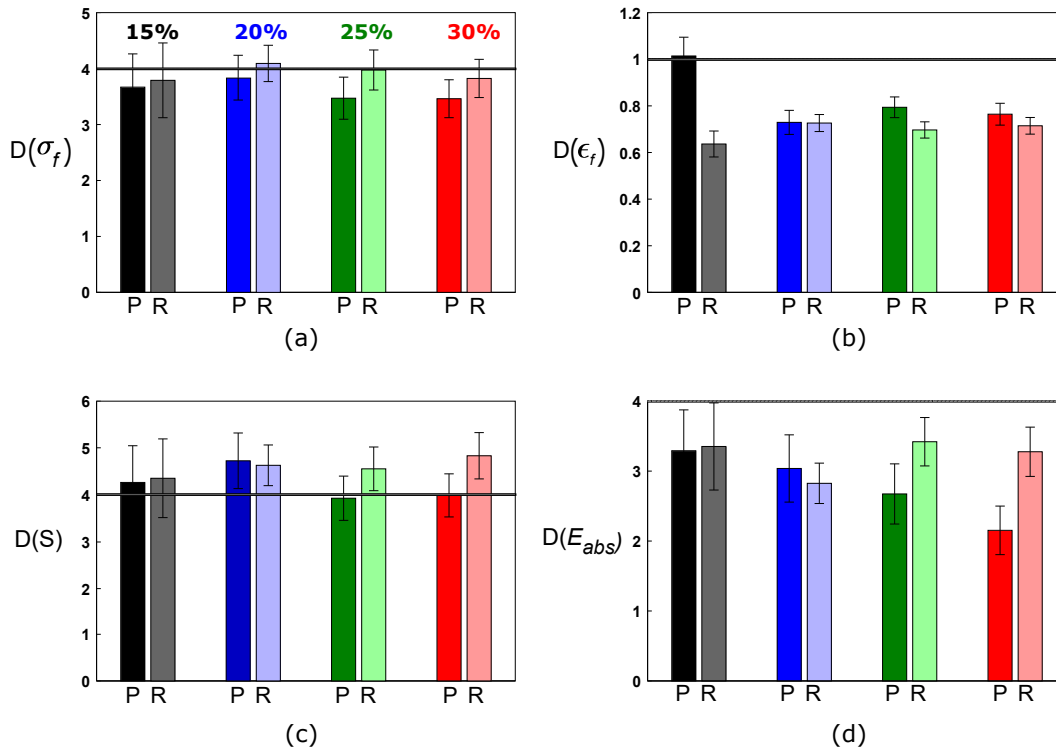
Figure 2.9: Enhancement factor, D for (a) failure stress σ_f, (b) failure strain ϵ_f, (c) stiffness S, and (d) specific energy absorption E_{abs}, for rod (R) and plate (P) geometries of $\rho^*/\rho_s = 15\%, 20\%, 25\%, 30\%$. A D of 4 (σ_f, S, E_{abs}) and 1 (ϵ_f) is marked to estimate the D extracted from base material characterization.

For all specimens, $D(\sigma_f) \approx 3.5 - 4$. A higher $D(\sigma_f)$ was generally observed in rod specimens, but cannot be confirmed due to large uncertainty. For ϵ_f, $D(\epsilon_f)$ is approximately 1 for the P15 specimen, but ≈ 0.8 for all others. A value below 1 represents a lower fracture strain during dynamic loading. ϵ_f appears to be the same across strain-rates for the P15 specimen while it decreases at high strain-rates for all other specimens. $D(S)$ of the stiffness, S, follows similar trends to σ_f and $D(S) \approx 4 - 4.5$ for all specimens. $D(E_{abs})$ for the specific energy absorption was observed to generally be lower for plate specimens than rod specimens and appeared to decrease with ρ^*/ρ_s for plate specimens. This decrease may be associated with poor mechanical performance due to the ejection of material previously discussed. The values of $D(\sigma_f) \approx 3.5 - 4$ correspond well with the D values for strength in the bulk polymer material of $D \approx 6$ at $\epsilon = 0.05$ and $D \approx 3.5$ at $\epsilon = 0.1$ (Fig. 2.5 in Section 2.3.1).

The Kelvin unit cell is known to display bending-dominated behavior [4] and can be expected to have some dependence on both tensile and compressive properties of the base material. The value for D of the photopolymer is measured in compression, but may serve as a baseline approximation for the high strain-rate effect. A value of $D \approx 4$ is estimated from base material characterization and is marked in Fig. 2.9. Slight deviations in loading rates, geometric defects, and tensile weakening effects may explain the deviation of lattice specimen D values from that of the photopolymer. Overall, the differences in lattice specimen D values are small from $D = 4$ and suggest that the dynamic strengthening of the lattice specimen is mostly due to the rate hardening of the base polymer material.

2.3.5 Numerical Simulations

High strain-rate finite element simulations were performed on all lattice geometries using Abaqus/Explicit (Dassault Systems). The velocity of the top rigid plate was set to correspond to nominal strain-rate of $\dot{\epsilon} = 1000/s$. The nominal stress-strain response of the specimen was computed using the nodal forces and displacements of the rigid end plates. Nominal stress, σ_N, was calculated using the rigid-plate force over the full area of the lattice and averaged across the two plates to account for dynamic equilibrium. Nominal strain, ϵ_N, was calculated using the rigid-plate displacement and the axial length of each specimen. The "Brittle Cracking" material model used includes element removal and thus introduces an inherent mesh sensitivity. A mesh sensitivity study was carried out and required a mesh size of 0.20 mm to attain physically relevant and converging simulations. The explicit nature of the simulation also required consideration of dynamic equilibrium of the specimen. The initial bumps in the stress-strain response at $\epsilon_N < 0.02$ reflect that force equilibrium is not attained. Beyond strain $\epsilon_N > 0.02$, stress equilibrium is reached indicated by stress balance of the end plates, $\sigma_{top} \approx \sigma_{bot}$. A constant strain-rate stiffening in modulus is assumed through the definition of E (Young's modulus) in the material model. Low strain-rate experiments on bulk photopolymer (Fig. 2.5) allow extraction of the quasi-static modulus $E \approx 400$ MPa. Thus, assigning $E = 1000$ MPa in numerical simulations introduces an approximate stiffening effect which was defined to qualitatively match experimental stress-strain response and deformation behavior. This effect agrees with experimentally observed strain-rate effects of the photopolymer material (Section 2.3.1).

Figure 2.10(a) shows the nominal stress-strain response ($\sigma_N - \epsilon_N$) for rod-lattice specimens and Fig. 2.10(c) shows the response for plate-lattice specimens. Despite

the simplistic model, the simulation results capture the general mechanical behavior and formation of the deformation band for each specimen. Numerical stress-strain curves exhibit the same four-region mechanical response observed in all experiments (I: elastic response, II: yielding and strain-hardening, III: strut fracture and failure, and IV: localization collapse). This suggests the mechanical behavior of these lattice specimen is largely dominated by brittle failure and that a brittle failure model is an effective model for the base photopolymer material.
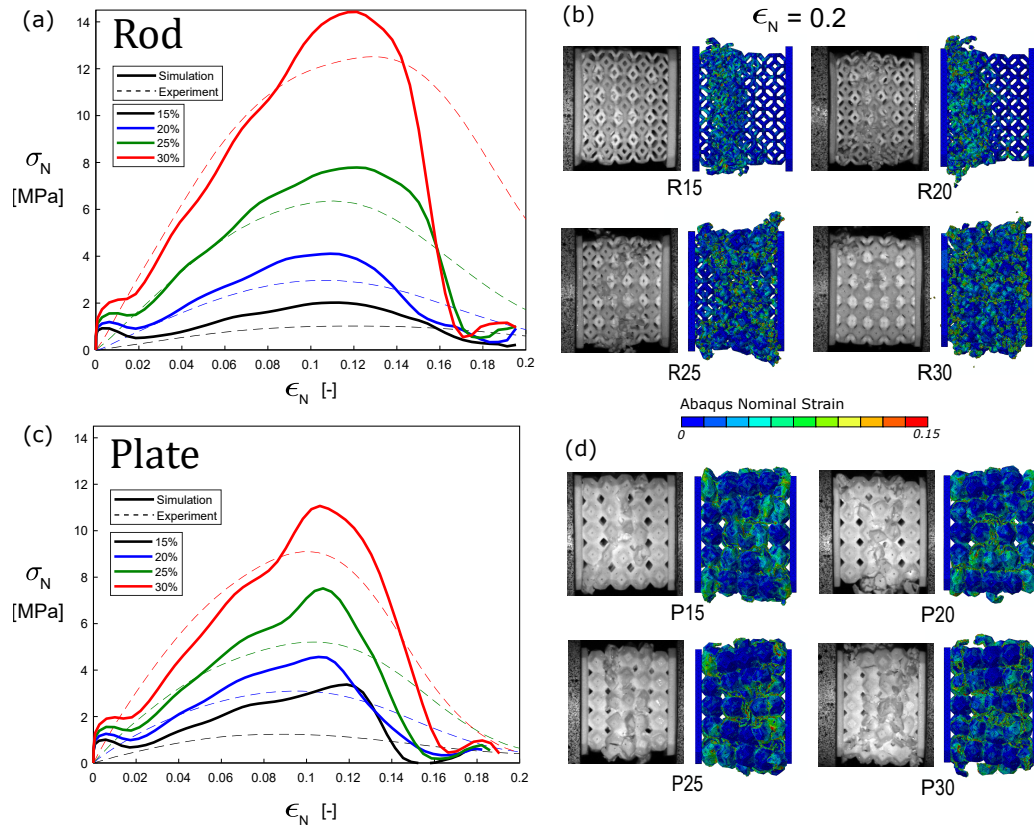
Figure 2.10: Numerical simulation (a) nominal stress (σ_N) – nominal strain (ϵ_N) response of rod specimens compared to average experimental values; (b) deformation images showing Abaqus-computed nominal strains at $\epsilon_N = 0.20$ for R15, R20, R25, and R30 compared to experimental images; and similar plots for plate specimens: (c) $\sigma_N - \epsilon_N$ response; and (d) deformation images for P15, P20, P25, and P30.

Figures 2.10(b) and 2.10(d) compare the experimental and simulation deformation images for rod and plate specimens, respectively, at $\epsilon_N = 0.20$. Good qualitative agreement and trend is found between experimental and simulation deformation modes. Lower density (15%, 20%) specimens showed a more localized deformation band while higher density (25%, 30%) specimens show more uniform deformation. A "X-shaped" deformation pattern can be observed in simulation of plate specimens which was also present in the high strain-rate experiments on P25 and P30 specimens.

This deformation mode shape has also been observed in literature in plate-Kelvin cell lattice structures [49] and the in-plane response of hexagonal honeycombs [82]. Simulation deformation images also reveal higher stress concentrations at unit cell boundaries in plate specimens than in rod specimens. This supports the role of stress concentrations in the weakening of plate specimen due to failure by tensile fracture.

The numerical stress-strain response also provides good validation of the mechanical failure property trends. Figure 2.11 shows the mechanical properties plotted against relative density on a log-log scale for high strain-rate experiments and simulations. Experimentally observed trends of mechanical performance are also observed in the numerical results: rod specimens exhibit higher values of σ_f, S, and E_{abs} at higher relative densities, while plate specimens exhibit higher values at lower relative densities.
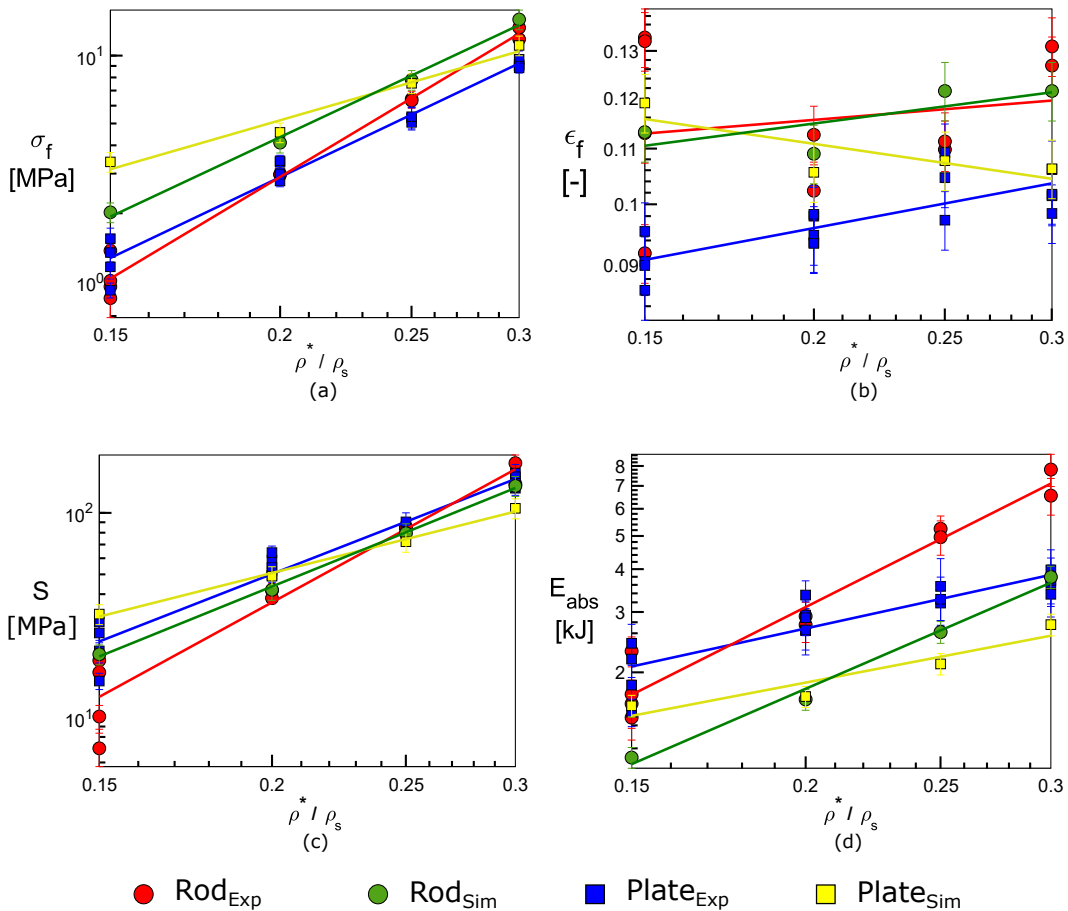
Figure 2.11: Comparison of scaling of mechanical properties with relative density (ρ^*/ρ_s) for high strain-rate experiments and simulations for (a) failure stress σ_f, (b) failure strain ϵ_f, (c) stiffness S, and (d) specific energy absorption E_{abs}.

Table 2.3 shows the scaling exponent values k for both high strain-rate experiment and simulation. In both experiment and simulation, rod specimens exhibit higher scaling exponent values for σ_f, S, and E_{abs} and no clear trend is observed for ϵ_f. Differences in values may stem from experimental geometric defects, differences in measurement resolution, or simplistic material modeling. Simulation results show ϵ_f decreases slightly in plate specimen and increases slightly in rod specimen on the order of 1%. This can be assumed to be outside of the experimental resolution and thus consistent with the weak experimental scaling of ϵ_f with ρ^*/ρ_s. The match between qualitative scaling in both experiment and simulation trends emphasizes there is a transition in mechanical performance of the lattice specimen for the defined mechanical properties.

Table 2.3: Scaling exponents (k) of high strain-rate experimental and simulation mechanical failure properties with relative density (ρ^*/ρ_s) of the lattice specimens: $(\rho^*/\rho_s)^k$.

$Geometry$	σ_f	ϵ_f	S	E_{abs}
Rod^{Exp}	3.30	0.08	3.70	2.04
Rod^{Sim}	2.82	0.13	2.74	1.75
$Plate^{Exp}$	2.86	0.19	2.64	0.89
$Plate^{Sim}$	1.74	0.15	1.71	0.78

2.4   Summary and Conclusions

The high strain-rate compressive behavior of rod and plate polymeric Kelvin lattice structures was experimentally and numerically explored. Mechanical properties such as failure strength, stiffness, and specific energy absorption of lattice specimens show dependence on strain-rate and relative density. Strain-rate experiments on lattice specimen and the base photopolymer material suggest the observed dynamic effects of strain-rate hardening, strain-rate stiffening, and decreased fracture strain may be mostly attributed to the parent polymeric material. A brittle failure material model with strain-rate dependent stiffness (Young's modulus) is shown to be sufficient to simulate lattice structure high strain-rate mechanical response. At both low and high strain-rates, experimental and simulation results show there exists a transition relative density under which plate-lattices outperform rod-lattices of similar mass (relative density) for each mechanical property. Experimental and simulation deformation images suggest no change in dynamic collapse mechanisms, but reveal the formation of a localized failure band more prominent in low strain-rate experiments and low relative density specimens.

The mechanical effects of applying rod or plate geometries to unit cells must be analyzed per geometry, loading rate, and relative density for optimal design. Despite poor performance at higher relative densities, polymeric plate-Kelvin-lattice structures offer improved mechanical properties for lightweight, energy absorbing materials on the millimeter length scale and may be readily manufactured using current technologies for engineering applications.

TRANSIENT DYNAMIC AND SHOCK RESPONSE OF POLYMERIC LATTICE STRUCTURES

Contributions: J.S.W participated in the conception of the project, designed and fabricated specimens, designed and conducted experiments, analyzed the data, and wrote the manuscript.

Abstract

The static and dynamic behavior of polymeric lattice structures is investigated through experiments on octet-truss, Kelvin, and cubic topologies with relative densities around 8%. Dynamic testing is conducted via gas gun direct impact experiments (25 – 70 m/s) with high-speed imaging coupled with digital image correlation and a polycarbonate Hopkinson pressure bar. Mechanical properties such as elastic wave speeds, deformation modes, failure properties, particle velocities, and stress histories are extracted from experimental results. At low impact velocities, a transient dynamic response is observed which is composed of a compaction front initiating at the impact surface and additional deformation bands whose characteristics match low strain-rate behavior. For higher impact velocities, shock analysis is carried out using compaction wave velocity and Eulerian Rankine-Hugoniot jump conditions with parameters determined from full-field measurements.

3.1 Introduction

Lattice structures exhibit behavior consistent with their base materials such as plasticity [83, 84] and heat treatment effects [45] in metals, brittle fracture in ceramics or glassy materials [60, 71, 85, 86], and large deformations in elastomers [87, 88]– these material behaviors also extend to strain-rate effects. Under high strain-rate ($> 1000s^{-1}$) loading, lattices have demonstrated material effects such as strain-rate strengthening in metallic materials [43, 44, 46] and strain-rate stiffening in polymeric materials as seen in Chapter 2. Deformation modes in this regime are similar to those of low strain-rate loading and collapse typically initiates in the middle of the lattice specimen. However, under impact loading (> 250 m/s), a compaction front develops and propagates from the impact surface of the lattice and has been demonstrated experimentally in polymeric [56, 57] and metallic lattices [58]. This

compaction 'wave' has been modeled as a *shock* in cellular materials such as wood [50], honeycombs [53, 89], and foams [51, 54, 62, 63]. This shock response may be modeled using 1D uniaxial planar shock theory and considering the compaction wave front as a density discontinuity in the material. At lower impact velocities, a transient dynamic response has also been demonstrated in honeycombs [53] and foams [54]. Under these loading conditions, deformation does not propagate as discontinuities in density in the form of compaction and instead additional deformation bands form within the cellular material. This behavior may also be expected in lattice structures, but no prior studies have experimentally investigated such response and the transition to the shock regime. Another relatively less explored topic is the effect of topology (geometry of the UC) on this transient dynamic response and the transition to shock-like behavior.

Typical planar shock experiments use laser interferometry to measure particle velocities on a surface of a target material [17, 78] which is used to quantify the bulk shock response in the form of a shock velocity–particle velocity equation of state. Laser interferometry has been successfully applied to shock experiments on periodic cellular materials [90], but does not capture details of the material deformation which may exist at the UC length scale. Full-field measurements are therefore necessary to characterize the response of lattice structures and cellular materials due to inhomogenous deformation. Techniques such as x-ray phase contrast imaging [91] have been used to study lattice structure shock behavior [56–58] and while these techniques are effective in understanding the volumetric response, they require powerful x-rays at advanced facilities such as synchrotrons, are limited in measurement quantity (frames/images), and specimens exist typically at smaller length scales ($O(mm)$). Digital image correlation (DIC) [92] has emerged as a powerful technique in experimental mechanics which allows for full-field displacement measurements and has been readily applied to foams [54, 93] and lattice structures [44, 94]. While DIC is limited to surface measurements, it offers high measurement quantity (number of images) based upon state-of-the-art camera capabilities and requires simpler experimental set-ups; these advantages make DIC an excellent experimental technique to study shock behavior of cellular materials.

In this chapter, the transient dynamic and shock response of polymeric lattice structures and the effect of topology is explored through gas gun direct impact experiments. High-speed imaging and digital image correlation are used to extract full-field measurements of kinematics during impact loading of lattice specimens

and the deformation modes and mechanical responses are analyzed. The low strain-rate, transient dynamic, and shock behavior of cubic (CUB), Kelvin (KEL), and octet-truss (OT) topologies are investigated. These topologies are chosen due to having rod-based architectures with distinct mechanical behaviors: Kelvin lattices demonstrate bending-dominated behavior [4, 95], octet-truss lattices demonstrate stretching-dominated behavior [39], and cubic lattices are chosen as a simple geometry with struts oriented along loading direction.

Section 3.2 describes the experimental methods of this work through specimen design and characterization and description of low strain-rate and direct impact experimental techniques. Section 3.3 then presents the experimental results and discussion of the low strain-rate, compaction, and shock behavior of lattice structures with different topologies. Finally, Section 3.4 presents the summary and conclusions of this work.

3.2 Materials and Methods

3.2.1 Design and Manufacture of Polymeric Lattice Structures

Lattice structure specimens were designed using cubic, Kelvin, and octet-truss unit cells with rod-based struts and a target relative density (volume fraction), ρ^*/ρ_s, of 10% shown in Figs. 3.1(a)-(c).
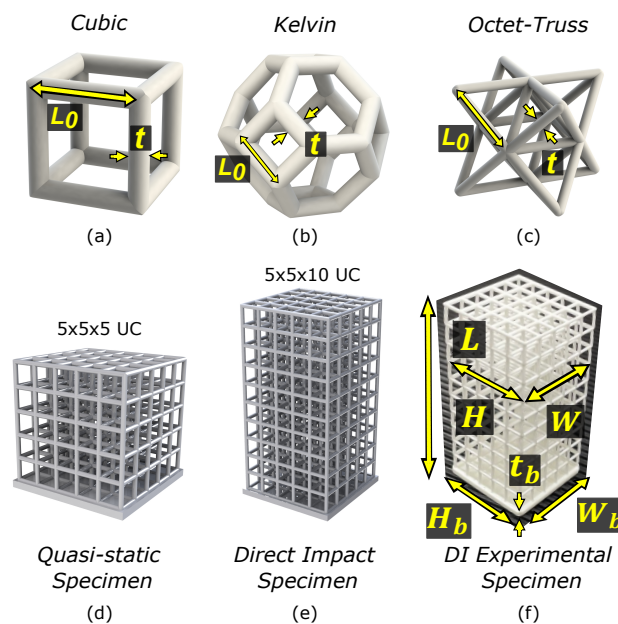
Figure 3.1: Design of lattice specimens: (a) cubic, (b) Kelvin, and (c) octet-truss unit cell geometries with characteristic length, L_0, and strut thickness, t; and cubic topology with (d) CAD 5x5x5 UC geometry, (e) CAD 5x5x10 UC geometry, and (f) experimental 5x5x10 UC specimen with relevant dimensions.

A low relative density was chosen such that topologies showed distinct behavior. At higher relative densities, lattice structure deformation is typically yield-dominated and behavior for various topologies may appear similar. For example, the octet-truss topology transitions from a buckling-dominated response to yield-dominated response around relative densities of 30% [46].

Unit cell geometries were created in SolidWorks (Dassualt Systemes, Providence, RI) with characteristic length, L_0, and strut thickness, t. Two types of specimen were designed for each topology with a 5x5x5 unit cell (UC) geometry used for low strain-rate testing and a 5x5x10 UC geometry used for direct impact testing. L_0 was chosen for each topology to produce a unit cell width of 4.8 mm and the strut thickness was chosen to match a relative density of computed-aided design (CAD) 5x5x10 specimens to 10%.

Values used in specimen design are shown in Table 3.1. Baseplates were also added to improve manufacturability and help ensure planar loading; a 25 mm square baseplate with 1.5 mm thickness was used for octet-truss and Kelvin specimens and a 26 mm square baseplate with 1.5 mm thickness was used for cubic specimens.

Table 3.1: CAD dimensions for characteristic length, L_0, and strut thickness, t, for cubic, Kelvin, and octet-truss unit cell geometries.

Topology	$L_0 [mm]$	t $[mm]$
Cubic	4.80	0.935
Kelvin	1.70	0.625
Octet-Truss	3.40	0.440

Lattice structures were additively manufactured using a vat polymerization technique with Digital Light Processing (DLP) technology. The layer-by-layer projection manufacturing technique of DLP allows for faster printing compared to point-based stereolithography techniques and permits a self-supporting build direction along the length of the specimen. An Autodesk Ember DLP 3D printer (San Rafael, CA) with a 405 nm wavelength light and 2.8 s exposure time per 25 μm layer was used with Colorado Photopolymer Solutions (Boulder, CO) PR57-W photoresin. After printing, specimens were rinsed in an isopropyl alcohol bath and allowed to dry for at least 3 hours before testing.

Relative density was calculated for all experimental specimens using dimensions labeled in Fig. 3.1(f) and volume fraction measurements as follows:

$$\rho^*/\rho_s = \frac{V_{mass} - V_b}{V_f} = \frac{V_{mass} - t_b H_b W_b}{(L - t_b) H W} , \tag{3.1}$$

where V_{mass} is the experimental volume of the full specimen found from mass measurements and assuming a constant material density, V_b is the volume of the rectangular baseplate, and V_f is the space-filling volume of the lattice. The mass density of the photopolymer was determined as 1200 kg/m^3 in Chapter 2 [95]. V_b was calculated from thickness, t_b, width, W_b, and height, H_b, of the baseplate and V_f was calculated using the specimen length, L, width, W, and height, H.

3.2.2 Low Strain-Rate Experiments

Low strain-rate experiments were performed on 5x5x5 lattice specimens using a MTS Model 358.10 servo-hyraulic actuator machine (Eden Prairie, MN) with a 13.3 kN capacity axial load cell. Preliminary experiments on 5x5x10 lattice specimens demonstrated macroscopic out-of-plane bending behavior due to shear localizations and long specimen lengths. This behavior is resultant from the structural geometry, but does not adequately describe the general behavior of a lattice defined by its topology and relative density, and therefore a 5x5x5 UC configuration was chosen for low strain-rate testing.

Relevant experimental dimensions and corresponding relative density for specimens used in low strain-rate experiments are shown in Table 3.2.

Table 3.2: Specimen characterization for low strain-rate experiments.

Experiment #	$m[g]$	$L[mm]$	$W[mm]$	$H[mm]$	$t_b[mm]$	$W_b[mm]$	$H_b[mm]$	$\rho^*/\rho_s[\%]$
CUB_{QS1}	2.723	25.784	24.480	24.518	1.676	25.766	25.788	7.987
CUB_{QS2}	2.702	25.848	24.514	24.530	1.728	25.816	25.828	7.580
CUB_{QS3}	2.573	25.936	24.560	24.568	1.608	25.826	25.840	7.298
KEL_{QS1}	2.656	25.674	24.244	24.220	1.818	24.794	24.844	7.806
KEL_{QS2}	2.758	25.788	24.290	24.230	1.927	24.768	24.826	7.929
KEL_{QS3}	2.399	24.992	24.196	24.234	1.570	24.814	24.754	7.533
OT_{QS1}	2.534	25.414	24.146	24.114	1.768	24.848	24.860	7.406
OT_{QS2}	2.473	25.222	23.962	23.866	1.772	24.824	24.796	7.236
OT_{QS3}	2.349	25.164	23.952	23.878	1.640	24.796	24.836	7.042

Lattice specimens were compressed at a rate of 1.5 mm/min, corresponding to a nominal strain-rate of $\dot{\epsilon} \approx 0.001s^{-1}$, until densification. Experimental images were taken at 24 frames per second using a Fastec IL5 High-Speed Camera (San Diego, CA) with a 100 mm Tokina AT-X Pro lens (Tokyo, Japan) and a Techniquip FOI-150-

UL continuous light source (Pleasanton, CA). A speckle pattern was applied to the hydraulic crosshead and 2D digital image correlation (DIC) using Vic2D (Correlated Solutions, Columbia, SC) was conducted at 1 fps to extract displacements. A subset size of 53 pixels (px) with a step size of 5 px was used for an area of interest of 36 mm × 16 mm (8 px/mm) in the DIC analysis.

3.2.3   Direct Impact Experiments

Direct impact experiments with high-speed imaging were conducted on 5x5x10 lattice specimens at impact velocities from 25 m/s to 70 m/s using a gas gun and polycarbonate (PC) Hopkinson pressure bar (HPB) as shown in Fig. 3.2. A Delrin disk (flyer) with 50.80 mm diameter and 25.40 mm length was used to impact specimens inside a chamber with a transparent PC window. Lattice specimens were taped to a PC anvil (31.75 mm diameter) which in turn was press fit onto a longer PC bar (25.40 mm diameter, 1.83 m length) and surrounded by a C-shaped aluminum stopper and two pieces of rubber. This 'stopper' prevented the flyer from fully densifying the specimen and transmitting high forces that could inelastically deform the pressure bar through high strains.
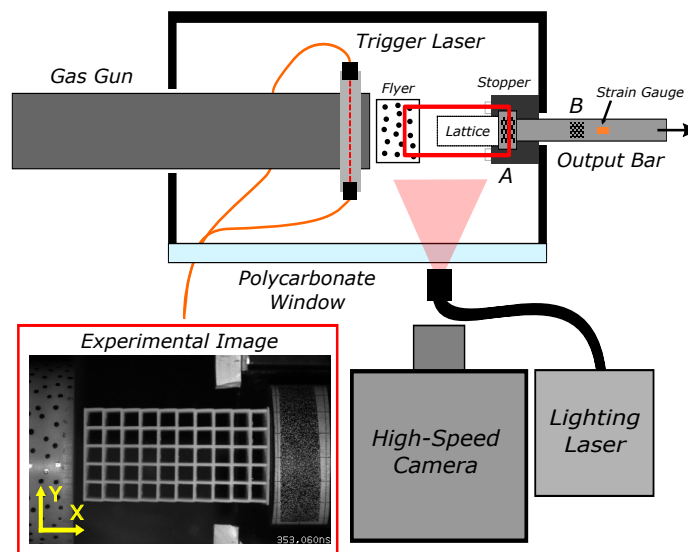
Figure 3.2: Schematic of direct impact experimental set-up with high-speed imaging and PC Hopkinson pressure bar. Insert shows an experimental image of speckled Delrin flyer, cubic lattice specimen and speckled PC anvil prior to impact. *X* and *Y* are the axial (horizontal) and transverse (vertical) coordinates, respectively, in the undeformed configuration.

High-speed images were taken using a Hyper Vision HPV-X2 camera (Shimadzu, Kyoto, Japan) with a 100 mm Tokina AT-X Pro lens and lighting from a non-coherent CAVILUX Smart laser (Cavitar, Tampere, Finland) with 40 ns pulse lengths. 128

images were taken at a constant framing interval (8,500 ns – 22,500 ns) set to maximize number of images taken during deformation depending on target impact velocities of 30 m/s, 50 m/s, and 70 m/s. Image capture and data acquisition was triggered using a Wilcom F6230A visual fault locator (Belmont, NH) directed through the gas gun barrel using fiber optic cables, a Thorlabs PDA10A2 photodiode (Newton, NJ), and a 2.5 GHz Tektronix DPO 3014 digital oscilloscope (Beaverton, OR). A trigger was sent as the flyer interrupted the visual fault locator and a voltage drop from the photodiode was registered for longer than 100 μs.

Specimen characteristics and imaging parameters for all direct impact experiments are shown in Table 3.3.

Table 3.3: Specimen characterization and imaging parameters for direct impact experiments.

Experiment #	$m\,[g]$	$L\,[mm]$	$W\,[mm]$	$H\,[mm]$	$t_b\,[mm]$	$W_b\,[mm]$	$H_b\,[mm]$	$\rho^*/\rho_s\,[\%]$	$\Delta t\,[ns]$	FPS	v_i [m/s]
CUB_{DI1}	4.191	49.594	24.552	24.550	1.703	25.834	25.784	8.171	20,000	50,000	24.21
CUB_{DI2}	4.090	49.608	24.552	24.560	1.598	25.878	25.810	8.089	12,000	83,333	49.34
CUB_{DI3}	3.806	48.810	24.650	24.660	0.840	25.936	25.880	8.942	8500	117,647	61.22
KEL_{DI1}	3.314	48.290	24.300	24.238	0.710	24.832	24.850	8.291	22,500	44,444	24.81
KEL_{DI2}	3.695	49.016	24.424	24.470	0.990	24.804	24.810	8.605	12,000	83,333	45.83
KEL_{DI3}	3.835	48.582	24.304	24.308	0.925	24.844	24.900	9.317	8,500	117,647	67.27
OT_{DI1}	3.776	49.148	24.010	24.016	1.808	24.770	24.762	7.465	22,500	44,444	25.63
OT_{DI2}	3.603	48.802	23.966	23.968	1.798	24.704	24.778	7.048	12,000	83,333	51.29
OT_{DI3}	3.041	47.304	23.728	23.800	1.070	24.798	24.780	7.186	8,500	117,647	73.11

Digital Image Correlation Analysis

Digital image correlation (DIC) was performed on three areas of interest (AOI) in the experimental images. The AOIs and corresponding DIC analyses for an octet-truss lattice impacted at 73.1 m/s (Exp. #OT_{DI3}) are shown in Fig. 3.3.

A Sharpie pen (Fine Point) was used to create a random speckle pattern on the flyer for AOI1, black spray paint and tape were used to make the speckle pattern on the anvil for AOI3, and the lattice geometry itself served as a unique subset for AOI2. A subset size of 23 px (4.6 mm) was used for AOI1 and AOI3 and a subset size of 27 px (5.4 mm) was used for AOI2 (corresponding to ~ 1.2 of a unit cell) with a step size of 1 px used in all analyses. While local strains of the lattice are inherently smoothed during the analysis due to a subset size greater than the unit cell size, these subset sizes remain relevant to approximate the material as a continuum. Incremental correlation was used for all analyses due to large deformations of the lattice and to remain consistent across all three areas of interest. Additionally, a 0.09 px confidence error threshold was used for data removal of highly deformed or overexposed regions. Particle velocities shown in Fig. 3.3 were computed in

Vic2D using a constant timing interval and three-point central difference numerical method. The impact velocity of the flyer, v_i, in each experiment was computed from DIC of the flyer (AOI1) prior to impact and is shown in Table 3.3. Anvil particle velocities were $\mathcal{O}(10)$ mm/s and much smaller than the magnitudes of the flyer and lattice particle velocities.
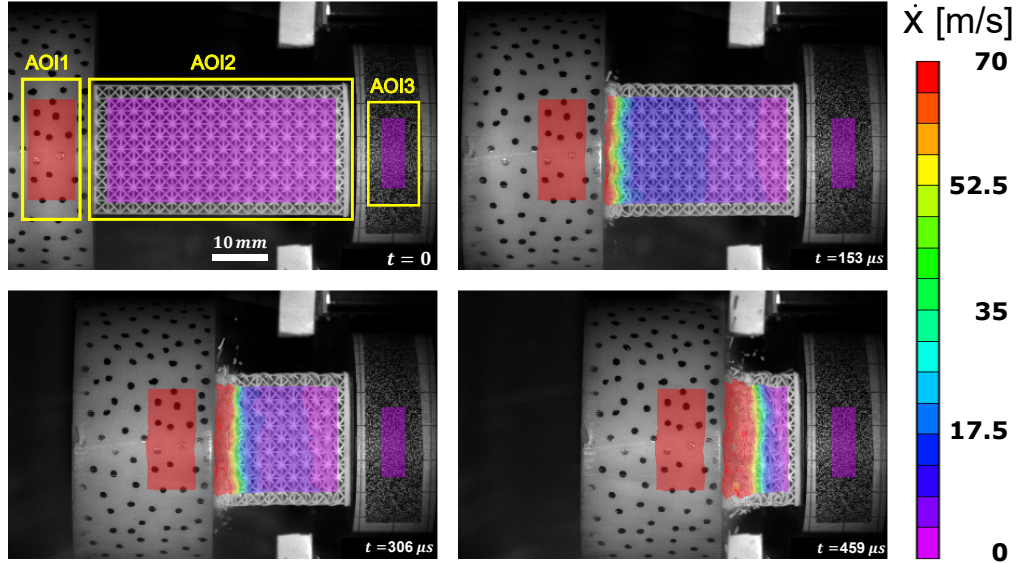
Figure 3.3: Digital image correlation analysis on Delrin flyer (AOI1), octet-truss lattice specimen (AOI2), and PC anvil (AOI3) at times t = 0, 153 μs, 306 μs, and 459 μs after impact for Exp. #OT_{DI3}. Particle velocity ($\dot{x}$) results from all AOI are superimposed on each image.

Hopkinson Pressure Bar Analysis

Strain gauge measurements on the polycarbonate pressure bar allowed extraction of the force acting on the distal (non-impacted) end of the lattice through conventional Hopkinson pressure bar (HPB) analysis. Two Vishay EA-13-031CE-350/LE gauges (1/4 bridge configuration) were placed diametrically opposite 0.6 m from the lattice-anvil interface and a Vishay 2310B signal conditioning amplifier (Raleigh, NC) and Agilent MSO9404A oscilloscope (20 GSa/s sample rate) (Santa Clara, CA) were used to record strain gauge voltage data. A low input voltage of 1.4 V was used to avoid heating effects in the strain gauges.

Following elastic HPB analysis [78], the particle velocity and force at the bar interface may be found using:

$$v(t) = c_0 \epsilon_{SG}(t) , \tag{3.2}$$

$$F(t) = EA \epsilon_{SG}(t) , \tag{3.3}$$

where v is the velocity of the bar interface, E is the Young's modulus of the PC bar taken as 2.37 GPa [96], c_0 is the bulk wave speed in the PC bar taken as 1405 m/s (using $c_0 = \sqrt{E/\rho}$ with density $\rho = 1200 kg/m^3$ [96]), ϵ_{SG} is the strain-gauge measurement in the bar, F is the force experienced at the lattice-anvil interface, and A is the cross-sectional area of the bar.

Viscoelastic analysis following Bacon [79] was also carried out using an additional set of strain gauges placed 0.3 m from the lattice-anvil interface. Elastic analysis matched viscoelastic analysis and typical strain measurements were low ($\mathcal{O}(100)\mu\varepsilon$) which justified the use of elastic analysis in this loading regime and experimental set-up.

A similar trigger was sent to imaging (high-speed camera) and HPB components (strain gauges) and allowed comparison of time-linked measurements. Velocities were extracted from both DIC and HPB analyses and used to validate strain gauge measurements. Figure 3.4(a) shows the computed anvil velocities using DIC and HPB techniques for all three topologies with $v_i \approx 50$ m/s. The corresponding DIC location is marked as position A in Fig. 3.2. Velocities of $\mathcal{O}(0.1 - 0.7)$ m/s corresponded to sub-pixel resolution of the DIC analysis and the resulting DIC confidence intervals were comparable to the magnitudes of HPB measurements. However, an overall qualitative match in the shape and magnitude of the velocity profiles was observed.
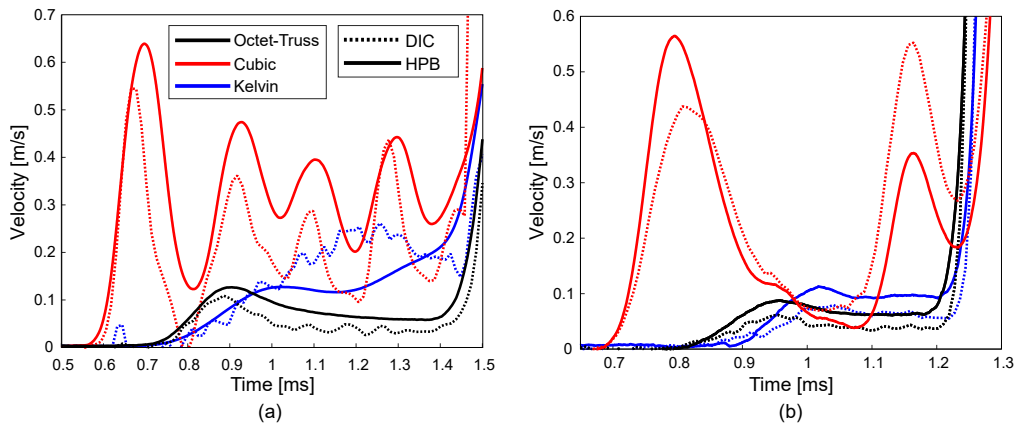
Figure 3.4: Hopkinson pressure bar (HPB) measurements were validated through comparison to DIC-computed velocities of the (a) anvil at impact velocity, $v_i \approx 50$ m/s and (b) pressure bar at impact velocity, $v_i \approx 70$ m/s.

An additional set of validation experiments was carried out at $v_i \approx 70$ m/s with a DIC location next to the strain gauges (corresponding to position B in Fig. 3.2). Velocities are shown in Fig. 3.4(b) and strain measurements showed good match with DIC

measurements with differences comparable to that of anvil experiments. Qualitative matching of velocities from both the anvil and pressure bar gives validation that strain gauge measurements are accurate and differences in measurements may be attributed to analysis techniques rather than effects of the anvil.

3.3 Results and Discussion

3.3.1 Low Strain-Rate Behavior of Lattice Structures

Low strain-rate experiments were performed on 5x5x5 lattice specimens at a nominal strain-rate of $\dot{\epsilon} \approx 0.001 s^{-1}$. Three experiments were conducted for each topology to verify repeatability of results and specimen characteristics for each experiment are shown in Table 3.2. The nominal stress, σ_N, of each specimen was found by dividing load cell force measurements by the full area of the lattice ($H * W$) and the nominal strain, ϵ_N, was found by dividing DIC-computed displacements of the hydraulic crosshead by the length of the lattice ($L - t_b$). Deformation images were taken during experiments and linked in time to mechanical measurements.

Figure 3.5(a) shows the low strain-rate nominal stress-strain response ($\sigma_N - \epsilon_N$) for each specimen. While variation between individual specimens exists, there is good repeatability of the general response of each topology. Specimens demonstrated behavior consistent with that of brittle cellular materials [1] which included an initial linear elastic region before a critical failure stress (σ_f) was reached and subsequent softening occurred. Then, crushing of the lattice progressed at a relatively constant plateau stress before struts began to contact and steep stiffening occurred due to densification of the material.
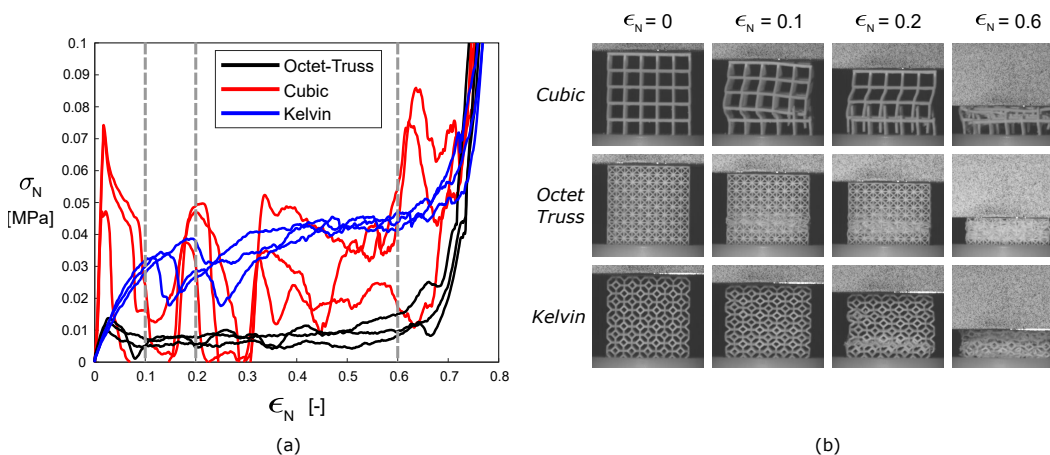
Figure 3.5: Low strain-rate (a) nominal stress (σ_N) – nominal strain (ϵ_N) response and (b) deformation images of specimens at $\epsilon_N = 0, 0.1, 0.2,$ and 0.6 which are represented as vertical lines in (a).

Images shown in Fig. 3.5(b) demonstrate the deformation modes of each lattice topology and show nominal strains of $\epsilon_N = 0, 0.1, 0.2$ and 0.6. The cubic topology showed a catastrophic failure deformation mode initiated by macroscopic buckling at strains $\epsilon_N < 0.1$ and fracture of vertical struts in a given horizontal layer of unit cells for strains $\epsilon_N > 0.1$ which then progressively failed in a layer-by-layer fashion. This behavior is demonstrated in the $\sigma_N - \epsilon_N$ response by sharp rises and drops in stress associated with the loading and failure of each layer. The octet-truss topology showed the weakest $\sigma_N - \epsilon_N$ response and deformation images revealed a buckling-dominated response which initiated after a peak failure stress. The progressive crushing of the lattice continued through buckling and showed a low, constant plateau stress until densification. This deformation mode and softening response is expected due to the "stretching-dominated" behavior of the geometry [39]. Finally, the Kelvin topology showed a strain-hardening response with "bending-dominated" deformation concentrated at the strut nodes. This observation is consistent with Maxwell's stability criterion analysis of this geometry [16] as well as experimental work on Kelvin lattices of the same material in Chapter 2 [95].

Low Strain-Rate Mechanical Properties

Low strain-rate mechanical deformation and failure properties were extracted from the $\sigma_N - \epsilon_N$ response of each specimen. The following properties were calculated: (1) stiffness, S, (2) specific energy absorption, E_{abs}, (3) failure stress, σ_f, and (4) failure strain, ϵ_f. S was defined through the slope of the initial $\sigma_N - \epsilon_N$ response and calculated using a linear fit of select data points ($0.01 < \epsilon_N < 0.05$) with a maximized R-squared value. E_{abs} was defined as: $E_{abs} = \frac{1}{\rho^*} \int_0^{0.6} \sigma_N d(\epsilon_N)$ where ρ^* is the mass density of the specimen and the upper integration bound of $\epsilon_N = 0.6$ was chosen to represent a typical strain before densification effects (stiffening) initiated. σ_f was defined as the maximum stress the specimen sustains before failure (softening) occurs, and ϵ_f was defined as the corresponding strain at failure.

Figure 3.6 shows the low strain-rate mechanical failure properties for all lattice specimens. Relative densities of the specimens were computed using Eq. (3.1) and showed significant distinctness in values. Particularly, the lower relative densities of the octet-truss specimens may be attributed to the smaller manufacturing dimensions of the geometry and limitations of the printer resolution.

Cubic specimens demonstrated the highest stiffness by a factor of ~ 5 compared to the Kelvin and octet-truss topologies. This high stiffness is in agreement with
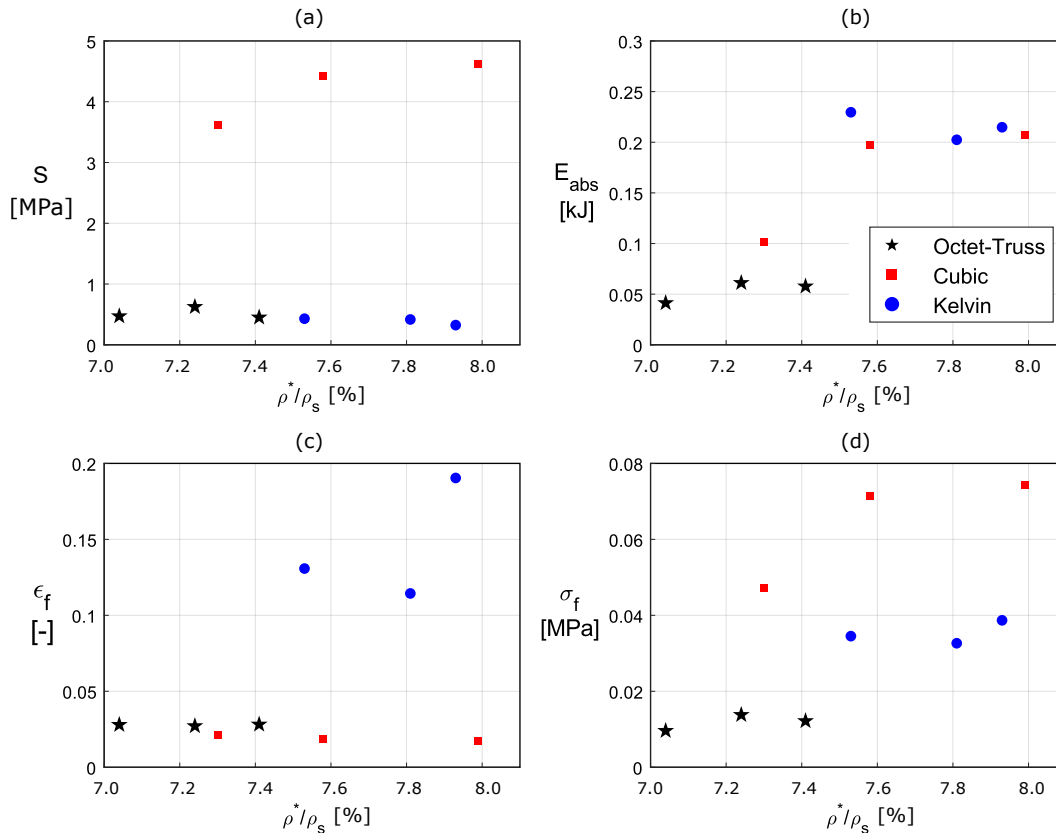
Figure 3.6: Low strain-rate mechanical properties of lattice structures for (a) stiffness, S, (b) specific energy absorption, E_{abs}, (c) failure strain ϵ_f, and (d) failure stress, σ_f.

rigid "stretching-dominated" behavior which was demonstrated through an initial buckling deformation mode. Maxwell's stability criterion (as well as buckling behavior) also describes the octet-truss topology as "stretching-dominated." But, while it is expected for a "stretching-dominated" geometry to have higher stiffness than a "bending-dominated" geometry for a relative density around 10% [16], this is not apparent from experimental results for the octet-truss and Kelvin specimens. However, the stiffness of lattice structures is also dependent on relative density [4], and lower density octet-truss specimens generated slightly higher stiffness values than Kelvin specimens of higher densities. It is reasonable to conclude octet-truss lattices of similar densities would demonstrate higher values than Kelvin lattices.

The octet-truss topology showed the lowest specific energy absorption, which may be related to a buckling deformation response compared to bending (Kelvin) or fracture (cubic). Meanwhile, cubic and Kelvin topologies showed similar E_{abs} values. Considering failure properties: Kelvin specimens showed the highest failure strain while octet-truss and cubic specimens showed lower values; and cubic specimens

demonstrated the greatest failure stress, followed by Kelvin, and octet-truss specimens. The failure stress results draw parallels to that of specific energy absorption and may be considered a large contributing factor to the total energy absorbed during low strain-rate loading. Densification strain was similar for all three lattice topologies with a value of ≈ 0.75 represented by convergence of the stiffening sections of the $\sigma_N - \epsilon_N$ curves in Fig. 3.5(a). Lattice relative densities were distinct but similar in values which agrees with experimental observations in foams that show densification strain is a function of relative density [1].

3.3.2 Elastic Wave Speeds in Dynamic Experiments

Full-field measurements from DIC allow extraction of particle displacements over the entire impacted lattice specimens. An example of particle displacement (δ) as a function of undeformed coordinate (X) profiles for an octet-truss specimen impacted at 73.1 m/s (Exp. #OT_{DI3}) is shown in Fig. 3.7(a). Particle displacements were computed for each undeformed horizontal coordinate (X) pixel and averaged over 20 undeformed vertical coordinate (Y) pixels about the center of the specimen, corresponding to the width across the center unit cell. Displacement – undeformed coordinate ($\delta - X$) profiles are plotted for each time instance in Fig. 3.7(a) where each line depicts data from one experimental image. Increasing time is recognized as rightward translation of each profile and positive concavity illustrates the trend of increasing displacement at all positions across the lattice.
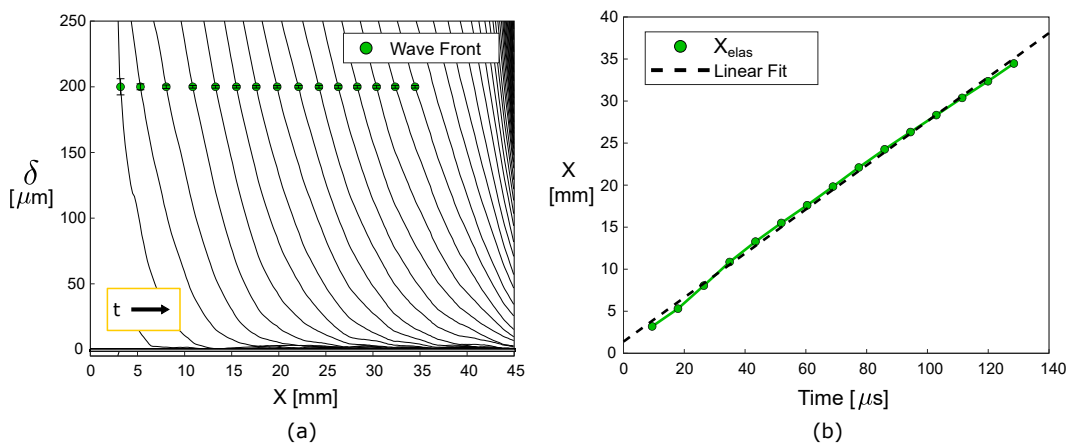
Figure 3.7: Elastic wave extraction: (a) particle displacement (δ) – undeformed coordinate (X) profiles with elastic wave front positions at 200 μm and (b) corresponding elastic wave front-time history for Exp. #OT_{DI3}.

The elastic wave front was defined using a displacement criterion of 200 μm which was chosen to approximate 1 pixel (image resolution: $\sim$ 5 pixels/mm). The DIC

analysis is capable of sub-pixel accuracy and error bars are plotted, which are small ($< \pm 1.5 \mu m$). Elastic wave speeds may then be extracted using displacement measurements since the time instance of each experimental image is known. The elastic wave front may be defined in position and time and is shown in Fig. 3.7(b) for the corresponding data in Fig. 3.7(a). A linear fit was applied to the elastic front position-time history and the slope was taken as the wave speed. The elastic wave speed was calculated using positions $X < 35$ mm to avoid boundary effects from the baseplate.

The elastic wave speeds for all impact experiments are shown in Fig. 3.8. Figure 3.8(a) shows the dependence of elastic wave speed on relative density. Elastic wave speeds appeared mostly constant for each topology with the cubic topology showing the highest speed followed by octet-truss and Kelvin topologies. This relationship closely follows trends of low strain-rate stiffnesses and agrees with the continuum approximation of longitudinal wave speed as $c = \sqrt{E/\rho}$ where E is Young's modulus (stiffness) of lattice specimens and density is similar for all specimens.
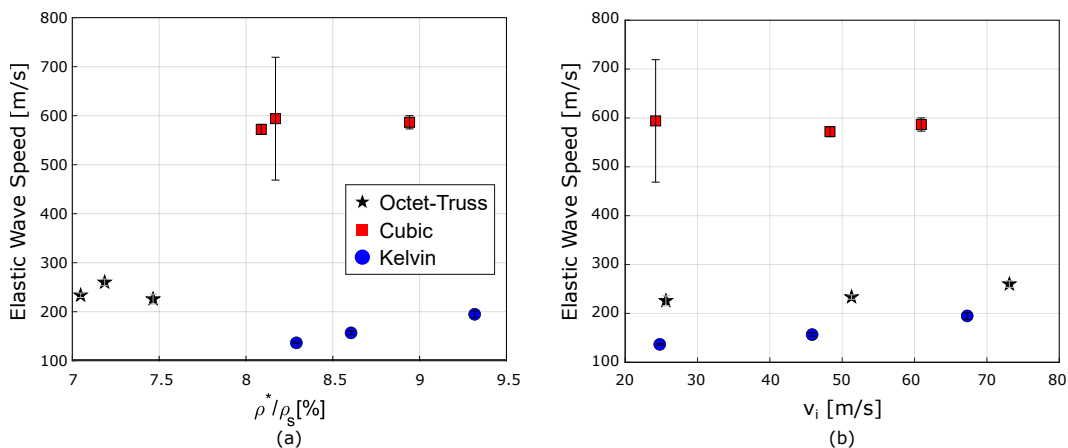
Figure 3.8: Elastic wave speeds vs. (a) relative density, ρ^*/ρ_s, and (b) impact velocity, v_i, for cubic, Kelvin, and octet-truss specimens. Error was defined using a 95% confidence bound and was large when few data points were used for fitting.

Figure 3.8(b) shows dependence of elastic wave speed on impact velocity. A slight increase in elastic wave speed with impact velocity was observed for octet-truss and Kelvin topologies, while no clear trend was discernible for the cubic topology. Large confidence bounds for the cubic specimen impacted at 24 m/s (Exp. #CUB_{DI1}) were a result of applying a fit to few data points (due to a high wave speed and low framing rates). Though, a general increase in wave speed with impact velocity may be realized in the data and interpreted by considering strain-rate stiffening of the base material which was observed for the photopolymer in Chapter 2 [95].

3.3.3 Compaction Behavior of Lattice Specimens

Deformation bands or strain concentrations occurring in different regions of cellular materials may be used to define unique deformation regimes. Transient dynamic behavior has been observed computationally in impact loading of honeycombs of $\rho^*/\rho_s = 10\%$ at $v_i = 10$ m/s [53] and experimentally in aluminum 6061 foams of $\rho^*/\rho_s \approx 8\%$ at $v_i \approx 35$ m/s [54]. This type of behavior demonstrates deformation occurring at distal ends (honeycomb) or mid-sections (foam) in addition to deformation at the impacted surface. In contrast, a more uniform dynamic response was found at strain-rates around 1000 s^{-1} (corresponding to $v_i \approx 15 - 20$ m/s) in Kelvin lattice structures of $\rho^*/\rho_s = 15 - 30\%$ in Chapter 2 of this thesis. These materials demonstrated deformation bands in the middle of the specimen similar to their low strain-rate behavior. During high velocity impact (e.g., $v_i > 250$ m/s) lattice structures exhibit another deformation mechanism–that of a sole progressing compaction (crushing) front initiating at the impact surface [56–58]. There exists a transition point between these deformation regimes dependent on the material, but this transition has not yet been fully explored in lattices. Impact velocities of $25 - 70$ m/s span a range of strain-rates in between the transient dynamic and shock regimes for polymeric lattice structures investigated in this study. The mechanical response of lattice specimens was analyzed in these regimes using DIC based full-field strain and particle velocity measurements and HPB force measurements.

Deformation Modes

Deformation modes of each specimen were analyzed from full-field DIC measurements. As previously described for particle displacements in Section 3.3.2, similarly, data for each X-position pixel was averaged over the central 20 Y-position pixels of the lattice AOI where 20 pixels was approximately the width of one UC.

Figure 3.9 shows deformation mode results for the octet-truss topology. Figure 3.9(a),(b),(c) show the longitudinal Lagrangian strain (ϵ_{XX}) – undeformed coordinate (X) profiles for octet-truss specimens with impact velocities (v_i) of 25.6 m/s, 51.3 m/s, and 73.1 m/s, respectively. Figure 3.9(d),(e),(f) show corresponding strain-fields taken at nominal impact strains ($\varepsilon = \Delta x_{flyer}/(L - t_b)$) of 0, 0.2, 0.4, and 0.6. The $\epsilon_{XX} - X$ profiles of the time instances at these nominal impact strains are represented using bold lines in Fig. 3.9(a),(b),(c).
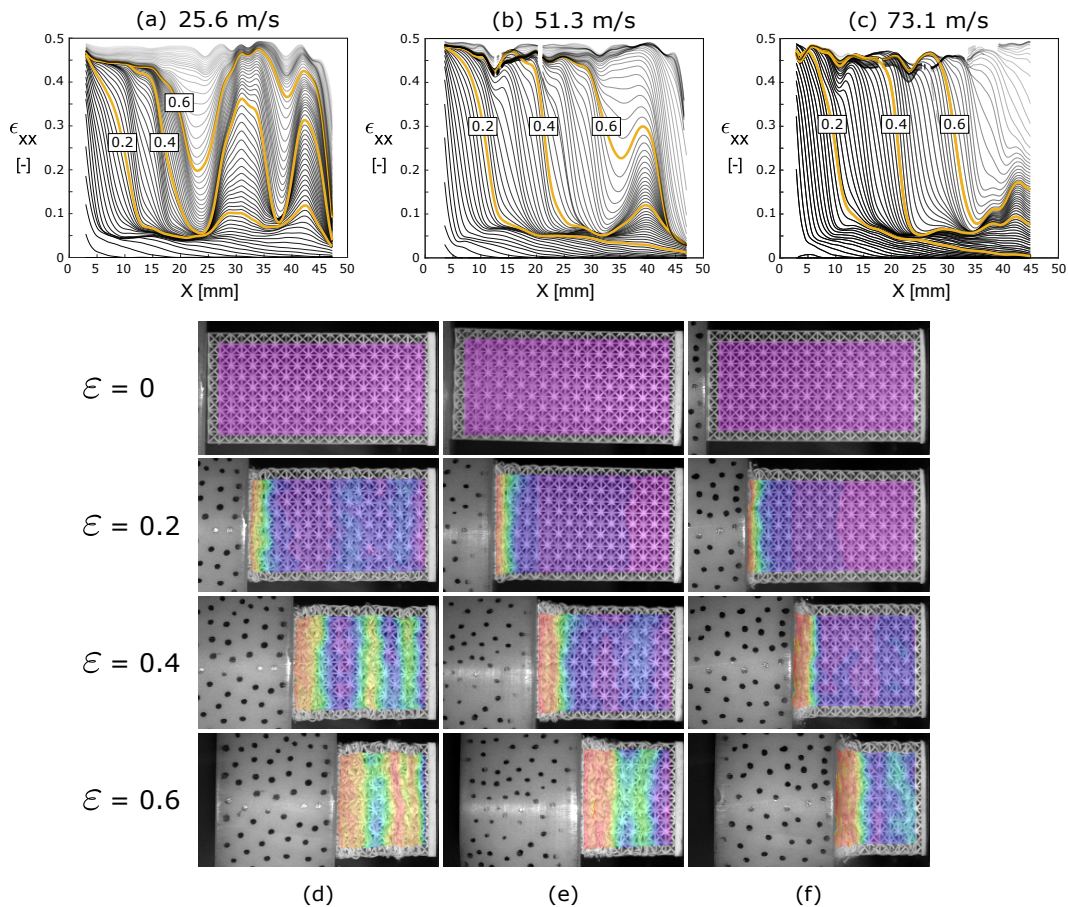
Figure 3.9: Deformation modes of octet-truss topology. Lagrangian strain (ϵ_{XX}) – undeformed coordinate (X) profiles for impact velocity v_i of (a) 25.6 m/s, (b) 51.3 m/s, and (c) 73.1 m/s. Corresponding strain-fields at nominal impact strains of $\varepsilon = 0, 0.2, 0.4$, and 0.6 for v_i of (d) 25.6 m/s, (e) 51.3 m/s, and (f) 73.1 m/s. Line transparency is increased at later time instances to improve data visualization.

For $v_i = 25.6$ m/s, Fig. 3.9(d) shows the initial development of a compaction front at $\varepsilon = 0.2$ and formation of additional deformation bands ahead of the compaction front by $\varepsilon = 0.4$. These bands may be realized through the shape of the $\epsilon_{XX} - X$ profiles in Fig 3.9(a). Figure 3.9(b),(e) show results for $v_i = 51.3$ m/s and similarly show the initial development of a compaction front from $\varepsilon = 0 - 0.4$ and an additional deformation band forming by $\varepsilon = 0.6$. Figure 3.9(c),(f) show results for $v_i = 73.1$ m/s with a clearly propagating compaction front and a slight region of deformation ahead of the deformation front at $\varepsilon = 0.6$. As impact velocity increased, the prominence of the compaction front increased while that of the additional deformation bands decreased. The deformation mechanism of these bands matched the low strain-rate behavior via a buckling response. In contrast, deformation at the compaction front demonstrated more crushing-like behavior.

Figure 3.10 shows the $\epsilon_{XX} - X$ profiles and deformation images taken at $\varepsilon = 0, 0.2, 0.4, 0.6$ for Kelvin lattice specimens impacted at 24.8, 45.8, and 67.3 m/s. For all impact velocities, a compaction front developed and became increasingly prominent as impact velocity increased. The $\epsilon_{XX} - X$ profiles in Fig. 3.10(a) show lines that appear to decrease somewhat linearly. This behavior is more representative of a 'transient dynamic' response than a 'shock' response which will be discussed in Section 3.3.4. The compaction wave also appeared to dissipate in all experiments, represented by non-zero strains ahead of the front. Deformation ahead of the compaction front is visualized in deformation images in Fig. 3.10(d),(e),(f) and showed consistent bending-dominated behavior which was observed in the low strain-rate response.
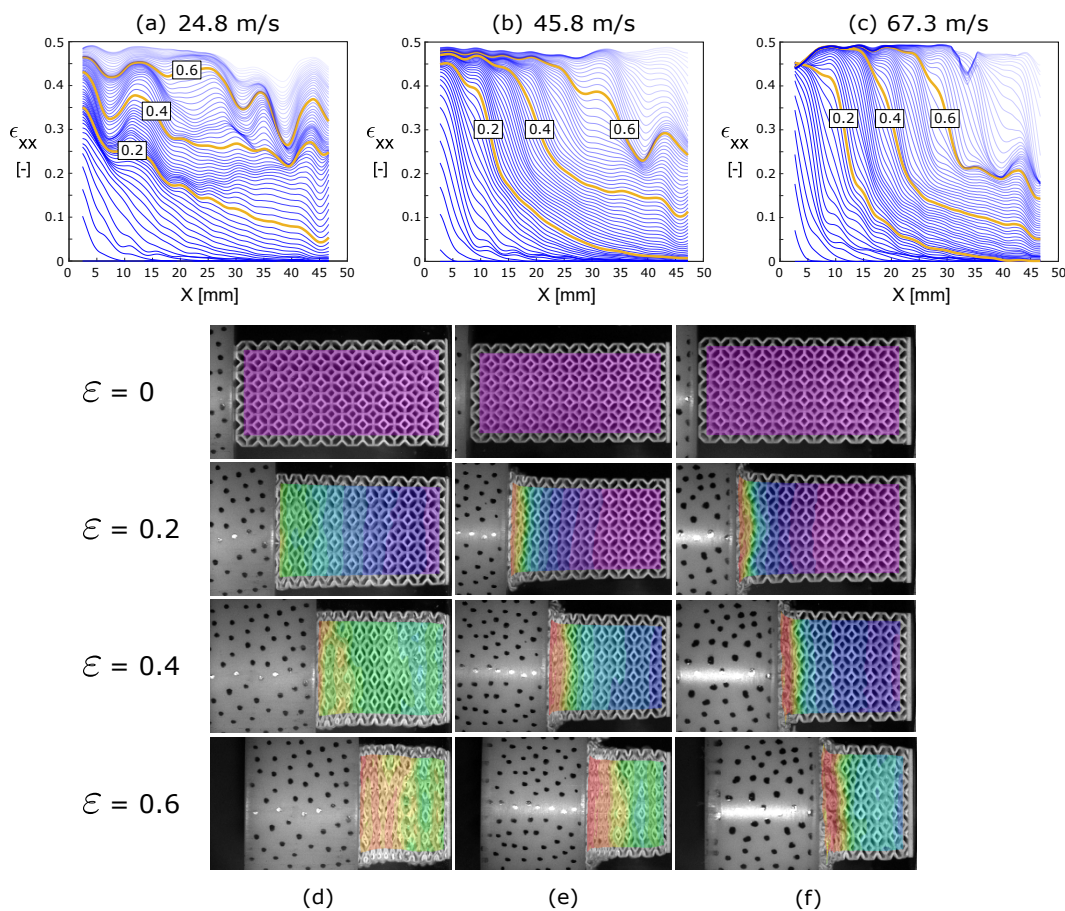
Figure 3.10: Deformation modes of Kelvin topology. Lagrangian strain (ϵ_{XX}) – undeformed coordinate (X) profiles for impact velocity v_i of (a) 24.8 m/s, (b) 45.8 m/s, and (c) 67.3 m/s. Corresponding strain-fields at nominal impact strains of $\varepsilon = 0, 0.2, 0.4$, and 0.6 for v_i of (d) 24.8 m/s, (e) 45.8 m/s, and (f) 67.3 m/s. Line transparency is increased at later time instances to improve data visualization.

Figure 3.11 shows the $\epsilon_{XX} - X$ profiles and deformation images taken at $\varepsilon = 0, 0.2, 0.4,$ and 0.6 for cubic lattice specimens impacted at 24.2, 49.3, and 61.2 m/s. For $v_i = 24.2$ m/s, Fig. 3.11(a),(d) show deformation first initiates at the impact surface and secondly initiates near the distal-most unit cell by $\varepsilon = 0.2$. Compaction then occurs at both these locations similar to what is expected in a low strain-rate response. Figure 3.11(b),(c) and Fig. 3.11(e),(f) show deformation modes for v_i of 49.3 m/s and 61.2 m/s, respectively.
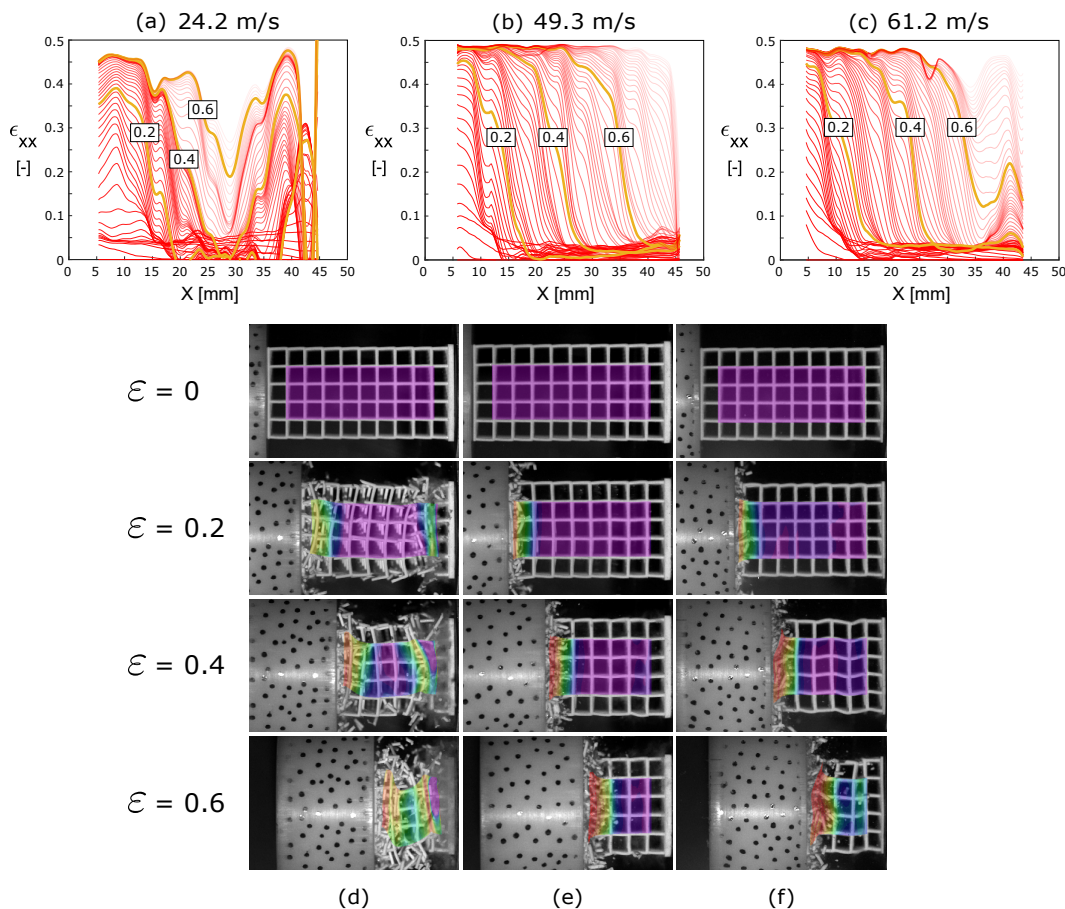
Figure 3.11: Deformation modes of cubic topology. Lagrangian strain (ϵ_{XX}) – undeformed coordinate (X) profiles for impact velocity v_i of (a) 24.2 m/s, (b) 49.3 m/s, and (c) 61.2 m/s. Corresponding strain-fields at nominal impact strains of $\varepsilon = 0, 0.2, 0.4,$ and 0.6 for v_i of (d) 24.2 m/s, (e) 49.3 m/s, and (f) 61.2 m/s. Line transparency is increased at later time instances to improve data visualization.

Unlike at $v_i = 49.3$ m/s (Exp. #CUB_{DI2}) deformation ahead of the front exists and strut fracture was observed at $v_i = 61.2 m/s$ (Exp. #CUB_{DI3}). This may have resulted from manufacturing or geometric defects or a higher relative density of the specimen (Exp. #CUB_{DI3}: 8.942% vs Exp. #CUB_{DI2}: 8.089%) and reflects the influence of structure on the deformation response. In both cases, buckling

followed by brittle fracture of the struts was observed and a clear compaction front developed. As with the Kelvin and octet-truss topologies, the cubic specimen deformation modes were similar to their low strain-rate response.

Full-field strain measurements and varying impact velocities allowed for comparison of the compaction response across topologies. In all topologies, a 'transient dynamic' response occurred at the lowest impact velocity: deformation initiated at the impact surface and additional deformation bands formed ahead of the compaction front. These bands demonstrated deformation mechanisms similar to the lattices' low strain-rate response. A 'shock' response may be generally defined using the ϵ_{XX} – X profiles. A square-wave type curve reflects a strong shock in the material with two distinct regions of uniform strain. The strongest shocks were observed at $v_i \approx 70$ m/s; impacts at $v_i \approx 50$ m/s generally induced deformation which may be realized as a weak shock with two separate regions defined with a lower sloped curve; and impacts at $v_i \approx 25$ m/s induced deformation which should be recognized as (non-shock) compaction. The strongest shocks were found in cubic specimen, followed by octet-truss, and Kelvin specimens based upon the steepness of the ϵ_{XX} – X curves. The shock response of these lattices (considering $v_i > 45$ m/s) is further analyzed in Section 3.3.4.

Some interesting observations are also noted as follows: particularly, strains ahead of the front were higher in Kelvin lattices than other topologies which suggests an increased dissipation effect in this topology; and the cubic topology did not display compaction wave behavior at $v_i \approx 25$ m/s which demonstrates a higher initiation velocity required for a compaction wave response.

Particle Velocity Profiles

Figure 3.12 shows particle velocities from full-field DIC measurements for each direct impact experiment. Particle velocities were plotted for each X-position at all time instances and measurements were taken as the average of 20 Y-pixels about the center of the lattice as discussed in previous sections. Each experimental curve corresponds to data from one X-pixel position and all experimental images.

Flyer velocity was calculated using DIC and plotted for each experiment. As time increased, particle velocities of the lattice specimens converged to the speed of the flyer. Sharp deceleration of the flyer sometimes resulted from hitting the 'stopper' in the experimental set-up such as for the octet-truss specimen at $v_i = 51.3$ m/s (Exp. #OT_{DI2}). Otherwise, flyer velocity appeared to gradually decrease with time
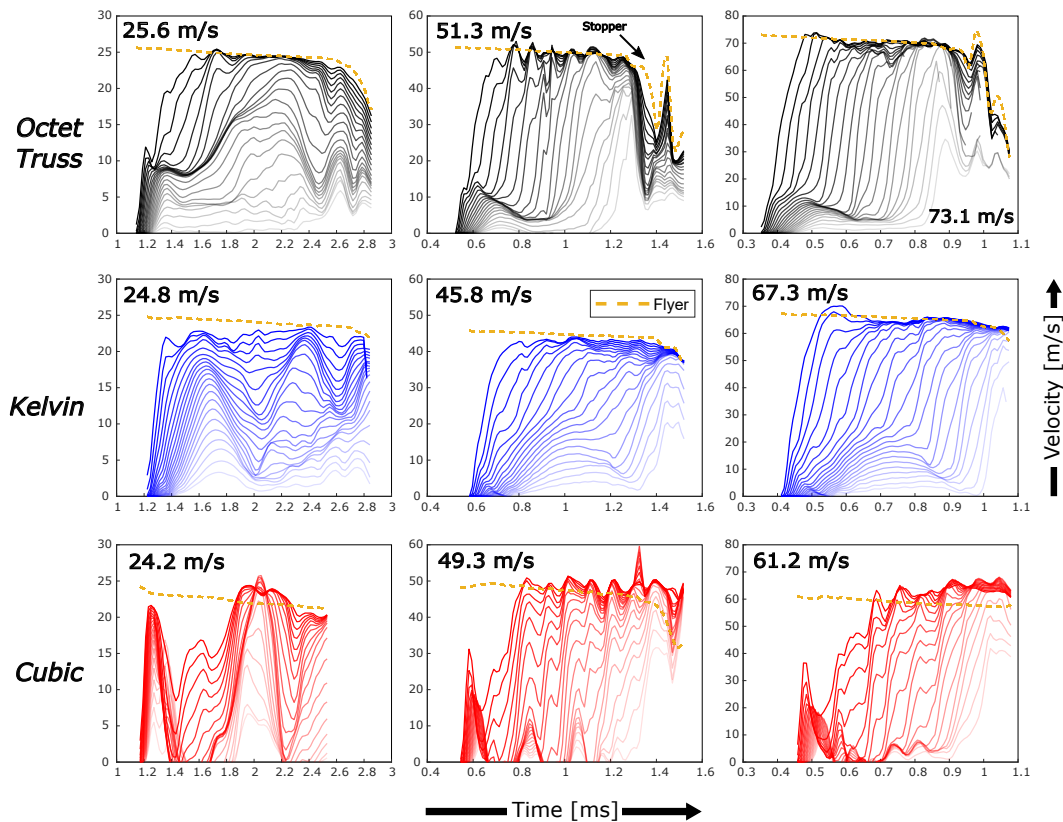
Figure 3.12: Particle velocities of lattice specimens and flyers during direct impact experiments with initial impact velocity shown. Line transparency is increased for larger X-positions to improve data visualization.

due to energy dissipation through deformation of the lattice. Convergence of the lattice particle velocities to the flyer speed is also demonstrated in metallic lattice specimens in Chapter 4 [61] and illustrates a 'structural shock' behavior.

Particle velocities in cubic specimens appeared to exceed that of the flyer which may be attributed to the catastrophic failure mode of the topology and high kinetic energy of the failed struts. Particle velocities in cubic specimen also appeared to take longer to converge to the flyer speed than Kelvin or octet-truss specimens, which represents a longer time for compaction initiation.

Sharper (smaller rise times) velocity profiles illustrate a stronger shock response apparent in experiments at higher impact velocities. Particle velocity profiles showed a precursor wave that decayed before the compaction wave arrived. This precursor wave is related to the elastic wave and plastic response of the lattice specimen and corresponding particle velocities appear to follow trends of low strain-rate behavior shown in Fig. 3.5(a). Cubic specimens showed a steep profile and large drop in value before the compaction shock arrived which is similar to the catastrophic failure

mode observed at low strain-rates. Similarly, Kelvin specimens showed hardening-like profiles and octet-truss specimens showed softening-like profiles resembling the low strain-rate stress-strain ($\sigma_N - \epsilon_N$) behavior.

Stress Histories

The force acting at the distal end of the lattice specimen was found using Eq. (3.3) and strain measurements (ϵ_{SG}) from the HPB. Figure 3.13 shows the nominal stress (σ_N) – nominal impact strain ($\varepsilon = \Delta x_{flyer}/(L - t_b)$) response for each direct impact experiment. Due to varying time durations of experiments, nominal impact strain was used as a comparable quantity. The nominal impact strain represents travel of the flyer normalized by the length of the lattice rather than a representation of the strain field of the specimen. An artifact of this method is that due to wave transit times across the lattice specimen, higher impact velocities induce a larger nominal impact strain before the stress wave arrives at the distal end and a non-zero stress is encountered. Therefore, higher impact velocity experiments may be mistakenly interpreted as exhibiting less stiff responses.
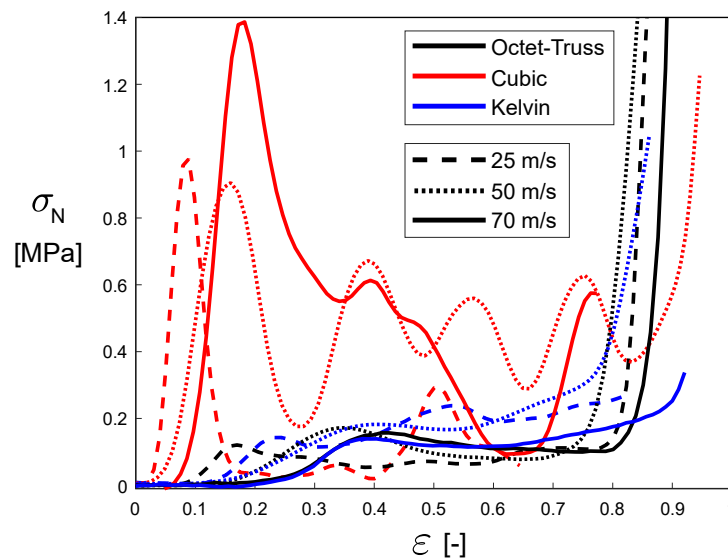
Figure 3.13: Distal nominal stress (σ_N) – nominal impact strain (ε) response for lattice specimens impacted at velocities of approximately 25, 50, and 70 m/s.

Across all topologies, the cubic specimens showed the stiffest and strongest response while the octet-truss and Kelvin specimens exhibited forces commensurate with each other. A slight strengthening may be realized as impact velocity increased, however, variance of force measurements may also be related to relative density of the specimens.

For each topology, force measurements from $v_i \approx 50$ m/s and $v_i \approx 70$ m/s were similar, but differed from force measurements at $v_i \approx 25$ m/s. This observation is in line with the emergence of a dominant compaction (shock) wave at these impact velocities. Overall, force measurements in these experiments resembled trends of the low strain-rate $\sigma_N - \epsilon_N$ behavior of the lattice specimens (Fig. 3.5(a)). Considering specimens with similar relative densities, results show a strain-rate strengthening factor around 15 for cubic specimens, 15 for octet-truss specimens, and 5 for Kelvin specimens.

3.3.4 Shock Response of Lattice Structures

While a compaction wave initiates at the impact surface of all lattice specimens in this work, it is only realized as a shock wave when it exists as the dominant deformation mechanism. This compaction front is also realized as a shock front in metallic octet-truss lattices structures under high impact velocities and the equation of state (EOS) for these materials is defined using a linear shock velocity – particle velocity relation in Chapter 4 [61]. Properties such as density and stress behind the shock front may be found by following one-dimensional continuum shock physics theory using the notions of conservation of mass and momentum [65]. Shock jump relations following the conservation of mass and momentum are shown in Eqs. (3.4) and (3.5) as follows:

$$\llbracket \rho \rrbracket u_s = \llbracket \rho \dot{x} \rrbracket , \tag{3.4}$$

$$\llbracket \rho \dot{x} \rrbracket u_s = \llbracket \rho \dot{x}^2 - \sigma \rrbracket , \tag{3.5}$$

where bracket quantities $\llbracket q \rrbracket$ represent the jump value $(q^+ - q^-)$ across the shock, ρ is the density, $\dot{x}$ is the Eulerian particle velocity, σ is the stress, and u_s is the shock velocity measured in the deformed or Eulerian coordinates. The Eulerian form of the jump conditions were used to account for effects of non-negligible deformation (e.g., strain, particle velocity) ahead of the shock as seen in DIC contours in Figs. 3.9, 3.10, and 3.11.

Parameters necessary to apply the shock jump relations were found using full-field DIC measurements. The shock front was determined by considering the particle velocity $(\dot{x})$ – undeformed (or, Lagrangian) coordinate (X) relation for each experimental image. An example of this data for the Kelvin topology impacted at 67.3 m/s (Exp. #KEL_{DI3}) is shown in Fig. 3.14.
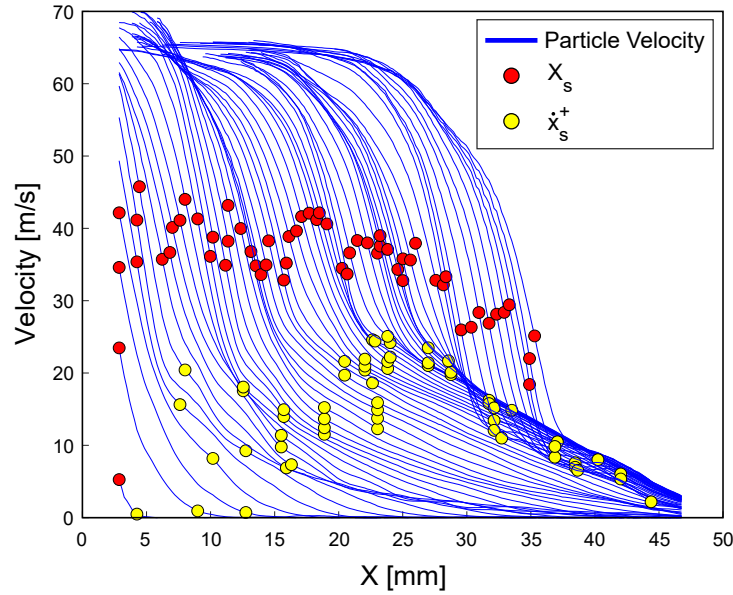
Figure 3.14: Particle velocity ($\dot{x}$) vs. undeformed coordinate (X) profiles for the Kelvin topology impacted at 67.3 m/s (Exp. #KEL_{DI3}) with shock front position (X_s) and particle velocity ahead of the shock ($\dot{x}_s^+$) marked.

Each line in Fig. 3.14 represents data from one experimental image. The shock front was defined as the point of maximum change in velocity for each time instance and the shock velocity was computed using a three-point central difference method on the shock front (X_s) – time (t) history. The shock front was determined for each undeformed coordinate, X, and mapped to the deformed coordinate, x, using displacement measurements, δ, such that $x = X + \delta$. Additionally, the particle velocity ahead of the shock was approximated as the point of maximum curvature ahead of the shock front position.

The density ahead of the shock, ρ_s^+, was found by considering the length of the uncrushed lattice ahead of the shock. This density may be approximated by taking the ratio between the initial length of the uncrushed section of the lattice and the current length of the uncrushed section of the lattice:

$$\frac{\rho_s^+}{\rho_0} = \frac{L - t_b - X_s}{L - t_b + \delta_{anv} - x_s},\tag{3.6}$$

where L is the length of the full specimen, t_b is the thickness of the baseplate, δ_{anv} is the displacement of the anvil, x_s is the deformed coordinate shock front position, X_s is the undeformed coordinate shock front position, and ρ_0 is the initial density of the specimen.

The conservation of mass (Eq. (3.1)) may be rewritten to obtain the density behind the shock (ρ^-) in terms of known parameters:

$$\rho^- = \frac{\rho^+ u_s - \rho^+ \dot{x}^+}{u_s - \dot{x}^-} \ .$$ (3.7)

Figure 3.15(a) shows the density ahead of the compaction wave (ρ_s^+) calculated using Eq. (3.6) and the density behind the compaction wave (ρ_s^-) calculated using Eq. (3.7). The density ahead of the shock remains at a relatively constant value during deformation while the density behind the shock varies widely. Figure 3.14 demonstrates the particle velocity ahead of the shock ($\dot{x}_s^+$) varies widely during loading as well. The density behind the shock, ρ_s^-, is dependent on this particle velocity, $\dot{x}_s^+$, and therefore has a dependence on the lattice topology.
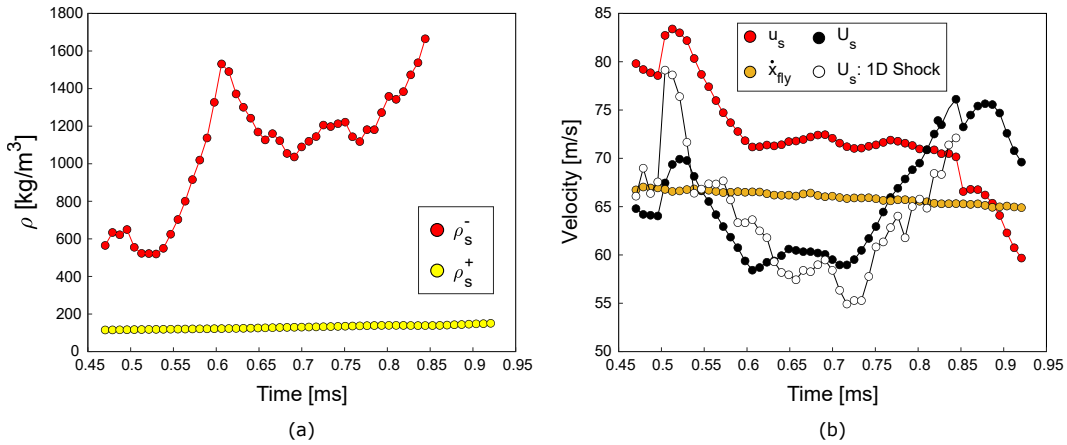
Figure 3.15: Shock parameter-time histories for (a) density behind the shock, ρ_s^-, density ahead of the shock, ρ_s^+, and (b) deformed coordinate shock velocity, u_s, undeformed coordinate shock velocity, U_s, and flyer speed, $\dot{x}_{fly}$ for the Kelvin topology impacted at 67.3 m/s (Exp. #KEL_{DI3}).

Figure 3.15(b) shows the corresponding undeformed coordinate shock velocity (U_s), deformed coordinate shock velocity (u_s), and flyer velocity ($\dot{x}_{fly}$) for a Kelvin specimen impacted at 67.3 m/s (Exp. #KEL_{DI3}). A large difference between the undeformed and deformed coordinate quantities reflects an effect of finite deformations ahead of the shock. These values would converge if no elastic wave or inelastic deformation ahead of the shock existed. The application of 1D shock theory may be evaluated by considering the relationship between these shock velocity quantities [65]:

$$U_s = \frac{\rho_s^-}{\rho_0} \left(u_s - \dot{x}_s^- \right) \ .$$ (3.8)

The Lagrangian shock velocity, U_s, was found using Eq. (3.8) and calculated or measured quantities of ρ_s^+, $\dot{x}_s^-$, and u_s and plotted in Fig. 3.15(b). Based upon velocities shown in Fig. 3.12, the particle velocity behind the shock converged to the speed of the flyer during deformation and therefore may be approximated as the flyer speed, $\dot{x}_{fly}$. Equation (3.8) may be considered as a mapping of the shock speed from u_s (deformed) to U_s (undeformed). Despite large differences between experimentally measured u_s and U_s values, a qualitative match was observed between the experimentally measured U_s values and the 1D shock theory-derived U_s values, which validates application of this theory.

The compaction wave speeds for each experiment are taken as the deformed coordinate shock speed, u_s, and are plotted as a function of flyer velocity in Fig. 3.16. Increasing compaction wave speed was observed with flyer velocity which agrees with other studies on shock compression of foams and lattices [54, 61]. Variation in velocities existed in each experiment due to non-steady shock behavior resulting from initiation and baseplate effects. Based upon this variation, as well as non-constant densities behind the compaction wave, these results are not under the classical classification of a strong shock and are thus described as compaction waves. A general linear trend may resemble the relations shown in Fig. 3.16, however more data points should be collected within the steady shock regime to define a proper $u_s - u_p$ equation of state.
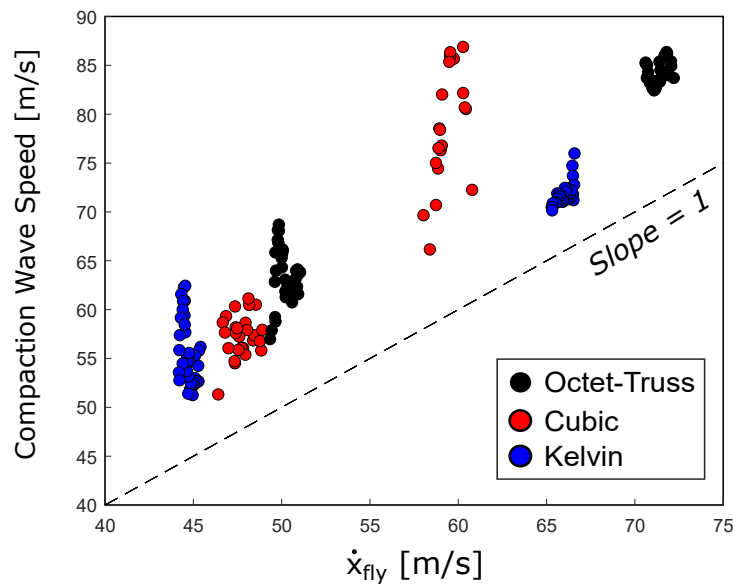
Figure 3.16: Compaction wave speed (taken as deformed coordinate shock velocity (u_s)) vs. flyer velocity ($\dot{x}_{fly}$) for all topologies with impact velocity $v_i > 45$ m/s. Unit slope line drawn for reference.

The stress behind the compaction wave may be found using the conservation of momentum (Eq. (3.5)) and HPB force measurements which were used to approximate the stress state ahead of the shock, σ_s^+. Conservation of momentum may be rewritten to solve for the stress behind the shock in Eq. (3.9):

$$\sigma^- = \sigma^+ + u_s [\![\rho \dot{x}]\!] - [\![\rho \dot{x}^2]\!] . \tag{3.9}$$

Stress versus nominal impact strain histories were computed for experiments with $v_i > 45$ m/s and are shown in Fig. 3.17. Stress acting on the flyer was approximated by taking the product of DIC-computed accelerations and mass of the flyer. It is noted that large scatter existed in the acceleration data and smoothing was implemented in the results. There is general agreement between the 1D shock theory-calculated stress behind the compaction wave and stress acting on the flyer in terms of curve shape and magnitude, which demonstrates 1D shock theory as an appropriate technique to approximate the stress behind the compaction wave.
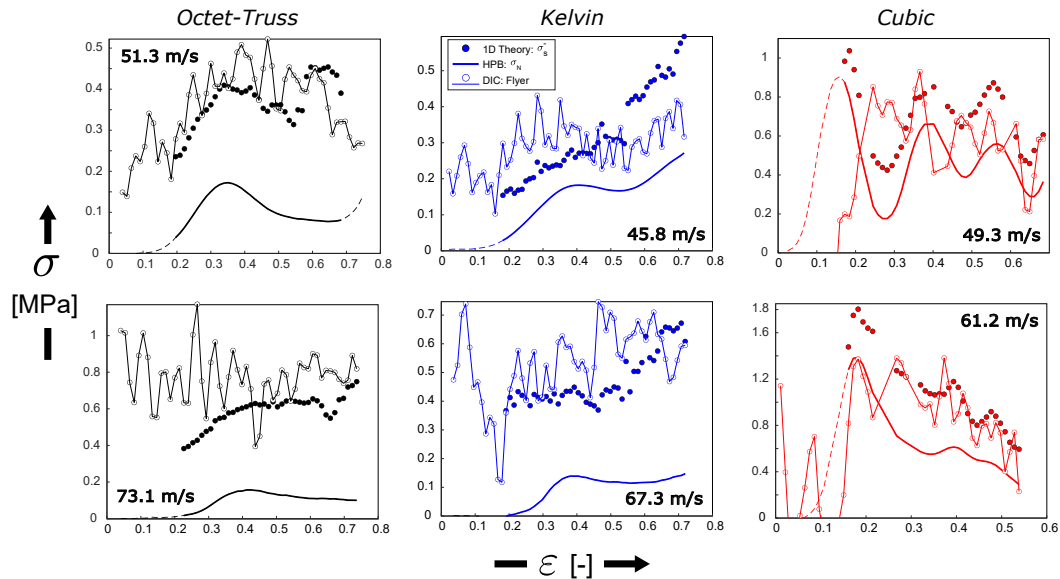
Figure 3.17: Validation of 1D shock theory stress calculations from stress (σ) – nominal impact strain (ε) relations considering stress behind the compaction wave (σ_s^-), HPB nominal stress measurements at the specimen distal face (σ_N), and DIC-computed acceleration based stresses on the flyer. Dotted lines represent HPB data outside duration of shock analysis.

Factors such as air resistance in the chamber or experimental DIC resolution may account for differences in measured values. The stress behind the compaction wave showed higher values than the stress state ahead of the wave, but overall curve shapes were similar. The difference between these values reflects effects of the compaction shock which are significant and caused stress enhancement by a factor of $2 - 3$.

The stress behind the compaction wave is plotted as a function of flyer velocity in Fig. 3.18. A general trend of increasing stress was observed with increasing flyer velocity. The cubic topology demonstrated the highest stress values while Kelvin and Octet-truss topologies showed lower values. A sharp peak in stress was observed for the cubic specimen impacted at 61.2 m/s (Exp. #CUB_{DI3}) due to the strong initial stress ahead of the shock apparent in Fig. 3.17 which may be related to a higher relative density of the specimen. The stress behind the shock strongly depended on the stress state ahead of the shock at these impact velocities. This in turn depends on the lattice topology and base material strain-rate dependent behavior.
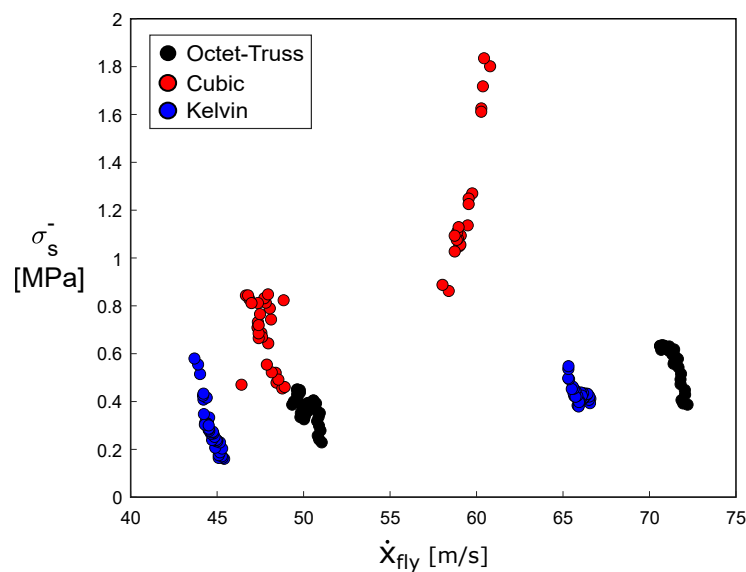
Figure 3.18: Stress behind the compaction wave (σ_s^-) vs. flyer velocity ($\dot{x}_{fly}$) relation for all topologies with impact velocity $v_i > 45$ m/s.

3.4 Summary and Conclusions

The transient dynamic and shock response of polymeric lattice structures of three different topologies was investigated through direct impact experiments with a poly-carbonate Hopkinson pressure bar (HPB), high-speed imaging, and digital image correlation (DIC). Polymeric lattice structures with cubic, Kelvin, and octet-truss topologies were manufactured using Digital Light Processing vat polymerization and characterized at low strain-rates and impact loading. DIC was used to validate elastic HPB analysis as well as analyze the full-field mechanical response of lattice structures. Due to inhomogeneous deformation in lattices, DIC serves as a valuable tool to understand the full-field response and an excellent technique for characterization of cellular materials.

Deformation modes of lattice structures were realized in low strain-rate and impact experiments with unique behavior demonstrated by each topology. Relevant mechanical properties of stiffness, specific energy absorption, failure stress, failure strain, and elastic wave speeds were extracted. At low to moderate impact velocities ($v_i = 25 - 50$ m/s), a mixed deformation mode of a compaction wave and additional deformation band formed in all topologies. At high impact velocities ($v_i > 50$ m/s), a well-defined compaction wave developed and was modeled using 1D continuum shock physics theory. Experimental shock parameters were defined to validate this theory and extract mechanical quantities such as stress behind the compaction wave.

The following conclusions are drawn from this work:

- Polymeric lattice structures demonstrate a transient dynamic deformation regime that includes a compaction wave initiating at the impact surface and dynamic deformation in other sections of the lattice. Higher impact velocities induce a more prominent compaction response.

- Low strain-rate behavior such as stress-strain response and deformation modes (buckling in octet-truss, fracture in cubic, bending in Kelvin) match trends observed in impact experiments and may be used to estimate dynamic behavior. Low strain-rate stiffnesses and elastic wave speeds also correlate between topologies.

- Compaction wave behavior may be modeled as a compaction 'shock' in polymeric lattice structures and 1D theory may be used to calculate the stress at the impacted surface.

- Full-field measurements using digital image correlation allow continuous measurement of the compaction wave which permits characterization of non-steady shock propagation and geometric defects.

- Inertial effects are significant, but not fully dominant, for shock-enhanced stresses. The stress behind the compaction wave largely depends on the state ahead of the wave which demonstrates strain-rate strengthening consistent with the photopolymer base material behavior.

- Different compaction behaviors between topologies illustrate potential for engineering applications. For example, Kelvin lattices dissipated the compaction wave most while cubic lattices showed the highest impact stresses.

This work provides an experimental demonstration of a mixed deformation regime in lattice structures subject to impact loading. Additional experiments on lattices of different topologies and base materials could expand the scope of the study: impact tests with rigid anvils could be used to directly measure stress behind the compaction wave; or additional impact tests at higher velocities could be used to define the steady-state shock $u_s - u_p$ relation. Future work may also entail modeling and development of a simple theory defining lattice structure deformation across a large range of strain-rates. Low strain-rate behavior of lattices drew similarities to dynamic behavior and suggests modeling features such as general hardening, softening, or failure-based responses dependent on topology and base material.

Chapter 4

SHOCK COMPRESSION BEHAVIOR OF STAINLESS STEEL 316L OCTET-TRUSS LATTICE STRUCTURES

Contributions: J.S.W participated in the conception of the project, designed specimens, participated in designing and conducting of experiments, performed the numerical simulations, analyzed the data, and wrote the manuscript.

Abstract

The shock compression behavior of stainless steel 316L (SS316L) octet-truss lattice structures is investigated through experimental techniques and numerical simulations. Plate impact experiments with high-speed imaging are conducted at impact velocities of 270 – 390 m/s on lattice specimens with 5x5x10 unit cell geometries additively manufactured (AM) using direct metal laser sintering. High-speed imaging together with digital image correlation is used to extract full-field measurements and define a two-wave structure consisting of an elastic wave and planar compaction (shock) wave which propagates along the impact direction. A linear shock velocity versus particle velocity relation is found to approximate the measurements with a unit slope and a linear fit constant equal to the crushing speed. The shock velocity versus particle velocity relation, full-field measurements, and elastic limit together with the Eulerian form of the Rankine-Hugoniot jump conditions are used to find relations for the stress and internal energy behind the shock. Stress behind the shock increases with relative density and particle velocity, and specific internal energy converge to a single curve similar to that of bulk AM SS316L. Explicit finite element analysis using the Johnson-Cook constitutive model demonstrates similar shock behavior observed in experiments and a linear shock velocity versus particle velocity relation and corresponding Hugoniot calculations are found to be in agreement with experimental results. Numerical simulations confirm negligible effects of exterior versus interior measurements and further validate the application of one-dimensional shock theory.

4.1 Introduction

Lattice structures demonstrate excellent energy absorption properties across various topologies [14, 97–99] which makes them well suited for impact applications and shock mitigation. The study of shock physics in solid cellular materials, such as foams, honeycombs, or periodic structures, serves as motivation for the analysis of

lattice structures. Rankine-Hugoniot jump conditions for planar uniaxial shocks following the conservation of mass, momentum, and energy have been extensively applied in analytical models of the shock response of foams [52, 64, 100] but only proposed in lattice structures [59]. In metallic foams, Barnes et al. [54] performed experiments and Hugoniot shock analysis on low relative density open-cell aluminum foams using a direct impact split-Hopkinson bar with complementary numerical simulations by Gaitanaros and Kyriakides [55]. They observed a shock developing above some critical impact velocity and computed Hugoniot values agreed with experimental and simulation measurements. Additional simulations by Gaitanaros and Kyriakides [101] on aluminum foams showed dependence of the shock velocity-impact velocity relation, stress behind the shock, crushing energy density, and Hugoniot strain on varying relative density. More recently, plate impact experiments with velocimetry have quantified the compaction shock wave in additively manufactured cellular materials [90], stochastic foams [102], and periodic materials of layered rods [103]. At very high impact velocities, interesting phenomena such as jetting of the periodic structure has also been observed [104].

The shock response of lattice structures has been studied in a limited manner across various length scales and materials. Hawreliak et al. [56] and Lind et al. [57] have conducted experiments on sub-millimeter UC polymeric materials which clearly show a two-wave structure of an elastic precursor wave followed by compaction shock wave. Branch et al. [58] conducted experiments on stainless steel 316L lattices (2x2x3 UC) using phase contrast imaging and demonstrated significant effects of experimental geometries on the shock response. On a smaller scale, Portela et al. [60] investigated impact behavior of nano-scale brittle lattice structures which showed a compaction shock response with distinct regions of intact and densified material. Few shock experiments on metallic lattice structures on the engineering scale (millimeter UC) have been carried out. The shock regime of lattice structures has been introduced, but not fully explored and requires the development of a consistent theory and analysis across length scales and materials.

In this chapter, shock definitions and parameters are developed for lattice structures and 1D uniaxial planar shock theory is applied to stainless steel 316L octet-truss lattice structures on the $O(cm)$ length scale. Normal plate impact experiments are conducted and Rankine-Hugoniot jump conditions are applied for the compaction shock using full-field digital image correlation (DIC) measurements obtained using high-speed imaging. General trends for the Hugoniot field variables are analyzed

per particle velocity and relative density. Explicit finite element analysis is also conducted to shed further light on experiments and the observed trends.

Section 4.2 details the experimental methods of this work through specimen design and characterization, description of normal plate impact experiments, and DIC techniques. Section 4.3 then presents the experimental results and defines and develops Rankine-Hugoniot shock relations for shock velocity, stress, and internal energy of lattice specimens. Section 4.4 presents the framework, results, and Rankine-Hugoniot shock analysis for numerical simulations, and discusses these results to validate effects of exterior versus interior measurements, application of one-dimensional shock theory, and comparison to experiments. Finally, Section 4.5 presents the summary and conclusions of this work.

4.2 Experimental Methods

4.2.1 Specimen Design and Characterization

The design and manufacturing process of lattice structure specimens using an octet-truss unit cell geometry [39] with 5x5x10 UC dimensions and one baseplate is illustrated in Fig. 4.1.
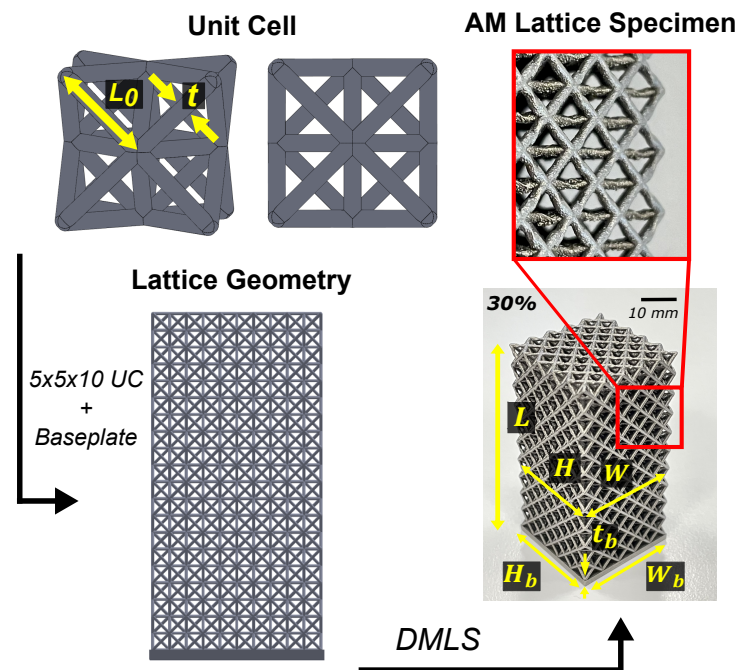
Figure 4.1: Design and DMLS additive manufacturing process of 5x5x10 UC SS316L octet-truss lattice specimens with characteristic length, L_0, strut thickness, t, lattice specimen length, L, lattice width, W, lattice height, H, baseplate thickness, t_b, baseplate width, W_b, and baseplate height, H_b.

Geometries with relative densities, ρ^*/ρ_s, of 10%, 15%, and 30% were designed using SolidWorks (Dassualt Systemes, Providence, RI). A characteristic length, L_0, was maintained in each unit cell geometry while the thickness, t, was varied to modify relative density. Lattice structures were manufactured by Protolabs (Maple Plain, MN, USA) using high-resolution (20 μm layer) direct metal laser sintering (DMLS) AM with stainless steel 316L (SS316L).

Table 4.1 shows relevant physical properties and dimensions of all lattice specimens.

Table 4.1: Design and experimental parameters for lattice specimen characterization. Measured dimensions of each specimen are used to compute the relative density.

#	CAD			Specimen			V_f			V_b			
	$L_0[mm]$	$t[\mu m]$	$\rho^*/\rho_s[\%]$	$m[g]$	$V_{exp}[mL]$	$\rho[kg/m^3]$	$L[mm]$	$W[mm]$	$H[mm]$	$t_b[mm]$	$W_b[mm]$	$H_b[mm]$	$\rho^*/\rho_s[\%]$
$OT10_1$	3.39	440	9.89	27.64	3.71	7450	49.84	24.44	24.44	1.59	24.99	24.97	9.43± 0.27
$OT10_2$	3.39	440	9.89	29.72	3.85	7746	49.89	24.43	24.44	1.65	25.02	25.02	9.74± 0.10
$OT10_3$	3.39	440	9.89	29.62	3.90	7617	49.91	24.45	24.44	1.60	25.01	25.05	9.99± 0.12
$OT10_4$	3.39	440	9.89	28.30	3.68	7710	49.84	24.46	24.49	1.57	25.03	25.04	9.30± 0.21
$OT15_1$	3.39	550	14.99	34.90	4.57	7656	49.81	24.54	24.51	1.53	25.00	24.98	12.40± 0.26
$OT15_2$	3.39	550	14.99	36.93	4.85	7630	49.62	24.47	24.53	1.28	24.93	25.00	13.92± 0.24
$OT15_3$	3.39	550	14.99	37.48	4.89	7677	49.79	24.55	24.56	1.50	25.02	25.02	13.55± 0.28
$OT15_4$	3.39	550	14.99	34.87	4.53	7706	49.79	24.55	24.73	1.48	25.00	25.00	12.28± 0.21
$OT30_1$	3.39	813	29.98	65.85	8.50	7764	50.01	24.77	24.79	1.61	24.97	25.00	25.15± 0.42
$OT30_2$	3.39	813	29.98	66.20	8.81	7535	50.03	24.77	24.77	1.63	24.98	24.99	26.17± 0.24

Relative density was calculated using volume fraction measurements as follows:

$$\rho^*/\rho_s = \frac{V_{exp} - V_b}{V_f} = \frac{V_{exp} - t_b H_b W_b}{(L - t_b)HW} \,, \tag{4.1}$$

where V_{exp} is the experimental volume of the full specimen found by an Archimedes' principle suspension technique [105], V_b is the volume of the rectangular baseplate, and V_f is the space-filling box volume of the lattice. V_b was calculated from thickness, t_b, width, W_b, and height, H_b, of the baseplate and V_f was calculated using the specimen total length, L, width, W, and height, H. Experimental error was computed using measurement uncertainties and error propagation. Mass density values were computed to verify repeatability of measurements and showed good agreement around 7700 ± 100 kg/m^3, slightly lower than the expected value of 7960 kg/m^3 for AM SS316L [35]. Relative density for computer-aided design (CAD) models was calculated using Eq. (4.1) and the corresponding measurements. Due to difficulties in printing small features, experimental relative densities showed significant deviation from CAD values ranging from 7% for $OT10$, 10% for $OT15$, and up to 15% for $OT30$.

4.2.2 Normal Plate Impact Experiments

Normal plate impact experiments with high-speed imaging were conducted at varying impact velocities for specimens with nominal relative densities $\rho^*/\rho_s = $ 10%, 15%, and 30%. A slotted 38.7 mm bore diameter powder gun was used with 76.2 mm long and 38.7 mm diameter aluminum 6061 projectiles (flyers) to impact lattice specimens at velocities of 270-390 m/s in a chamber with a transparent polycarbonate (PC) window. Figure 4.2 illustrates the experimental set-up. Lattice specimens were epoxied to an aluminum target holder and attached to a mounting gimbal by alumina rods.
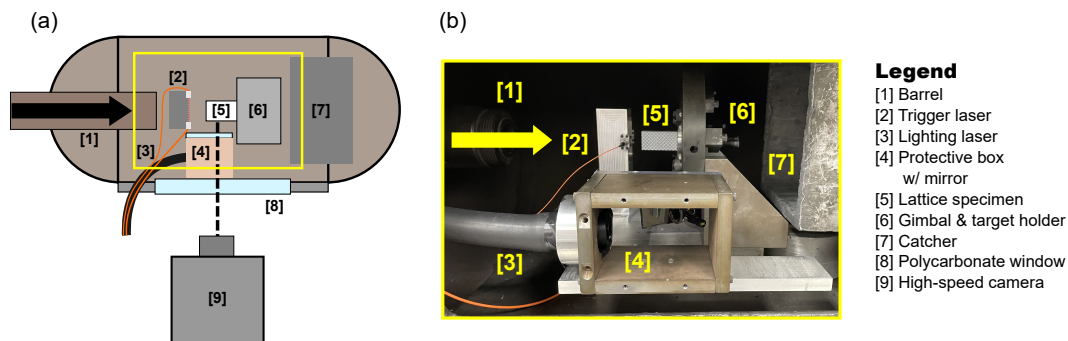
Figure 4.2: Normal plate impact powder gun experiments on lattice specimens: (a) schematic of set-up and (b) photograph of laboratory set-up. One side of the protective box is removed for visibility.

Experimental images were captured using a Hyper Vision HPV-X2 high-speed camera (Shimadzu, Kyoto, Japan) with a Nikon 70-300mm f/4.5-5.6G lens and lighting from a non-coherent CAVILUX Smart laser (Cavitar, Tampere, Finland) with 40 ns pulse lengths which provided sufficient lighting and prevented motion blur. A protective box with an interior mirror was used to protect the Cavitar laser and redirect light onto the test specimen through a small PC window. 128 images (400x250 pixels (px)) were captured at a constant framing rate (500,000 to 800,000 frames per second) set to maximize the number of images taken normal to the side of the lattice through the PC window during shock compression of the lattice specimen. The framing rate of the high-speed camera was determined by setting the framing interval, Δt, based on target impact velocities of 270, 300, 330, and 380 m/s. Experimental image capture was triggered using an Agilent MSO9404A oscilloscope (20 GSa/s sample rate), Wilcom F6230A visual fault locator, and Thorlabs PDA10A2 photodiode. Interruption of the laser (placed ahead of the specimen) by the flyer caused a measured voltage drop which triggered after a 1 μs time duration.

4.2.3 Digital Image Correlation

An example of experimental images taken during impact is shown in Fig. 4.3 and full deformation can be visualized in Supplementary Video S3. 2D digital image correlation (DIC) was performed on the high-speed images using Vic2D (Correlated Solutions, Columbia, SC, USA). Lattice specimens were painted white to improve contrast in experimental images and a random speckle pattern was applied to each flyer. There were two areas of interest (AOI) for these experiments; AOI1: over the flyer used to track rigid flyer displacements, and AOI2: over the lattice specimen to track specimen particle displacements. A random speckle pattern was applied to the flyer using a Sharpie pen (Fine Point) and produced unique subsets for correlation analysis of AOI1, while the lattice geometry itself was used for correlation of AOI2. A subset size of 29 px (4.35 mm) was used for AOI1 and 23 px (3.45 mm) for AOI2 (corresponding to ≈3/4 of a unit cell) and step size of 1 px with incremental correlation was used in both analyses. Due to the inherent periodicity of the lattice specimen, DIC was able to correlate AOI2 subsets that were smaller than a unit cell with seed points placed away from the impact surface. A maximum error of 0.15 px was set to remove highly decorrelated regions.
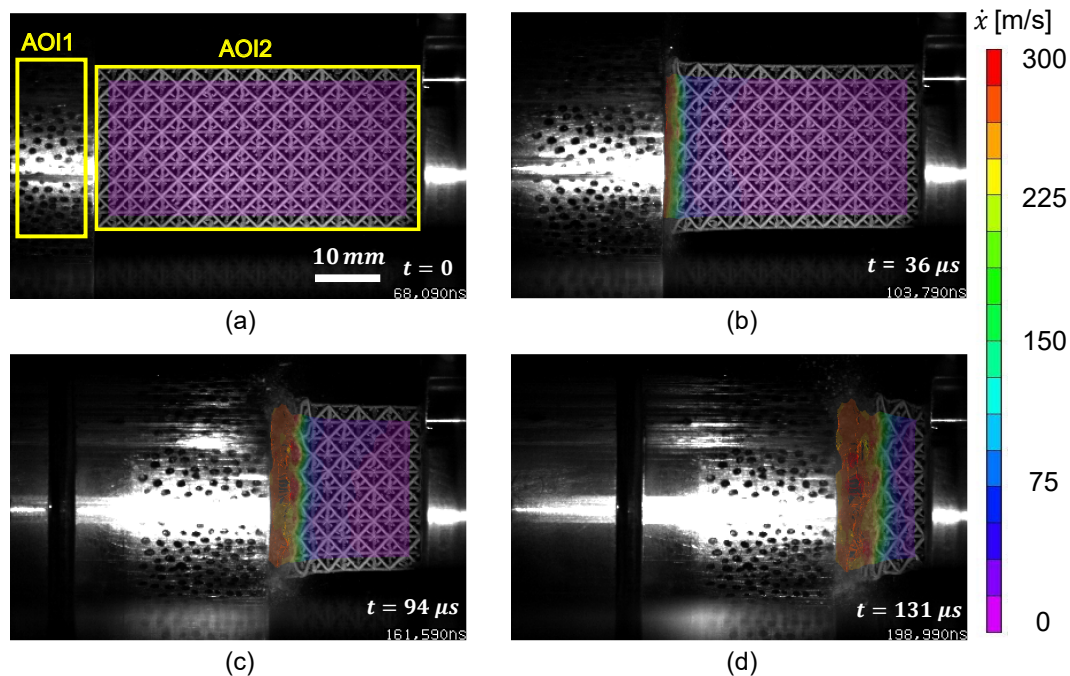
Figure 4.3: Experimental images for $\#OT15_2$ at $V_{impact} \approx 300 m/s$ and $\rho^*/\rho_s \approx 15\%$ with (a) DIC areas of interest and (b)-(d) full-field measurements for particle velocity at time instances, $t = 0, 36\mu s, 94\mu s$, and $131\mu s$ after impact.

Some image distortion through the polycarbonate (PC) window was expected. Therefore, calibration images were taken without the PC window and used to measure actual specimen dimensions using ImageJ [106]. These values were then used as calibration lengths in the DIC analyses. The particle velocities of both AOI are then numerically computed by applying the three-point central difference method on the measured displacements at the constant framing rate. Figure 4.3(b)-(d) shows the DIC results for particle velocity for experiment $\#OT15_2$ on a $\rho^*/\rho_s \approx 15\%$ specimen at $V_{impact} \approx 300$ m/s. A clear compression shock front is visible in the images represented by the discontinuity of crushed and non-crushed regions of the specimen. This discontinuity can also be realized through the overlaid particle velocities which show near zero values ahead of the front and high constant values behind the front. Due to the large amount of deformation, some regions lose correlation and values are removed from the results illustrated by the 'holes' in later images.

4.3 Experimental Results and Discussion

The experimental matrix for this study is shown in Table 4.2. Four impact velocities are tested for 10% and 15% specimens, and two for 30% specimens. The velocities of the flyers were extracted from each experiment using DIC displacements, and the set Δt and corresponding FPS are shown.

Table 4.2: Experimental matrix with frames per second (FPS) determined by setting the framing interval (Δt) of the high-speed camera to maximize images captured during deformation by a flyer traveling at the impact velocity, V_{impact}. The specimens are designated as $OTPP_Q$ where PP and Q are the nominal relative density (%) and experiment number for that density, respectively.

#	$\Delta t\,[ns]$	FPS	$V_{impact}\,[m/s]$
$OT10_1$	1900	526,320	270
$OT10_2$	1700	588,240	303
$OT10_3$	1500	666,670	331
$OT10_4$	1300	769,230	381
$OT15_1$	1900	526,320	265
$OT15_2$	1700	588,240	295
$OT15_3$	1500	666,670	331
$OT15_4$	1400	714,290	391
$OT30_1$	1700	588,240	290
$OT30_2$	1400	714,290	381

4.3.1 Wave Definitions and Extraction

Similar to shock behavior in bulk materials [17], a two-wave structure consisting of (1) an elastic wave, and (2) a compaction (shock) wave was observed during experiments. Similar observation has been well documented in polymeric lattice structures on the sub-millimeter scale impacted around 200-600 m/s. [56, 57]. The elastic wave and shock wave may be defined and the corresponding locations can be extracted using full-field displacement and velocity measurements. Ravindran et al. have used this technique to accurately define elastic and shock fronts in aluminum foams [93]. Full-field measurements were averaged over the center (middle) row of unit cells to approximate a uniaxial bulk material response. Displacement and velocity measurements were taken as the average over 30 y-pixel (vertical) positions corresponding to the center UC, for each x-pixel (horizontal) position.

The elastic wave front was defined using a 15 μm displacement criterion based on the maximum observed DIC error (confidence interval) of 0.1 px and average image scale of 0.15 mm/px. The confidence interval for all experiments remained under 0.1 px during elastic deformation and therefore the criterion is larger than the experimental resolution. Wave definition and extraction for experiment #$OT15_2$ is shown in Fig. 4.4.

Figure 4.4(a) shows particle displacement plotted against horizontal position (Lagrangian/undeformed coordinate) defined using the impact surface as $X = 0$ and time of impact as $t = 0$. Each line represents a single time-instance taken from one experimental image and the marker represents the position of the elastic front. A stricter or looser displacement criterion may slightly alter results, however the steepness and consistent spacing of displacement profiles imply similar results for criteria of 10-20 μm.

The shock front and relevant parameters are defined in both position and time and visualization is shown in Fig. 4.4(b). Figure 4.4(c) shows the particle velocity (u_p) – time (t) history of all material points (x-pixel positions). Each material point of the specimen shows an initial low-amplitude particle velocity from the elastic wave followed by steep acceleration to a nearly constant particle velocity similar to the flyer speed. The shock front was defined for each material point as the point of largest change in velocity–equal to infinity in the case of a mathematically sharp shock. Based upon this definition, the shock front may be defined: with respect to time for one material point (pixel), or with respect to position for one time instance (image).
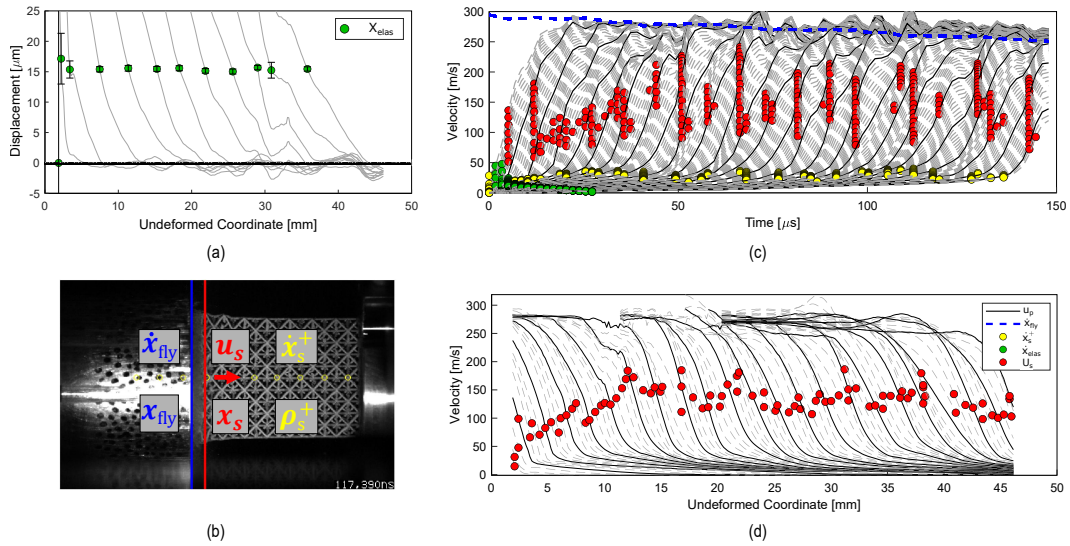
Figure 4.4: Wave definition and extraction for experiment #$OT15_2$: (a) displacement position profiles with 15 μm displacement criterion marking the location of the elastic wave front (X_{elas}); (b) visualization of the shock definition and relevant parameters; and DIC particle velocity (u_p) profiles with respect to (c) time and (d) undeformed (Lagrangian) coordinate, with the elastic wave ($\dot{x}_{elas}$), flyer ($\dot{x}_{fly}$), velocity ahead of the shock ($\dot{x}_s^+$), and shock front (U_s) marked. Every 10th line is highlighted to improve data visualization.

Figure 4.4(c) shows particle velocities with respect to time (i curves of j data points) and Fig. 4.4(d) shows particle velocities with respect to position (j curves of i data points) where i is the number of horizontal pixels in experimental images ≈ 200 and j is the number of images analyzed ≈ 90. Every 10th line is highlighted to improve data visualization. Determination of the shock front using du_p/dt caused 'lines' of front positions to emerge in Fig. 4.4(c) due to the low temporal resolution from the limited number of experimental images. Determination of the shock front using du_p/dX improved extraction of the shock wave as shown in Fig. 4.4(d) due to an increased spatial resolution ($i > j$). The particle velocity ahead of the shock, $\dot{x}_s^+$, was determined from the particle velocity-time history as the point of maximum change in curvature before the shock front.

The wave fronts were extracted and plotted against time as shown in Fig. 4.5(a) and visualized using experimental images in Supplementary Video S4. The elastic wave front (X_{elas}) was determined using the displacement criterion, the flyer front (x_{fly}) was determined using displacement measurements of the flyer, and the Lagrangian shock front (X_s) was determined using the spatial derivative technique in Fig. 4.4(d). The term "Lagrangian" is used to describe parameters defined using the undeformed coordinate system while the term "Eulerian" is used to describe parameters defined

using the deformed coordinate system. The Eulerian shock front (x_s) can be determined by mapping the Lagrangian shock front to the deformed coordinate system using full-field displacement (δ) measurements: $x_s = X_s + \delta$. Flyer speed and shock velocities were computed from the front-time histories using a three-point central difference method. Figure 4.5(b) shows the calculated flyer speed, Lagrangian shock velocity (U_s), and Eulerian shock velocity (u_s) as a function of time with the steady shock defined from time t_1 to t_2 to avoid edge or smoothing effects.

(a)   (b)
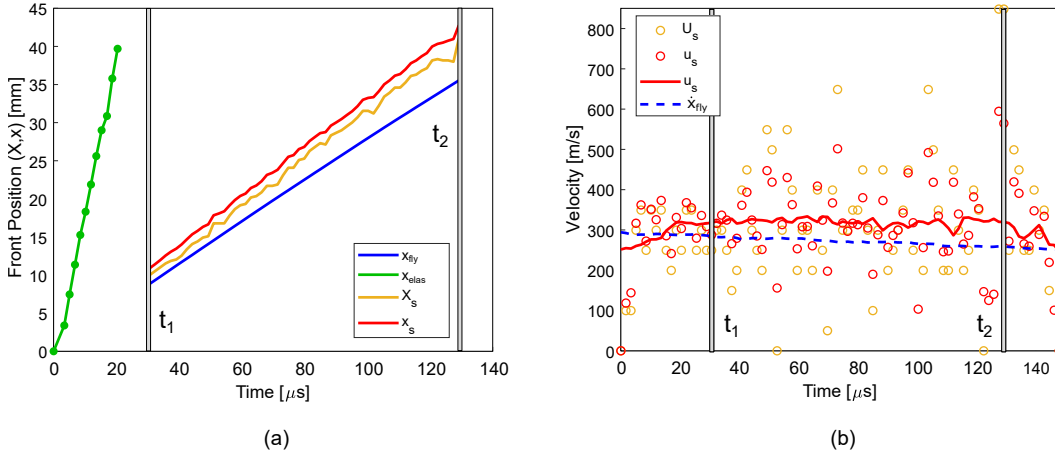
Figure 4.5: Wave front position and velocity profiles: (a) elastic (X_{elas}), flyer (x_{fly}), Lagrangian shock (X_s), and Eulerian shock (x_s) front-time histories; and (b) corresponding flyer speed ($\dot{x}_{fly}$) and shock velocities in the Lagrangian (U_s) and Eulerian (u_s) configurations computed using a three-point central difference method. A 20% moving mean window was applied to smooth experimental scatter of Eulerian shock velocities (u_s) indicated by the red solid line.

Deceleration of the flyer was observed in all experiments and scatter plots of the shock velocities showed large variations in values. These variations may largely be attributed to noise in experimental front locations combined with small timesteps used in numerical derivative calculations. Eulerian shock velocities were smoothed with a 20% moving mean window to eliminate scatter and resemble the smoothness of the flyer speed. Front positions appear mostly linear in time which supports the formation of a steady shock in the lattice specimens and justifies smoothing of data.

Experimental Elastic Wave Speeds

Elastic wave speeds were computed using a linear fit of the elastic front time history and error is reported as the 95% confidence interval of the fit. Results for all experiments are shown in Fig. 4.6. There is a clear trend showing positive correlation between elastic wave speed and relative density which agrees with positive stiffness

correlation with relative density found in lattice structures [4]. However, this trend inherently depends on manufacturing defects and geometry which control the stiffness and density of the specimen. Impact velocity does not appear to influence the wave speeds which agrees with results from other studies [57]. This also implies AM SS316L does not demonstrate strain-rate stiffening effects.
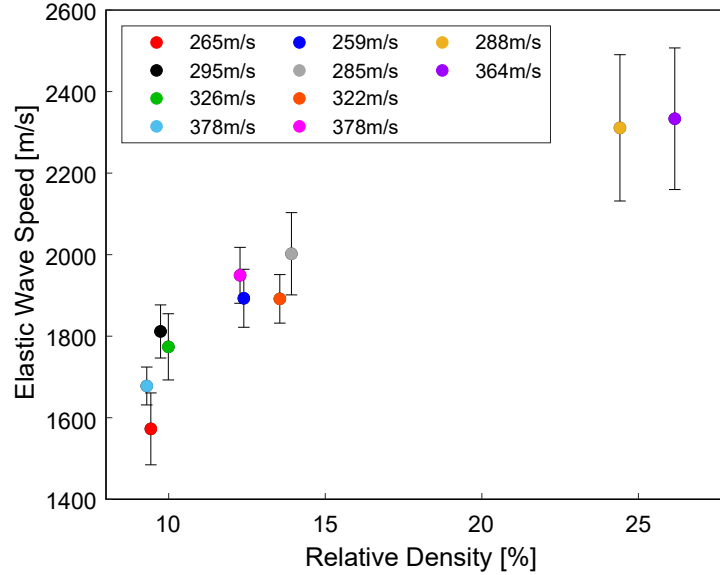
Figure 4.6: Elastic wave speed as a function of relative density for all experiments. Elastic wave speeds were computed using a linear fit of the elastic front time-history and error is reported as the 95% confidence interval of the fit.

4.3.2 Rankine-Hugoniot Shock Analysis

Rankine-Hugoniot jump conditions were used to analyze the shock compression behavior of lattice specimens. Full-field displacement measurements were used to map between the undeformed and deformed coordinate systems and allowed for extraction of field variables ahead and behind of the shock. These measurements allow for application of the Eulerian forms of the jump conditions following the conservation of mass, momentum, and energy [65]:

$$\llbracket \rho \rrbracket u_s = \llbracket \rho \dot{x} \rrbracket , \tag{4.2}$$

$$\llbracket \rho \dot{x} \rrbracket u_s = \llbracket \rho \dot{x}^2 - \sigma \rrbracket , \tag{4.3}$$

$$\llbracket \rho \left(\mathcal{E} + \frac{1}{2} \dot{x}^2 \right) \rrbracket u_s = \llbracket \rho \left(\mathcal{E} + \frac{1}{2} \dot{x}^2 \right) \dot{x} - \sigma \dot{x}^2 \rrbracket , \tag{4.4}$$

where bracket quantities $\llbracket q \rrbracket$ represent the jump value $(q^+ - q^-)$ across the shock, ρ is the density, $\dot{x}$ is the particle velocity, σ is the stress, and $\mathcal{E}$ is the specific

internal energy. The Eulerian form of these equations was considered to account for the effect of the elastic wave on shock behavior, namely the propagation of the shock into non-quiescent material. Significant deviation of the Eulerian shock front and Lagrangian shock front in Fig. 4.5(a) illustrates a non-negligible effect. The difference in shock fronts is visualized in Supplementary Video S4 showing the shock and flyer fronts overlaid on experimental images. The Eulerian (deformed) coordinates show a true tracing of the shock that accounts for elastic deformation.

Shock Velocity (u_s) **– Particle Velocity** (u_p) **Relation**

Full Hugoniot characterization was carried out using known or approximated states ahead of the shock, conservation equations Eqs. (4.1)-(4.4), and an additional relation between shock velocity, u_s, and particle velocity, u_p. u_s is the Eulerian shock velocity shown in Fig. 4.5(b) and the particle velocity behind the shock, u_p, was approximated by the flyer speed, $\dot{x}_{fly}$, at the same time instant. This approximation is based on the convergence of particle velocities to the flyer speed as seen in Fig. 4.4(c). The $u_s - u_p$ relation is shown in Fig. 4.7 for all experiments. Each data point represents a single time instance at which particle velocities were computed from one experimental image. Smoothed data with a 20% moving mean window was used in the final results.
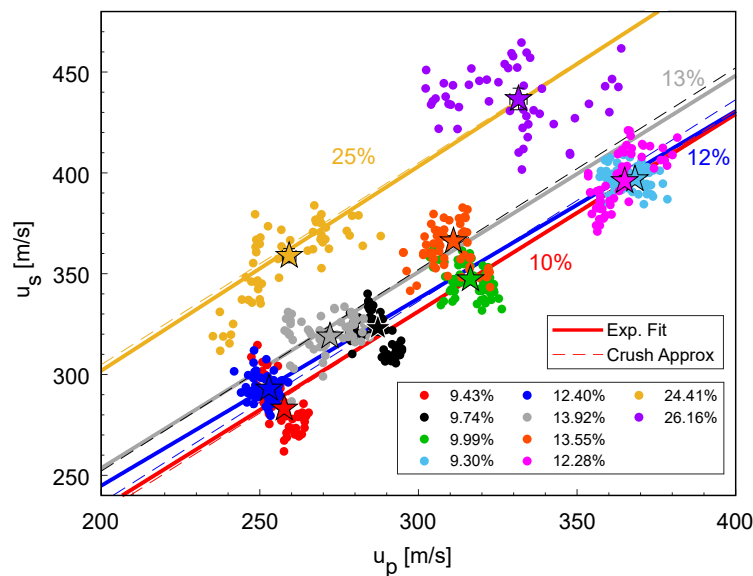
Figure 4.7: Eulerian shock velocity (u_s) – particle velocity (u_p) relation for all specimens and linear fits for $\rho^*/\rho_s = 10\%, 12\%, 13\%$, and 25%. Each data point corresponds to a measurement from one experimental image and stars represent linearized approximations. Dotted lines show the 'crushing speed approximation' discussed in Section 4.3.2.

Significant deceleration of the flyer induced a range of u_p during experiments. Linearized approximations were found by taking a linear fit of the flyer and shock fronts in Fig. 4.5(a) and are shown as stars in Fig. 4.7. A linear fit was also applied to scatter data to define the $u_s - u_p$ relation. While there was significant scatter in the results, the linear fit shows good agreement with linearized values. This agreement suggests experimental noise as the major cause of variation and will be further discussed and validated in Section 4.4.3 of the finite element analysis results.

The linear fit of the data was computed for four groups of relative density, 10% ($OT10_1 - OT10_4$), 12% ($OT15_1, OT15_4$), 13% ($OT15_2, OT15_3$), and 25% ($OT30_1, OT30_2$). Two groups (12%, 13%) were considered from the CAD 15% specimens due to a significant 10% difference in measured relative density values. The linear fit is of the form:

$$u_s = m + Su_p,\qquad(4.5)$$

where m is the constant coefficient and S is the slope of the relation. Experimental results for these fits are shown in Table 4.3 with error found using 95% confidence bounds. The slope, $S \approx 1$ for all relative densities and m increased with relative density for Eulerian coordinate parameters. A consistent S value and positive correlation of m with relative density matches trends observed in simulation of aluminum foams [101]. The Lagrangian shock relations are shown for comparison and demonstrate similar values for S but no trend for m can be determined due to high errors. Lagrangian and Eulerian fit parameters are further compared and discussed in simulation results in Section 4.4.2.

Table 4.3: Linear fit parameters for experimental linear shock velocity (u_s, U_s) – particle velocity (u_p) relations of Eulerian, x, and Lagrangian, X, coordinate systems for $\rho^*/\rho_s = $ 10%, 12%, 13%, and 25%.

ρ^*/ρ_s [%]	m_x	S_x	m_X	S_X
10	37.98 ± 12.71	0.978 ± 0.041	50.02 ± 25.83	0.923 ± 0.084
12	59.09 ± 9.52	0.929 ± 0.030	59.89 ± 17.00	0.894 ± 0.054
13	58.99 ± 30.43	0.973 ± 0.105	58.97 ± 54.6	0.940 ± 0.188
25	99.15 ± 28.37	1.014 ± 0.096	50.83 ± 39.98	1.107 ± 0.136

Crushing Speed Approximation

Most bulk materials typically follow a linear $u_s - u_p$ relation with $m \approx c_0$, where c_0 is the bulk sound speed of the material [65]. Elastic wave speeds $c_{elas} \approx$ 1600-2400 m/s in the lattice specimens (Fig. 4.6) are much higher than the fitted $m \approx$

30-100 m/s values in Table 4.3. This constant, m, is therefore not equivalent to the bulk sound speed of the material, but may be physically interpreted by assuming $S \approx 1$. An S value of approximately one suggests a constant compaction strain in the shocked region and modeling the lattice as an elastic-plastic rigid-locking crushable material [64] where the particle velocity behind the shock is equal to the flyer speed. Taking $S = 1$ in Eq. (4.5), m can be rewritten:

$$m = u_s - u_p = \frac{d}{dt}(x_s(t) - x_{fly}(t)) = \frac{d}{dt}x_c(t), \qquad (4.6)$$

where the shock velocity (u_s) and particle velocity (u_p) can be rewritten as time derivatives of the front locations, $x_s(t)$ and $x_{fly}(t)$, and the distance $x_s(t) - x_{fly}(t) = x_c(t)$ is recognized as the crushed width of the lattice specimen computed as the distance between the shock front and flyer front. The constant m can then be interpreted as the slope of a linear fit to the crush width-time history, or, a constant crushing speed. Figure 4.8(a) shows the crushing width versus time plots for all experiments. Experimental curves show some noise, but a linear fit can be applied. The linear fit is shown through dotted lines in Fig. 4.8(a) and the slope of the plots are extracted in Fig. 4.8(b) and plotted against relative density.
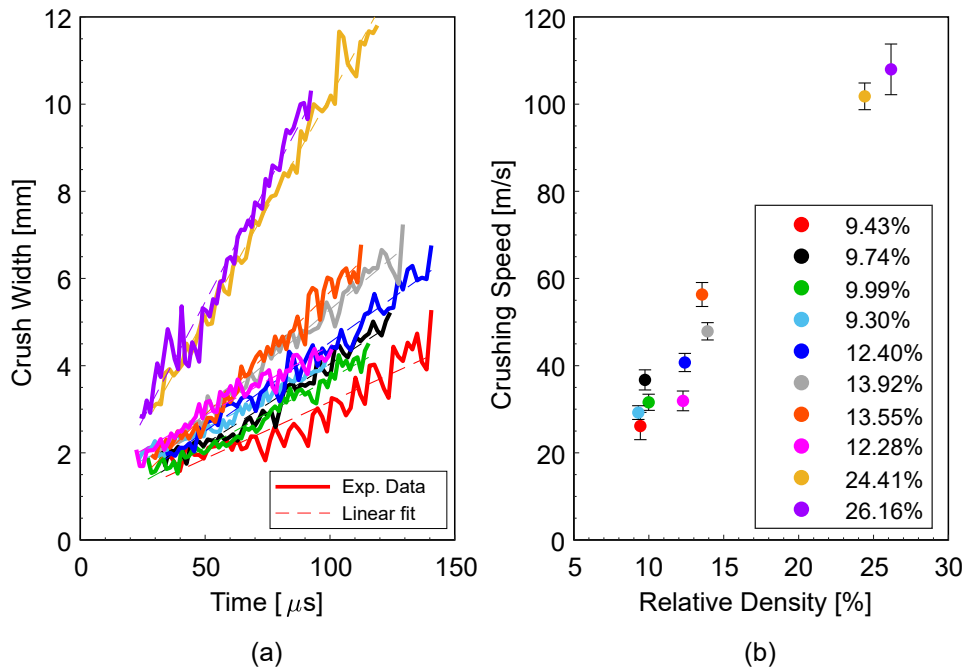
Figure 4.8: Lattice specimen crush width and crushing speed relations: (a) crush width (distance between flyer and shock front) of shocked specimens as a function of time with linear fit lines; and (b) crushing speed (slope of linear fit of crush width time history) plotted against relative density.

The crushing speed shows a strong positive correlation to relative density and values show good agreement with the calculated fit values for m. Using $S = 1$ and m as the crushing speed may serve as a general approximation for the linear $u_s - u_p$ relation of lattice materials. These approximations are applied for $\rho^*/\rho_s = 10\%, 12\%, 13\%$, and 25% by taking m as the average value for each group and are plotted as dotted lines alongside experimental fits in Fig. 4.7. These approximations show good agreement with experimental fit lines within the range of particle velocities.

Hugoniot Relations for Stress and Internal Energy

Stress and internal energy Hugoniot relations can be developed for both elastic and shock waves with the elastic wave treated as a weak shock into a quiescent material and the shock wave treated as a strong shock into a non-quiescent material. In the elastic case, $u_s = c_{elas}$ where c_{elas} is the measured elastic wave speed and independent of impact velocity.

The density ratio ahead of the shock, ρ^+/ρ_0, was approximated by the ratio of the length of the uncrushed region in the deformed coordinate to the length of the uncrushed region in the undeformed coordinate. These lengths were found as the distance between the shock fronts and non-impacted face of the lattice such that: $\rho^+/\rho_0 = (L - t_b - X_s)/(L - t_b - x_s)$ with specimen length, L, and baseplate thickness, t_b. Using full-field measurements of $\dot{x}^+, \dot{x}^-, u_s, \rho^+$, and conservation of mass (Eq. (4.1)), the density behind the shock, ρ^-, may be determined:

$$\rho^- = \frac{\rho^+ u_s - \rho^+ \dot{x}^+}{u_s - \dot{x}^-} \ . \tag{4.7}$$

It is assumed the elastic wave propagates into quiescent material, or, $\dot{x}^+_{el} = 0$. The particle velocity behind the elastic wave, $\dot{x}^-_{el}$, was defined as the corresponding velocity at which the material point satisfies the displacement criterion. Divergence of velocity values was observed for initial data points and so a constant value was approximated for $\dot{x}^-_{el}$ from the fourth image of each experiment (approximately deformation of 1/2 unit cell). The velocity ahead of the shock, $\dot{x}^+_s$, was determined from the particle velocity-time history as the point of maximum change in curvature before the shock front chosen to most accurately depict the velocity. Particle velocities ahead of the shock in Fig. 4.4(c) appeared to gradually increase in time. This may be related to material properties such as plasticity or experimental conditions such as lateral movement of the specimen and must be accounted for in the analysis.

Assumption or measurement of the stress ahead of the shock, σ^+, and conservation of momentum (Eq. (4.3)) may be used to find the stress behind the shock, σ^-:

$$\sigma^- = \sigma^+ + u_s [\![\rho\dot{x}]\!] - [\![\rho\dot{x}^2]\!] . \tag{4.8}$$

The stress behind the elastic wave, σ_{el}^-, was calculated assuming quiescent initial conditions and used to approximate the stress ahead of the compaction shock, σ_s^+. Equation (4.8) was solved for each data point for the $\sigma_s^- - u_p$ relation shown in Fig. 4.9 and σ_s^- showed a positive correlation with relative density and particle velocity. Increasing the relative density at a constant particle velocity caused a larger increase in stress than increasing particle velocity at a constant relative density.
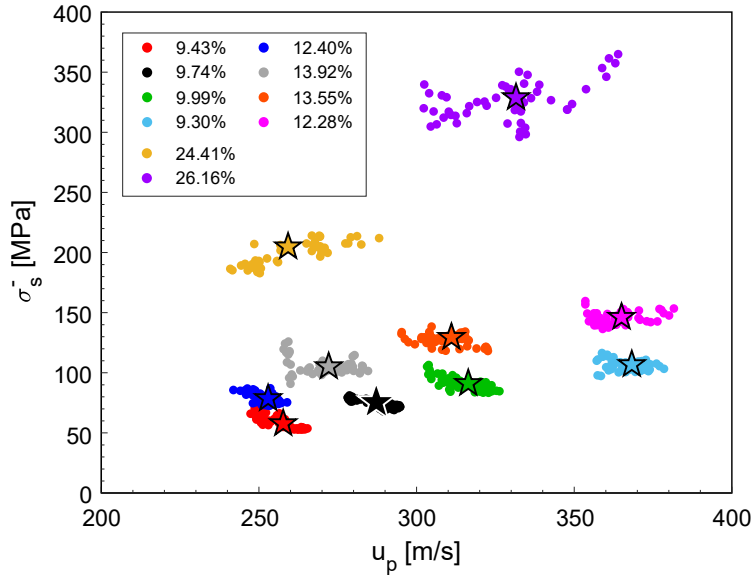
Figure 4.9: Experimental stress, σ_s^-, vs. particle velocity, u_p, Hugoniot relation. Stars represent linearized values by assuming a constant shock velocity.

In addition to the stress, the internal energy behind the shock, $\mathcal{E}^-$, may be computed in a similar way using conservation of energy (Eq. (4.4)):

$$\mathcal{E}^- = \frac{u_s[\![\rho\dot{x}^2]\!] - [\![\rho\dot{x}^3]\!] + 2[\![\sigma\dot{x}]\!] + 2\mathcal{E}^+(\rho^+ u_s - \rho^+\dot{x}^+)}{2\rho^-(u_s - \dot{x}^-)} . \tag{4.9}$$

Elastic values for $\mathcal{E}_{el}^-$ were solved assuming quiescent initial conditions and used to approximate the internal energy ahead of the shock, $\mathcal{E}_s^+$. Specific internal energy is defined per unit mass and was converted to per unit volume by multiplying by the experimental density (ρ^*). Figure 4.10 shows the $\mathcal{E}_s^- - u_p$ Hugoniot relation for all experiments (a) per unit mass and (b) per unit volume.
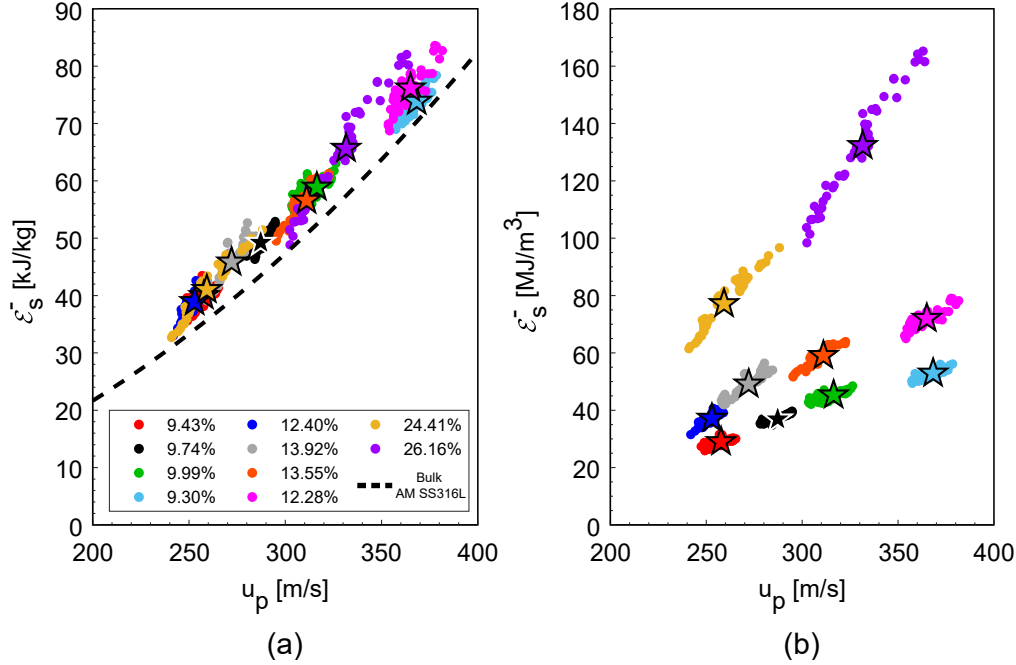
Figure 4.10: Experimental internal energy, $\mathcal{E}_s^-$ vs. particle velocity, u_p, Hugoniot relation normalized per (a) unit mass and (b) unit volume. Stars represent linearized values by assuming a constant shock velocity. The black dashed line shows the specific internal energy for bulk AM SS316L [35].

The specific internal energy converged to a single curve for all particle velocities and relative densities. The dotted black line in Fig. 4.10 represents values for bulk Laser Engineering Net Shaping (LENS) additively manufactured stainless steel 316L from shock experiments [35]. The bulk curve was calculated using measured experimental parameters of LENS AM SS316L: bulk sound speed, $c_0 =$ 4474 m/s, longitudinal sound speed, $c_L =$ 5730 m/s, density, $\rho =$ 7960 kg/m^3, velocity at the Hugoniot Elastic Limit (HEL), $v_{HEL} =$ 60 m/s (approximated from photonic doppler velocimetry wave profiles), and linear coefficient in the $U_s - u_p$ shock relationship, $s =$ 1.54. The stress and specific internal energy ahead of the shock were approximated using the conservation of momentum (Eq. (4.3)) and conservation of energy (Eq. 4.4) and used with a linear $U_s - u_p$ relation for LENS AM SS316L to calculate the specific internal energy behind the shock, $\mathcal{E}_s^-$. The lattice structure curves overall show excellent agreement with the results for the bulk material. Mechanical properties of Selective Laser Melting (SLM) AM SS316L have been shown to vary based upon crystallographic textures [83, 107] and therefore slight deviations between curves may occur due to differences in mechanical properties from differing AM techniques (LENS vs DMLS). Specific internal energy (per unit mass) of lattice specimens is therefore solely dependent

on the parent material properties and particle velocity. Internal energy per unit volume showed a positive correlation with particle velocity and relative density–this is due to an increase of mass in higher relative densities, but little to no change in space-filling volume of the specimens.

4.4 Numerical Simulations

Numerical simulations were used to investigate the validity of the application of shock definitions and parameters and to explore additional trends in lattice structure shock behavior. A finite element framework with the Johnson-Cook constitutive model was used to model the AM SS316L lattice specimens. The elastic, flyer, and shock front locations and speeds were extracted for each unit cell position and Rankine-Hugoniot shock analysis was applied similar to experiments. Simulation results were used to evaluate the effects of exterior node measurements and non-constant impact velocities, and were also compared to experimental values.

4.4.1 Finite Element Model Framework

Numerical simulations were carried out using Abaqus/Explicit (Dassault Systemes, Providence, RI) finite element analysis (FEA) software with 5x5x10 CAD geometries used for AM of specimens. The baseplate of each specimen was fixed to an analytically rigid plate and a second rigid plate was used to impact the lattice with displacement boundary conditions corresponding to experimental flyer displacements. A general contact algorithm was defined for self-contact of the specimen and rigid plate-lattice interactions. Tetrahedral free meshing with quadratic C3D10M elements was used with a local mesh size of 1.5 mm corresponding to 4-5 million nodes and 2-3 million elements. Mass scaling was used to increase the computational timestep to 1 ns which corresponded to $< 0.1\%$ percent change in mass for all specimens. Physical relevance of simulations was evaluated by comparing the total energy to external work, internal energy, kinetic energy, and plastic dissipation at each timestep. Total energy appeared constant with respect to these energies and reached a maximum of 3.5% of the kinetic energy across all simulations, with an average value approximately equal to 0.5%. Figure 4.11(a) shows the side-view of the FEA 3D framework with lattice specimen and rigid plates and Fig. 4.11(b) shows nodes of interest for the numerical analysis.

This framework allowed measurement and analysis of both interior and exterior nodes of the lattice specimen. Exterior nodes provided a direct comparison to experimental measurements while interior nodes provided a more appropriate uniaxial
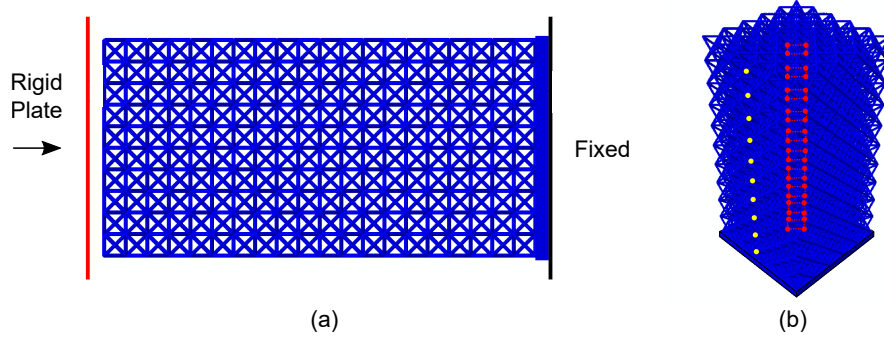
Figure 4.11: Finite element analysis framework: (a) front view of the 3D model of a 5x5x10 UC lattice specimen compressed between one fixed and one moving rigid plate; and (b) interior and exterior nodes of interest.

strain approximation over the innermost unit cells. Displacements and velocities for interior points were taken as the average over four nodes located at the middle vertices of the unit cell. Validation and comparison of these two techniques is discussed in Section 4.4.4.

To model the bulk material, the Johnson-Cook (JC) constitutive model [108] was used for the AM SS316L material:

$$\sigma = [A + B(\epsilon^p)^n] \left[1 + C ln \left(\frac{\dot{\epsilon}^p}{\dot{\epsilon}_0} \right) \right] (1 - \hat{\theta}^m) , \tag{4.10}$$

where ϵ^p is the equivalent plastic strain, $\dot{\epsilon}^p$ is the equivalent plastic strain-rate, and $\dot{\epsilon}_0$ is the reference strain-rate. The non-dimensional temperature, $\hat{\theta}$, is piecewise defined by: $(T - T_{ref})/(T_{melt} - T_{ref})$ for $T_{ref} < T < T_{melt}$; 0 for $T < T_{ref}$; and 1 for $T > T_{melt}$. The melting temperature, T_{melt}, was taken as the melting temperature of conventional SS316L [109] and a high reference temperature, T_{ref}, was chosen to limit temperature effects.

Material parameters for the JC constitutive model are shown in Table 4.4.

Table 4.4: Material parameters used for the Johnson-Cook (JC) constitutive model in numerical simulations. Elastic parameters, physical parameters, and m are taken from typical values for SS316L [109, 110] and the constitutive parameters are taken from experiments on AM SS316L by Platek et al. [111].

$\rho\,[kg/m^3]$	E [GPa]	ν [-]	A [MPa]	B [MPa]	n [-]	C [-]	m [-]	T_{ref} [K]	T_{melt} [K]	$\dot{\epsilon}_0$ [-]
8000	193	0.27	542	303	0.293	0.028	0.6	1573.15	1673.15	0.001

AM techniques of metals induce different material properties due to grain elongation and partial melting [83, 107] and constitutive modeling using conventional SS316L

properties may lead to less accurate results. The parameters for the Johnson-Cook model ($A, B, n, C, \dot{\epsilon}_0$) were taken from experimental data collected by Platek et al. [111] on SLM AM SS316L while elastic parameters, density, and m were were chosen from typical values for conventional SS316L [109, 110].

4.4.2 Simulation Results

Using the defined 3D model, numerical simulations were performed for each corresponding experiment in Table 4.2. Deformation images from simulation results clearly show the two-wave structure seen in experiments. Figure 4.12(a) shows the visualization of the shock front defined by particle velocities for $\rho^*/\rho_s = 15\%$ and $V_{impact} \approx 300$ m/s (corresponding to experiment #$OT15_2$) and full deformation can be visualized in Supplementary Video S3. A clear discontinuity in particle velocity was observed between regions of near zero velocity ahead of the shock and high constant velocity behind the shock.

Figure 4.12(b) shows the particle velocities extracted from the interior nodes shown in Fig. 4.11(b). Particle velocities were extracted from 10 positions along the lattice each corresponding to one unit cell. The shock front was defined using a maximum du_p/dt (change in velocity with respect to time) criterion. This technique was chosen over the maximum du_p/dX technique used in experiments due to the higher temporal resolution (number of frames) than spatial resolution (number of unit cell positions) and therefore provided a more accurate calculation. The elastic wave and velocity ahead of the shock were defined as in experiments: the elastic wave front was defined using a 15 μm displacement criterion and the velocity ahead of the shock was defined from the velocity-time profile as the point of maximum change in curvature before the shock front. Small oscillations of particle velocity behind the shock were observed but clearly follow the deceleration of the flyer.

The computed elastic, flyer, and shock fronts are shown in Fig. 4.12(c) and closely resemble trends from experiments. The position of the propagating elastic wave front appears to be progressing linearly in time and elastic wave speed was extracted by applying a linear fit. Differences between the shock fronts in undeformed and deformed configurations were also observed, but smaller than those in experiments.

Flyer speed was set by experimental displacement boundary conditions and shock velocities were computed using a three-point central difference method and are shown in Fig. 4.12(d). The lower noise in the simulation results revealed trends within the velocities: Eulerian shock velocity decreased with time while Lagrangian

(a)

(b)

(c)

(d)
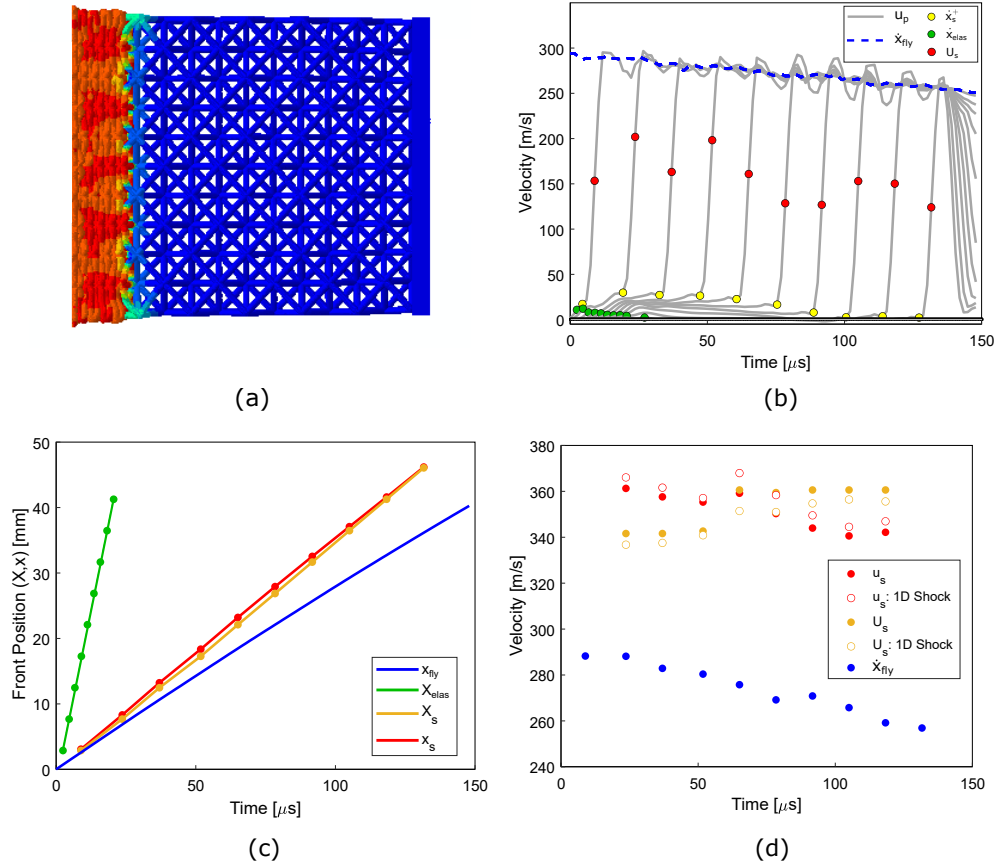
Figure 4.12: Wave definition and extraction in numerical simulation corresponding to experiment #$OT15_2$: (a) deformation images from numerical simulations showed similar shock structure to experimental images; (b) particle velocity profiles for each unit cell position used to determine shock parameters and front locations; (c) elastic (X_{elas}), flyer (x_{fly}), and shock (X_s, x_s) front-time histories; and (d) corresponding shock velocity and flyer speed with 1D shock theory calculations.

shock velocity increased with time. These opposite trends may be explained by considering definitions of the shock velocity in Eulerian and Lagrangian coordinates derived by Davison [65]:

$$U_s = \frac{\rho^+}{\rho_0}(u_s - \dot{x}^+).$$
(4.11)

Equation (4.11) quantifies the effect of the elastic wave and density ahead of the shock on the Lagrangian shock velocity. This relation allows the computation of shock velocity in either coordinate given known values for the density and velocity ahead of the shock. The ratio density ahead of the shock, ρ^+/ρ_0, was again defined as the ratio of distances from the non-compacted lattice face to the shock front: $\rho^+/\rho_0 = (L - t_b - X_s)/(L - t_b - x_s)$. Values of both coordinate shock velocities were computed using u_s, U_s, and Eq. (4.11) and are represented by the open

data points in Fig. 4.12(d). These calculated values confirm the increasing and decreasing trends of U_s and u_s, respectively. Analysis in either coordinate system is valid, but only the deformed coordinate showed a positive correlation with the flyer speed with both decreasing with time. This correlation serves as the justification for defining the $u_s - u_p$ relation in the deformed coordinate for the Rankine-Hugoniot shock analysis.

4.4.3 Rankine-Hugoniot Shock Analysis

The Rankine-Hugoniot shock analysis of numerical simulations is shown in Fig. 4.13. Figure 4.13(a) shows the Eulerian shock velocity, u_s, flyer speed, u_p, relation for $\rho^*/\rho_s = 10\%, 15\%$, and 30%. The linear relation, $u_s = m + Su_p$, found in experiments was more evident in simulation results and illustrated by the fit lines along the individual scatter points. Linearized approximations for each simulation are shown by diamond markers. The slope $S \approx 1$ for all simulations and appeared to slightly increase with relative density while m was similar to experimental values and ranged from 30-100 m/s. Fit parameters are shown in Table 4.5 and are further discussed in Section 4.4.4.

Figure 4.13(b) shows the crush width-time history and the corresponding crushing speeds. Crush width $(x_s(t) - x_{fly}(t))$ profiles appeared linear and speeds were found by applying a linear fit. Crushing speed showed a positive correlation with relative density and a slight dependence on particle velocity with higher crushing speeds occurring at higher impact velocities. The $u_s - u_p$ relation was again approximated with $S = 1$ and m as the crushing speed taken as the average for each relative density. Crushing speed $u_s - u_p$ approximations are shown as dotted lines in Fig. 4.13(a) and show good agreement with data.

Rankine-Hugoniot jump conditions were applied for the elastic wave assuming quiescent initial conditions and wave speed, c_{elas}, which was measured using a linear fit of the front positions as seen in Fig. 4.12(c). The velocity behind the elastic wave, $\dot{x}_{el}^-$, was taken as the maximum velocity value of the elastic wave and the stress behind the elastic wave, σ_{el}^- was approximated using Eq. (4.8). Each data point represents results from one unit cell position (taken over four interior nodes about the central UC) and used to calculate the Hugoniot response, similar to full-field measurements of experiments. The density behind the shock, ρ_s^-, was calculated using Eq. (4.7) and the stress behind the shock, σ_s^-, was evaluated using Eq. (4.8). Additionally, the stress ahead of the shock is approximated as $\sigma_s^+ = \sigma_{el}^-$ as
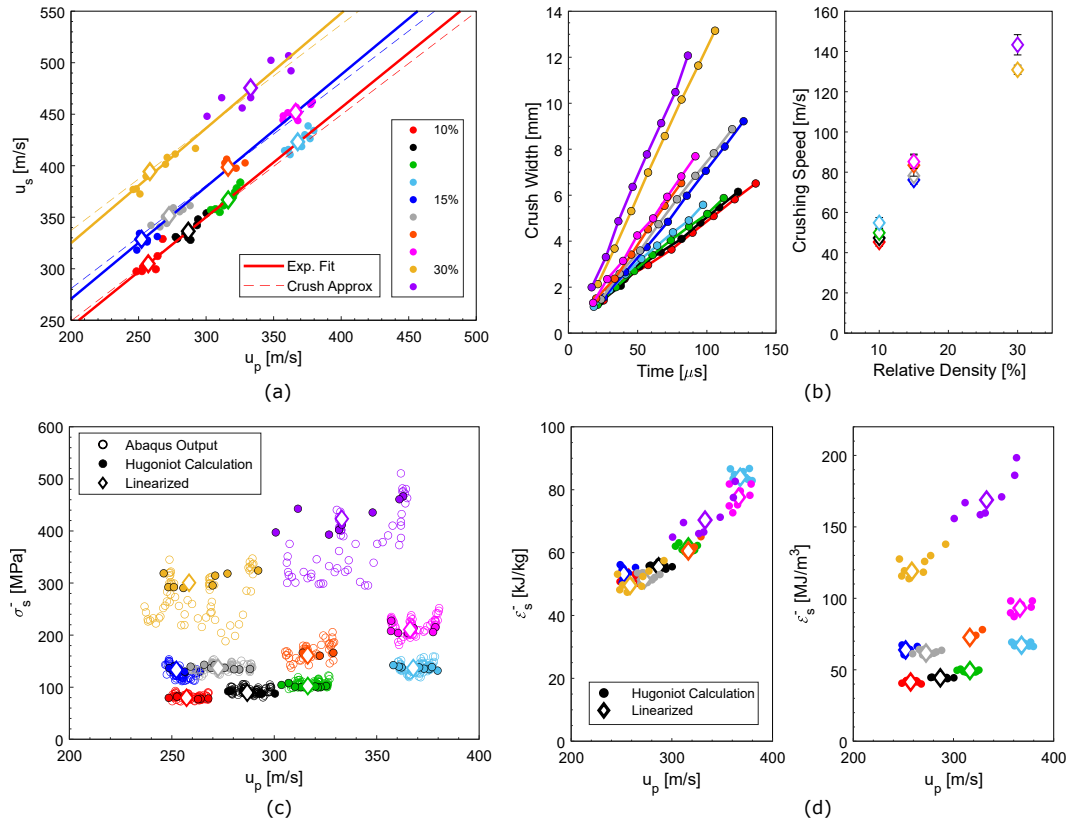
Figure 4.13: Shock Hugoniot relations for numerical simulations: (a) shock velocity (u_s) − particle velocity (u_p) relation, (b) crushing width-time history and crushing speed versus relative density, (c) stress behind the shock (σ_s^-) − particle velocity (u_p) relation, and (d) internal energy behind the shock ($\mathcal{E}_s^-$) − particle velocity (u_s) relation per unit mass and per unit volume.

done in experiments. It is noted that calculation of ρ^+/ρ_0 and subsequent parameters is improved over the experimental approach due to the true fixed position (no lateral motion) of the baseplate.

Reaction force measurements on the rigid impactor plate were extracted and directly compared to calculated Hugoniot values. Figure 4.13(c) shows the $\sigma_s^- - u_p$ relation with the rigid impactor reaction force outputs, Hugoniot calculations, and linearized approximations. Excellent agreement between Hugoniot calculations and reaction force outputs validates application of one-dimensional Rankine-Hugoniot shock analysis.

Figure 4.13(d) shows the internal energy ($\mathcal{E}_s^-$) − particle velocity (u_p) relation calculated using Eq. (4.9) and approximation of the state ahead of the shock as $\mathcal{E}_s^+ = \mathcal{E}_{el}^-$. Convergence of curves for internal energy per unit mass and divergence of curves for internal energy per unit volume was observed as in experiments.

4.4.4 Validation of Node Measurements

Exterior node measurements on the three-dimensional lattice structure may not match internal node measurements due to lateral movement of exterior material during loading. This difference in values is examined through the $u_s - u_p$ relations for these nodes. Figure 4.14(a) shows the numerical $u_s - u_p$ relation for exterior and interior nodes (shown in Fig. 4.11(b)) for $\rho^*/\rho_s = 10\%$ specimens with experimental displacements as applied boundary conditions. Exterior nodes showed a lower intercept than interior nodes which may be interpreted as a lower crushing speed. This decrease in crushing speed measured in the axial direction is consistent with the presence of lateral velocities. Overall, differences between shock velocities were small and exterior node measurements adequately approximate interior measurements. $S \approx 1$ with exterior and interior values differing around 2%. While m values varied more, the corresponding shock velocities showed 4-6% difference within relevant particle velocity ranges.
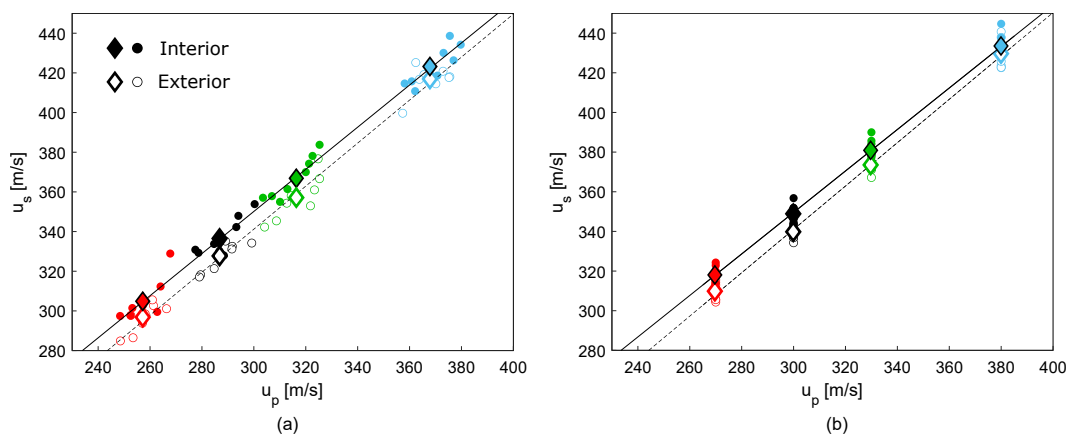
Figure 4.14: Comparison of shock velocity (u_s) – particle velocity (u_p) relation for interior and exterior nodes for applied boundary conditions of (a) experimental displacements and (b) constant impact velocities for $\rho^*/\rho_s = 10\%$ specimens. The circles ($\circ$) correspond to the various nodal values and the diamonds ($\diamond$) correspond to linearized values by assuming a constant shock velocity.

Figure 4.14(b) show the $u_s - u_p$ relation for exterior and interior nodes of $\rho^*/\rho_s = 10\%$ specimens impacted at constant velocities of 270, 300, 330, and 380 m/s. Exterior nodes again showed a lower intercept than interior nodes consistent with a lower axial-measured crushing speed due to lateral velocities. Scatter of $4 - 5\%$ was observed in shock velocities and can be attributed to measurement techniques and resolution. Excellent agreement between linear $u_s - u_p$ relations and linearized shock velocity approximations justify the linearized approximations as relevant quantities.

Table 4.5: The linear shock velocity (u_s) – particle velocity (u_p) parameters (S, m_{fit}, m_{crush}) for exterior and interior nodes of experiments and simulations with applied experimental displacements (δ_{exp}) for $\rho^*/\rho_s = 10\%, 15\%$, and 30% specimens and constant impact velocities (u_{const}) for $\rho^*/\rho_s = 10\%$ specimens.

ρ^*/ρ_s [%]		Node	Loading	S	m_{fit}	m_{crush}
10	Simulation	Exterior	u_{const}	1.094 ± 0.045	12.95 ± 14.47	44.47 ± 2.33
10	Simulation	Interior	u_{const}	1.047 ± 0.044	35.68 ± 14.04	49.41 ± 1.11
10	Experiment	Exterior	-	0.978 ± 0.041	37.98 ± 12.71	30.93 ± 2.23
10	Simulation	Exterior	δ_{exp}	1.085 ± 0.050	15.88 ± 15.39	43.56 ± 2.60
10	Simulation	Interior	δ_{exp}	1.063 ± 0.045	31.54 ± 13.83	49.34 ± 2.06
12	Experiment	Exterior	-	0.929 ± 0.030	59.09 ± 9.52	36.32 ± 4.41
13	Experiment	Exterior	-	0.973 ± 0.105	58.99 ± 30.43	52.10 ± 4.22
15	Simulation	Interior	δ_{exp}	1.089 ± 0.051	53.02 ± 15.30	80.79 ± 2.15
25	Experiment	Exterior	-	1.014 ± 0.096	99.15 ± 28.37	104.89 ± 3.09
30	Simulation	Interior	δ_{exp}	1.115 ± 0.123	101.8 ± 37.07	137.12 ± 6.21

Table 4.5 shows computed values for S, m_{fit}, and m_{crush} where S and m_{fit} were found using a linear fit of all data points and m_{crush} was computed as the average crushing speed. Errors for S and m_{fit} were found using 95% confidence bounds and error for m_{crush} was calculated as the standard error. These results provide insights into the sensitivity of the $u_s - u_p$ calculations. $S \approx 1$ within error for all conditions while m_{fit} and m_{crush} varied with significant errors. The difference in fit values between experimental displacements and constant velocities was small (1-2% for S, 10-20% for m_{fit}, and 2% for m_{crush}) and verifies the use of experimental displacements for $u_s - u_p$ relations. Crushing speed was higher in simulations than experiments for all relative densities which may be attributed to perfect geometries and higher relative densities in simulations.

4.4.5 Comparison to Experiments

Numerical simulation results support the Hugoniot equation of state (EOS) in the form of a linear $u_s - u_p$ relation as a reasonable approximation of the shock response of SS316L octet-truss lattices. The linearized results for all experiments and simulations are shown in Fig. 4.15.

Differences between experiment and simulation may be attributed to the constitutive model, additive manufacturing technique [83, 107], stiffness effects from geometric imperfections [73], and lower relative densities from manufacturing defects. Similar trends were observed in both experiment and simulation: a linear $u_s - u_p$ relation (Fig. 4.15(a)); linear crushing width-time histories and positive correlation between crushing speed and relative density (Fig. 4.15(b)); increasing stress behind the shock with particle velocity and relative density (Fig. 4.15(c)); and converged

internal energy per unit mass behind the shock and diverged internal energy per unit volume behind the shock (Fig. 4.15(d)). Higher values were observed for all quantities in simulations which may be dependent on geometric defects and distributions [58].
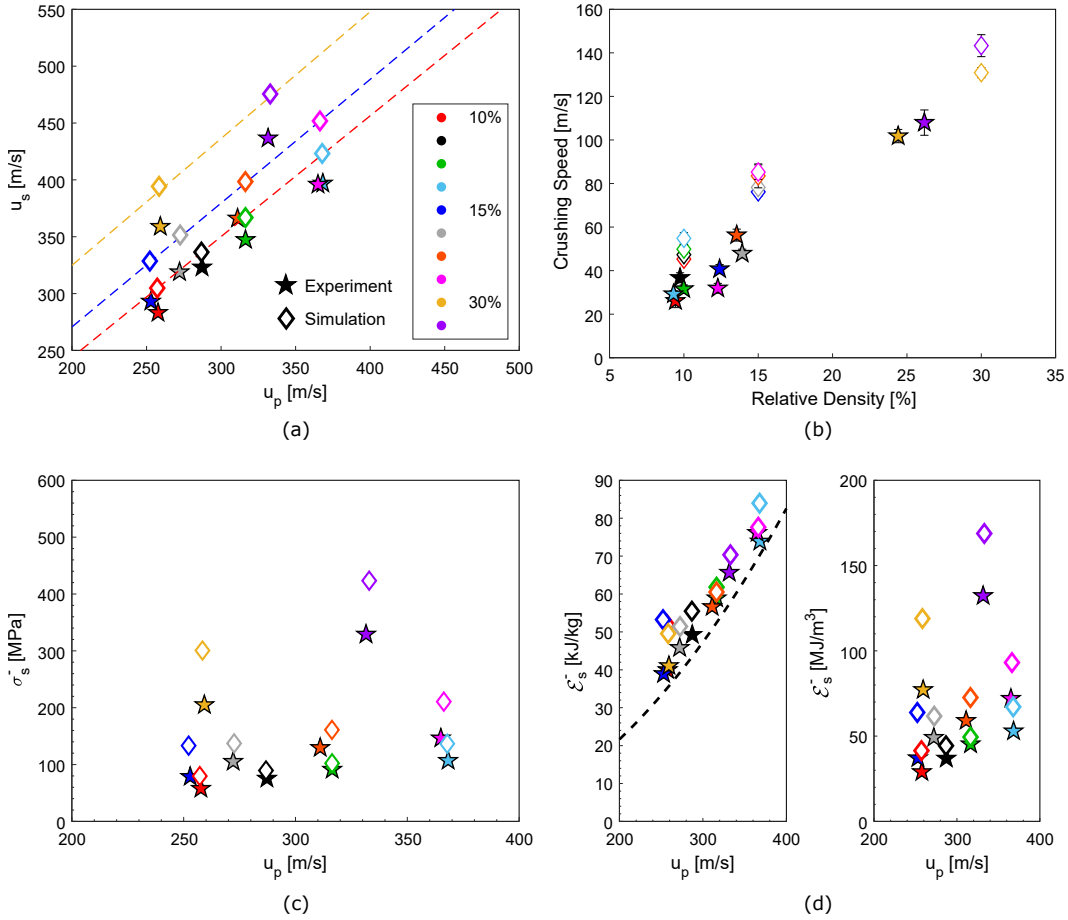
Figure 4.15: Comparison between simulation and experiment for (a) shock velocity (u_s) − particle velocity (u_p) relation with simulation fit lines, (b) crushing speed − relative density relation, (c) stress (σ_s^-) − particle velocity (u_p) relation, and (d) internal energy ($\mathcal{E}_s^-$) − particle velocity (u_p) relation defined per unit mass and per unit volume. The dotted black line represents experimental values for bulk AM SS316L [35].

Average elastic wave speeds are compared for all relative densities and reported in Table 4.6. Infinite lattice approximations were found using effective elastic properties from Bloch-wave homogenization of the octet-truss unit cell calculated by Patil and Matlack [112]. Normalized effective uniaxial modulus was found as a function of relative density with scaling $E^*/E_s \propto (\rho^*/\rho_s)^{1.2}$ and values were extracted for $\rho^*/\rho_s = 10\%, 15\%, 30\%$. Wave speed was approximated as $c = \sqrt{E^*/\rho^*}$ using these values. Experiment and simulation values were calculated using linear fits of front profiles as previously discussed.

In experiment, simulation, and Bloch-wave analysis, elastic wave speed increased with relative density. Wave speeds were lower in experiments and showed better agreement with both simulation and Bloch-wave values at higher relative densities. Bloch-wave approximations of wave speeds showed excellent agreement with simulation values with 1% difference at $\rho^*/\rho_s = 10\%$ and 15%, and 6% difference at $\rho^*/\rho_s = 30\%$. Experimental wave speed at $\rho^*/\rho_s = 10\%$ showed 18.6% difference from simulation values, $\rho^*/\rho_s = 15\%$ showed 10.1% difference, and $\rho^*/\rho_s = 30\%$ showed 4.9% difference.

Table 4.6: Average elastic wave speeds from experiments and simulations for $\rho^*/\rho_s = 10\%, 15\%$, and 30% specimens. Error was calculated as the standard error of the measurements. Bloch-wave approximations of wave speeds were found using effective stiffness calculations [112].

ρ^*/ρ_s	10%	15%	30%
Experiment	1709 ± 54	1934 ± 26	2322 ± 11.18
Simulation	2028 ± 5	2129 ± 10	2438 ± 6
Bloch-wave	2009	2142	2299

A major reason for this discrepancy in values could be manufacturing defects. Manufacturing defects were observed frequently in the horizontal struts of lower density specimens as seen in Fig. 4.16.
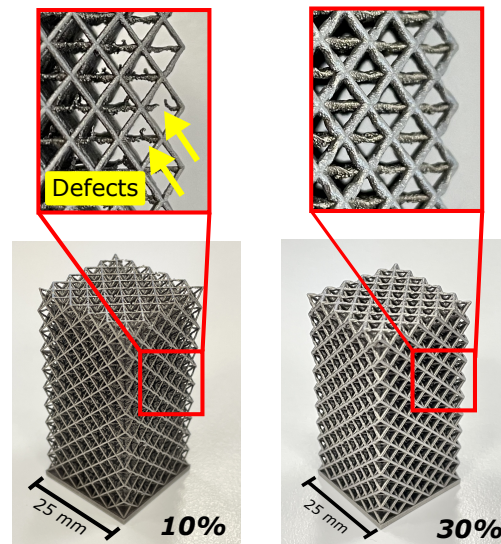
Figure 4.16: Manufacturing defects of $\rho^*/\rho_s = 10\%$ specimens present on horizontal struts relative to print direction.

High quantities of manufacturing imperfections in $\rho^*/\rho_s = 10\%$ experimental specimens suggest a loss of stiffness from geometric defects and support a larger observed

difference in speeds. These defects may be attributed to the manufacturing limits of DMLS technology for features at this length scale such as poor heat conduction due to small feature dimensions or powder bed rollers disrupting weakened struts during printing. The effects of geometric defects are accounted for in the shock analysis by using the experimental elastic wave speed and relative density values.

4.5   Summary and Conclusions

The shock compression behavior of stainless steel 316L octet-truss lattice structures was explored and shock definitions and Rankine-Hugoniot shock theory were applied to both experiments and simulations. SS316L octet-truss lattice structures with 5x5x10 unit cell (5 mm/UC) geometries were additively manufactured using DMLS. Normal plate impact experiments were conducted on specimens with nominal relative densities (volume fraction) of 10%, 15%, and 30% at impact velocities ranging from 270 m/s to 390 m/s. High-speed experimental images were taken at 500,000 – 800,000 fps and digital image correlation (DIC) was performed on the lattice specimen and flyer to extract full-field particle velocities. Images showed a distinct discontinuity between regions of highly densified and intact material with a densification front propagating in the direction of impact. Particle velocities of the densified material were approximately equal to the flyer speed while the velocities of the intact region were near zero. A two-wave structure consisting of an elastic wave and compaction shock wave was observed in agreement with prior work [56, 57]. The elastic wave was defined using a displacement criterion and elastic wave speeds appear constant for all specimens at a given relative density. Experimental and simulation elastic wave speeds were found to be around 30%-50% of the bulk sound speed of the parent material.

The observed 'structural shock' can be modelled using Rankine-Hugoniot jump conditions for one-dimensional planar shocks. The shock front was defined for each material point at the point of maximum change of particle velocity and described through position and time using full-field measurements of the lattice specimen. Full-field measurements allow determination of density and velocity field variables during shock propagation and permit application of the Rankine-Hugoniot jump conditions in the Eulerian form. The elastic wave was treated as a weak shock and jump conditions were used to approximate field variables of the material behind the elastic wave, but ahead of the shock. Stress and internal energy behind the shock were also estimated using the jump conditions and the experimental measurements.

In addition to experiments, numerical simulations using finite element analysis (Abaqus/Explicit) with the Johnson-Cook constitutive model also exhibit a highly densified region with a steady front separated from the intact material. Numerical results validate experimental techniques by verifying the negligible effects of exterior node measurements and non-constant impact velocities, matching calculated Hugoniot stress values to numerical outputs, and accurately computing shock velocities using 1D shock theory. Rankine-Hugoniot analysis of numerical simulations matches experimental results leading to the following conclusions:

- A linear shock velocity, u_s, particle velocity, u_p, relation was found to describe the equation of state for octet-truss lattice materials: $u_s = m + S u_p$. Linearized approximations of velocities were found by taking a linear fit of the front position-time history and show excellent agreement with fits of the full data.

- A slope of $S \approx 1$ was found in both experiment and simulation and suggests modeling lattice structures as elastic-plastic rigid-locking [64] crushable materials.

- The constant term, m, is correlated with the crushing front speed with values $O(10 - 100)$ m/s significantly lower than the elastic wave speeds of SS316L lattices with values $O(2000)$ m/s.

- Stress behind the shock showed a positive correlation with relative density and particle velocity, while specific internal energy calculations showed a correlation only with particle velocity.

- Specific internal energy of lattice specimens closely resembled values obtained from bulk AM SS316L at similar particle velocities.

- 1D shock theory may be applied to numerical simulation results without resorting to a $U_s - u_p$ relation for the bulk material. Qualitative agreement with experimental results shows the shock behavior of lattice structures is dependent on the structural response.

In both experiments and numerical simulations, consistent definitions for shock parameters such as front locations and field variables (density, particle velocity) behind and ahead of the shock have been developed, and 1D Rankine-Hugoniot analysis may be identically applied. With these definitions and theoretical framework, future work entails the exploration of shock behavior of lattice structures with varying

topology and parent material. Homogenization and extrapolation of shock behavior based on relative density and unit cell topology would allow for optimization of these materials at a highly decreased computational cost. Extension to other topologies would allow engineering design of impact-dissipative structures for applications of energy absorption, and strong lightweight materials for dynamic applications.

Chapter 5

SUMMARY AND FUTURE WORK

5.1   Summary

In this thesis, we investigated the dynamic behavior of polymeric and metallic lattice structures of varying topology and relative density on the centimeter length scale. The mechanical response of these materials depends on topology, strain-rate, and base material, and demonstrates various regimes of deformation based upon strain-rate loading conditions. Experimental techniques are used to study the *high strain-rate*, *transient dynamic*, and *shock compression* behavior of lattice structures and numerical simulations are used to support, verify, and extend the experimental analyses.

In Chapter 2, the *high strain-rate* response ($\dot{\epsilon} \approx 1000s^{-1}$) of rod-like and plate-like polymeric lattice structures with Kelvin unit cells of varying relative density is explored. Distinct effects of rod and plate structural components are demonstrated by mechanical behavior dependent on strain-rate, relative density, and topology despite a similar unit cell shape. The *high strain-rate* deformation regime is characterized through strain-rate effects and deformation modes; strain-rate effects in lattice specimens are similar to those observed in the base material, and deformation bands form in the middle of specimens at both high and low strain-rates which more strongly localize at low strain-rates and low relative densities. Engineering design implications of rod versus plate structures are evaluated through mechanical failure properties: plate-like lattices demonstrate superior properties at lower relative densities and rod-like lattices demonstrate superior properties at higher relative densities. The scaling of these properties with relative density is also calculated. Explicit finite element numerical simulations are used to validate deformation modes and scaling/property trends and relate those observed in experiments.

In Chapter 3, the *transient dynamic* and transition to shock response of polymeric lattice structures with cubic, Kelvin, and octet-truss topologies at moderate to high impact velocities (25-70 m/s) is discussed. Distinct mechanical behavior is again observed across different topologies, but a new deformation regime persists due to higher strain-rate loading. The *transient dynamic* regime ($\dot{\epsilon} \approx 500s^{-1}$) is characterized by initiation of a compaction wave at the impact surface and additional

deformation bands with modes similar to low strain-rate modes of deformation. Low strain-rate mechanical properties, elastic wave speeds, deformation modes, particle velocities, and distal stress histories are analyzed for each topology to characterize lattice structure behavior. At high impact velocities (> 50 m/s), a sole compaction wave is observed which characterizes the *shock compression* response ($\dot{\epsilon} \approx 1200 s^{-1}$). This compaction wave is modeled as a 'shock' and one-dimensional continuum shock theory is used with full-field measurements to quantify a non-steady shock response and extract the stress behind the compaction wave. We demonstrate that there is shock-induced stress enhancement at the impact surface which is dependent on impact velocity, topology and dynamic material effects.

Finally, in Chapter 4 we explore the *shock compression* behavior ($\dot{\epsilon} \approx 6500 s^{-1}$) of metallic octet-truss lattice structures at higher impact velocities (> 250 m/s). We demonstrate these lattice structures support an elastic and compaction shock wave similar to polymeric lattice structures in Chapter 3, which supports this behavior as a generalization. Rankine-Hugoniot 1D shock analysis is carried out using full-field experimental measurements and validated using identical techniques on numerical simulations. A linear shock velocity (u_s) – particle velocity (u_p) relation for the equation of state (EOS) is approximated using a slope of one and constant term equal to the linearized crushing speed which exhibits positive correlation with relative density. Shock analysis reveals the stress behind the shock depends on particle velocity and relative density while the specific internal energy behind the shock depends only on particle velocity. Specific internal energy calculations for lattice structures agree with approximations for the base material which has engineering design implications that structure has limited effect on this quantity for lattice structures under shock loading. Notably, one-dimensional continuum shock theory is applied to numerical simulations using a Johnson-Cook strength-hardening model without resorting to a $u_s - u_p$ relation for the base material, which characterizes this deformation regime and compaction wave as a 'structural shock.'

5.2 Future Work

The field of architected materials will continue to grow as computational design methods advance and additive manufacturing (AM) techniques improve and become more accessible. The scope of this thesis covers experimental investigations on lattice structures across varying strain-rates, but there remains a large research avenue for future work in this field. The following sections outline particularly interesting and attainable opportunities for further research.

5.2.1 Experiments on Shock Compression

Plate and Sheet Lattice Structures

Shock compression behavior of cellular materials such as stochastic foams has been well-studied [52, 54, 55, 62–64, 101, 103] and now recently investigated in rod-based lattice architectures. Plate-lattices and sheet-lattices have been realized to show superior mechanical properties to rod-based counterparts, but shock compression behavior of these materials remains unstudied. It may be expected that at comparable relative densities these lattices will show a structural shock response while offering benefits of superior mechanical properties for dynamic applications. However, manufacturability of closed-cell structures such as plate-lattices remains a difficult challenge due to trapping of powder or liquid photoresin inside unit cells. Advancement of AM technology that allows for realization of these structures would enable increased experimental work on these materials and confirmation of these deformation regimes. Improvements in experimental techniques of visible and x-ray high-speed imaging and full-field measurement methods such as digital image correlation will also permit observation of these phenomena at higher strain-rates with increased resolution, allowing a closer inspection of the complex mechanics and mechanisms at play.

Impact at Very High Velocities

At very high impact velocities (> 500 m/s), phenomena such as jetting [104, 113] and ejecta [58] occur in periodic and lattice materials. Further work on shock compression of lattice structures at these velocities would allow for exploration of a potential deformation regime which surpasses the regime of 'structural shock' in which the base material itself undergoes a change in density. This regime may be relevant for high-velocity impact experienced by spacecrafts or structures. These effects are not considered in this thesis, exemplified through numerical modeling in Chapter 4 with elastic parameters and a Johnson-Cook strength model which implies constant density in the strut material. Other shock regimes such as over-driven shocks which exhibit velocities faster than the elastic wave are also currently unexplored and remain an area for future work on architected materials.

Determination of Equation of State

Conventional shock physics revolves around the determination of an equation of state (EOS) of materials found through a shock velocity (U_s) – particle velocity (u_p) relation. This type of relation is discussed in Chapter 4, but further research needs to be conducted to identify these relations for lattices of different topology, base material, relative density, and length scales. While it appears relative density is the

dominant factor for structural shock behavior, it remains to be seen experimentally in various topologies and base materials under steady shock conditions. These relations may also change as deformation regime potentially transitions from 'structural shock' in the architected material to 'true' shock in the base material, resulting in multiple EOS for architected materials dependent on loading rate.

5.2.2 Theory and Analysis

Deformation regimes of lattice structures investigated in this work have an inherent dependence on base material, topology, and relative density. Particularly, *high strain-rate* behavior shows a large dependence on base material, and *shock compression* behavior shows a large dependence on relative density. With understanding of these deformation regimes, it is feasible to construct theory and analysis connecting the behavior of lattice structures across strain-rates. Future work may entail development of analysis for a given unit cell and base material that would allow approximation of the lattice response across all strain-rate deformation regimes. Transition between a low strain-rate and high strain-rate regime may be derived from base material strain-rate dependent constitutive behavior and transition to the shock regime (shock initiation) may be predicted using relative density and topology. While there has been work studying shock initiation in cellular materials such as stochastic foams [51, 64], it has yet to be readily applied to lattice structures.

5.2.3 Computational Methods and Homogenization

The advancement of computational design has spurred the field of architected materials and continues to allow exploration of topology effects. Unit cell design in this thesis uses previously designed structures but may be improved further with techniques such as topology optimization [44] and machine learning [114, 115].

Computational techniques also allow for realization of unit cell designs of varying density (graded structures), varying size (hierarchical structures), or combination of topologies. While heterogeneous design is feasible, there is benefit in considering lattice structures at the unit cell level as a representative volume element (RVE). Computational design and simulation of lattice structures is expensive due to complex geometries, and while improvements in computation will advance these abilities, modeling and analysis of a single unit cell remains at an incredibly inexpensive cost. Homogenization of the unit cell response, especially in the dynamic regime, would allow for design of complex lattice structures and understanding of macroscopic mechanical response at a low computational cost, cutting down design time and increasing engineering efficiency.

5.2.4 Thermomechanical Effects in Modeling

Plastic work and dissipation occur during deformation of lattice structures, particularly with metallic base materials, which is supported through numerical simulation results in Chapter 4. The thermomechanical conversion of plastic work to heat may induce behaviors such as thermal softening in the base material, however, these effects are not considered during modeling in this thesis. A high reference (onset of effects) temperature was used in Section 4.4.1 for the definition of the Johnson-Cook (JC) constitutive model of AM SS316L to prevent the onset of thermal effects. Thermomechanical effects in lattice structures remains an area of future work and may be explored through varying this reference temperature in the JC model parameters or with other temperature-dependent constitutive relations.

5.2.5 Unit Cell Size Effects

Size effects have been well-studied in cellular materials through 2D modeling of foams [116] and lattice structures [117] which have shown the number of unit cells in a given material volume affects the quasi-static mechanical response. These effects have been extended to dynamic deformations experimentally demonstrated by Xiao et al. [43] in titanium alloy 3D lattices with distinct high strain-rate behaviors of 3x3x3 5mm UC and 5x5x5 3mm UC specimens. Size effects may be expected for lattice structures in this thesis in the "quasi-static" and "high strain-rate" deformation regimes. However, size effects are not expected to play a large role in the "shock compression" regime as the deformation is dominated by the volume fraction of the specimens and compaction to a locking strain for each unit cell. A more complete analysis of size effects in lattice structures across the various dynamic deformation regimes remains an area for future work in this field.

In this thesis, lattice specimen geometries were selected as 5x5x5 (or 5x5x10) UC based upon manufacturing resolutions and dimensions of experimental apparatus. A 5x5 row geometry allowed for a well-constrained middle section of test specimens with two unit cells on each side. Changing strut dimensions of lattice structures would allow an increased or decreased number of unit cells for a given build volume and may induce size effects. However, a trade-off exists due to current manufacturing resolutions where defects present in the specimens will dominate the behavior at very low strut thicknesses.

BIBLIOGRAPHY

[1]   Lorna J. Gibson and Michael F. Ashby. *Cellular Solids*. Cambridge University Press, 1997. ISBN: 9780521499118. DOI: 10.1017/CBO9781139878326.

[2]   Lorna J. Gibson, Michael F. Ashby, and Brendan A. Harley. *Cellular materials in nature and medicine*. Cambridge University Press, 2010. ISBN: 9780521195447.

[3]   Michael F. Ashby et al. "Chapter 4 – Properties of metal foams." *Metal Foams*. Butterworth-Heinemann, 2000, pp. 40–54. ISBN: 978-0-7506-7219-1. DOI: 10.1016/B978-075067219-1/50006-4.

[4]   Michael F. Ashby. "The properties of foams and lattices." *Philosophical Transactions of the Royal Society A: Mathematical, Physical and Engineering Sciences* 364.1838 (2006), pp. 15–30. ISSN: 1364503X. DOI: 10.1098/rsta.2005.1678.

[5]   John Banhart. "Manufacture, characterisation and application of cellular metals and metal foams." *Progress in Materials Science* 46.6 (2001), pp. 559–632. ISSN: 00796425. DOI: 10.1016/S0079-6425(00)00002-5.

[6]   Antonio Fuganti et al. "Aluminum foam for automotive applications." *Advanced Engineering Materials* 2.4 (2000), pp. 200–204. ISSN: 1438-1656. DOI: 10.1002/(sici)1527-2648(200004)2:4<200::aid-adem200>3.0.co;2-2.

[7]   Carolyn C. Seepersad et al. "Multifunctional design of prismatic cellular materials." *Journal of Computer-Aided Materials Design* 11.2-3 (2005), pp. 163–181. ISSN: 09281045. DOI: 10.1007/s10820-005-3167-0.

[8]   Amir A. Zadpoor. "Mechanical performance of additively manufactured meta-biomaterials." *Acta Biomaterialia* 85 (2019), pp. 41–59. ISSN: 18787568. DOI: 10.1016/j.actbio.2018.12.038.

[9]   Tobias A. Schaedler and William B. Carter. "Architected cellular materials." *Annual Review of Materials Research* 46 (2016), pp. 187–210. ISSN: 15317331. DOI: 10.1146/annurev-matsci-070115-031624.

[10]   Matteo Benedetti et al. "Architected cellular materials: A review on their mechanical properties towards fatigue-tolerant design and fabrication." *Materials Science and Engineering: R: Reports* 144 (2021), p. 100606. ISSN: 0927-796X. DOI: 10.1016/j.mser.2021.100606.

[11]   Syed A.M. Tofail et al. "Additive manufacturing: Scientific and technological challenges, market uptake and opportunities." *Materials Today* 21.1 (2018), pp. 22–37. ISSN: 18734103. DOI: 10.1016/j.mattod.2017.07.001.

[12]   Mark Helou and Sami Kara. "Design, analysis and manufacturing of lattice structures: An overview." *International Journal of Computer Integrated Manufacturing* 31.3 (2018), pp. 243–261. ISSN: 13623052. DOI: 10.1080/0951192X.2017.1407456.

[13]   Norman A. Fleck, Vikram S. Deshpande, and Michael F. Ashby. "Micro-architectured materials: Past, present and future." *Proceedings of the Royal Society A: Mathematical, Physical and Engineering Sciences* 466.2121 (2010), pp. 2495–2516. ISSN: 14712946. DOI: 10.1098/rspa.2010.0215.

[14]   Xuan Zhang et al. "Design, fabrication, and mechanics of 3D micro-/nanolattices." *Small* 16.15 (2020), pp. 1–19. ISSN: 16136829. DOI: 10.1002/smll.201902842.

[15]   Ruth Schwaiger, Lucas R. Meza, and Xiaoyan Li. "The extreme mechanics of micro- and nanoarchitected materials." *MRS Bulletin* 44.10 (2019), pp. 758–765. ISSN: 08837694. DOI: 10.1557/mrs.2019.230.

[16]   Vikram S. Deshpande, Michael F. Ashby, and Norman A. Fleck. "Foam topology: Bending versus stretching dominated architectures." *Acta Materialia* 49.6 (2001), pp. 1035–1040. ISSN: 00207462. DOI: 10.1016/S1359-6454(00)00379-7.

[17]   Marc A. Meyers. *Dynamic Behavior of Materials*. John Wiley and Sons, Ltd, 1994, pp. 98–123. ISBN: 9780470172278. DOI: 10.1002/9780470172278.

[18]   Yongle Sun and Qingming Li. "Dynamic compressive behaviour of cellular materials: A review of phenomenon, mechanism and modelling." *International Journal of Impact Engineering* 112 (2018), pp. 74–115. ISSN: 0734743X. DOI: 10.1016/j.ijimpeng.2017.10.006.

[19]   James Clerk Maxwell. "L. on the calculation of the equilibrium and stiffness of frames." *The London, Edinburgh, and Dublin Philosophical Magazine and Journal of Science* 27.182 (1864), pp. 294–299. DOI: 10.1080/14786446408643668.

[20]   Christopher R. Calladine. "Buckminster Fuller's "tensegrity" structures and Clerk Maxwell's rules for the construction of stiff frames." *International journal of solids and structures* 14.2 (1978), pp. 161–172. DOI: 10.1016/0020-7683(78)90052-5.

[21]   Oraib Al-Ketan, Reza Rowshan, and Rashid K. Abu Al-Rub. "Topology-mechanical property relationship of 3D printed strut, skeletal, and sheet based periodic metallic cellular materials." *Additive Manufacturing* 19 (2018), pp. 167–183. ISSN: 22148604. DOI: 10.1016/j.addma.2017.12.006.

[22]   Thomas Tancogne-Dejean et al. "3D plate-lattices: An emerging class of low-density metamaterial exhibiting optimal isotropic stiffness." *Advanced Materials* 30.45 (2018), pp. 1–6. ISSN: 15214095. DOI: 10.1002/adma.201803334.

[23] Thomas Tancogne-Dejean et al. "High strain rate response of additively-manufactured plate-lattices: Experiments and modeling." *Journal of Dynamic Behavior of Materials* 5.3 (2019), pp. 361–375. ISSN: 21997454. DOI: 10.1007/s40870-019-00219-6.

[24] Shengyu Duan, Weibin Wen, and Daining Fang. "Additively-manufactured anisotropic and isotropic 3D plate-lattice materials for enhanced mechanical performance: Simulations & experiments." *Acta Materialia* 199 (2020), pp. 397–412. ISSN: 13596454. DOI: 10.1016/j.actamat.2020.08.063.

[25] Colin Bonatti and Dirk Mohr. "Mechanical performance of additively-manufactured anisotropic and isotropic smooth shell-lattice materials: Simulations & experiments." *Journal of the Mechanics and Physics of Solids* 122 (2019), pp. 1–26. ISSN: 00225096. DOI: 10.1016/j.jmps.2018.08.022.

[26] Jonathan B. Berger, Haydn N. G. Wadley, and Robert M. Mcmeeking. "Mechanical metamaterials at the theoretical limit of isotropic elastic stiffness." *Nature Publishing Group* 543.7646 (2017), pp. 533–537. ISSN: 0028-0836. DOI: 10.1038/nature21075.

[27] Zvi Hashin and Shmuel Shtrikman. "A variational approach to the theory of the elastic behaviour of multiphase materials." *Journal of the Mechanics and Physics of Solids* 11.2 (1963), pp. 127–140. ISSN: 00225096. DOI: 10.1016/0022-5096(63)90060-7.

[28] Cameron Crook et al. "Plate-nanolattices at the theoretical limit of stiffness and strength." *Nature Communications* 11.1 (2020), pp. 1–11. ISSN: 20411723. DOI: 10.1038/s41467-020-15434-2.

[29] Colin Bonatti and Dirk Mohr. "Large deformation response of additively-manufactured FCC metamaterials: From octet truss lattices towards continuous shell mesostructures." *International Journal of Plasticity* 92 (2017), pp. 122–147. ISSN: 07496419. DOI: 10.1016/j.ijplas.2017.02.003.

[30] Ian Gibson et al. *Additive manufacturing technologies*. Vol. 17. Springer, 2021. ISBN: 978-1-4939-2113-3. DOI: 10.1007/978-3-030-56127-7.

[31] Xiaoqin Zhou, Yihong Hou, and Jieqiong Lin. "A review on the processing accuracy of two-photon polymerization." *AIP Advances* 5.3 (2015). ISSN: 21583226. DOI: 10.1063/1.4916886.

[32] Marek Pagac et al. "A review of vat photopolymerization technology: Materials, applications, challenges, and future trends of 3d printing." *Polymers* 13.4 (2021), pp. 1–20. ISSN: 20734360. DOI: 10.3390/polym13040598.

[33] Wayne E. King et al. "Laser powder bed fusion additive manufacturing of metals; physics, computational, and materials challenges." *Applied Physics Reviews* 2.4 (2015), p. 041304. DOI: 10.1063/1.4937809.

[34] Benjamin Vayre, Frédéric Vignat, and François Villeneuve. "Metallic additive manufacturing: state-of-the-art review and prospects." *Mechanics & Industry* 13.2 (2012), pp. 89–96. DOI: `10.1051/meca/2012003`.

[35] George T. Gray et al. "Structure/property (constitutive and spallation response) of additively manufactured 316L stainless steel." *Acta Materialia* 138 (2017), pp. 140–149. ISSN: 13596454. DOI: `10.1016/j.actamat.2017.07.045`.

[36] Curt A. Bronkhorst et al. "Structural representation of additively manufactured 316L austenitic stainless steel." *International Journal of Plasticity* 118.January (2019), pp. 70–86. ISSN: 07496419. DOI: `10.1016/j.ijplas.2019.01.012`.

[37] Stefano Natali, Andrea Brotzu, and Daniela Pilone. "Comparison between mechanical properties and structures of a rolled and a 3D-printed stainless steel." *Materials* 12.23 (2019), p. 3867. ISSN: 1996-1944. DOI: `10.3390/ma12233867`.

[38] Stephen Timoshenko and James N. Goodier. *Theory of Elasticity*. Third. New York: McGraw-Hill, 1970. ISBN: 0070647208.

[39] Vikram S. Deshpande, Norman A. Fleck, and Michael F. Ashby. "Effective properties of the octet-truss lattice material." *Journal of the Mechanics and Physics of Solids* 49.8 (2001), pp. 1747–1769. ISSN: 00225096. DOI: `10.1016/S0022-5096(01)00010-2`.

[40] Oraib Al-Ketan et al. "Microarchitected stretching-dominated mechanical metamaterials with minimal surface topologies." *Advanced Engineering Materials* 20.9 (2018). ISSN: 15272648. DOI: `10.1002/adem.201800029`.

[41] Carlos M. Portela, Julia R. Greer, and Dennis M. Kochmann. "Impact of node geometry on the effective stiffness of non-slender three-dimensional truss lattice architectures." *Extreme Mechanics Letters* 22 (2018), pp. 138–148. ISSN: 23524316. DOI: `10.1016/j.eml.2018.06.004`.

[42] Nandita Biswas et al. "Deformation and fracture behavior of laser processed dense and porous Ti6Al4V alloy under static and dynamic loading." *Materials Science and Engineering A* 549 (2012), pp. 213–221. ISSN: 09215093. DOI: `10.1016/j.msea.2012.04.036`.

[43] Lijun Xiao et al. "Mechanical properties of open-cell rhombic dodecahedron titanium alloy lattice structure manufactured using electron beam melting under dynamic loading." *International Journal of Impact Engineering* 100 (2017), pp. 75–89. ISSN: 0734743X. DOI: `10.1016/j.ijimpeng.2016.10.006`.

[44] Lijun Xiao and Weidong Song. "Additively-manufactured functionally graded Ti-6Al-4V lattice structures with high strength under static and dynamic loading: Experiments." *International Journal of Impact Engineering* 111

(2018), pp. 255–272. ISSN: 0734-743X. DOI: `10.1016/j.ijimpeng.2017.09.018`.

[45] Kavan Hazeli et al. "Microstructure-topology relationship effects on the quasi-static and dynamic behavior of additively manufactured lattice structures." *Materials & Design* 176 (2019), p. 107826. ISSN: 18734197. DOI: `10.1016/j.matdes.2019.107826`.

[46] Thomas Tancogne-Dejean, Adriaan B. Spierings, and Dirk Mohr. "Additively-manufactured metallic micro-lattice materials for high specific energy absorption under static and dynamic loading." *Acta Materialia* 116 (2016), pp. 14–28. ISSN: 13596454. DOI: `10.1016/j.actamat.2016.05.054`.

[47] Lijun Xiao et al. "Mechanical characterization of additively-manufactured metallic lattice structures with hollow struts under static and dynamic loadings." *International Journal of Impact Engineering* 169 (2022), p. 104333. ISSN: 0734-743X. DOI: `10.1016/j.ijimpeng.2022.104333`.

[48] Chen Ling et al. "Mechanical behaviour of additively-manufactured polymeric octet-truss lattice structures under quasi-static and dynamic compressive loading." *Materials and Design* 162 (2019), pp. 106–118. ISSN: 18734197. DOI: `10.1016/j.matdes.2018.11.035`.

[49] Yu Duan et al. "Quasi-static and dynamic compressive properties and deformation mechanisms of 3D printed polymeric cellular structures with Kelvin cells." *International Journal of Impact Engineering* 132 (2019). ISSN: 0734743X. DOI: `10.1016/j.ijimpeng.2019.05.017`.

[50] Stephen R. Reid and C. Peng. "Dynamic uniaxial crushing of wood." *International Journal of Impact Engineering* 19.5-6 (1997), pp. 531–570. ISSN: 0734743X. DOI: `10.1016/s0734-743x(97)00016-x`.

[51] Yongle Sun et al. "Determination of the constitutive relation and critical condition for the shock compression of cellular solids." *Mechanics of Materials* 99 (2016), pp. 26–36. ISSN: 01676636. DOI: `10.1016/j.mechmat.2016.04.004`.

[52] Zhijun Zheng et al. "Dynamic crushing of cellular materials: Continuum-based wave models for the transitional and shock modes." *International Journal of Impact Engineering* 42 (2012), pp. 66–79. ISSN: 0734743X. DOI: `10.1016/j.ijimpeng.2011.09.009`.

[53] Zhenmin Zou et al. "Dynamic crushing of honeycombs and features of shock fronts." *International Journal of Impact Engineering* 36.1 (2009), pp. 165–176. ISSN: 0734743X. DOI: `10.1016/j.ijimpeng.2007.11.008`.

[54] A. T. Barnes et al. "Dynamic crushing of aluminum foams: Part I – Experiments." *International Journal of Solids and Structures* 51.9 (2014), pp. 1631–1645. ISSN: 00207683. DOI: `10.1016/j.ijsolstr.2013.11.019`.

[55] Stavros Gaitanaros and Stelios Kyriakides. "Dynamic crushing of aluminum foams: Part II – Analysis." *International Journal of Solids and Structures* 51.9 (2014), pp. 1646–1661. ISSN: 00207683. DOI: 10.1016/j.ijsolstr.2013.11.020.

[56] James A. Hawreliak et al. "Dynamic behavior of engineered lattice materials." *Scientific Reports* 6 (2016), pp. 1–7. ISSN: 20452322. DOI: 10.1038/srep28094.

[57] Jonathan Lind et al. "In situ dynamic compression wave behavior in additively manufactured lattice materials." *Journal of Materials Research* 34.1 (2019), pp. 2–19. ISSN: 20445326. DOI: 10.1557/jmr.2018.351.

[58] Brittany A. Branch et al. "Detailed meso-scale simulations of the transient deformation in additively manufactured 316 L stainless steel lattices characterized by phase contrast imaging." *International Journal of Impact Engineering* 161 (2022), p. 104112. ISSN: 0734743X. DOI: 10.1016/j.ijimpeng.2021.104112.

[59] Mark C. Messner et al. "Modeling shocks in periodic lattice materials." *AIP Conference Proceedings* 1793 (2017). ISSN: 15517616. DOI: 10.1063/1.4971618.

[60] Carlos M. Portela et al. "Supersonic impact resilience of nanoarchitected carbon." *Nature Materials* (2021). ISSN: 14764660. DOI: 10.1038/s41563-021-01033-z.

[61] John S. Weeks, Vatsa Gandhi, and Guruswami Ravichandran. "Shock compression behavior of stainless steel 316L octet-truss lattice structures." *International Journal of Impact Engineering* 169 (2022), p. 104324. ISSN: 0734-743X. DOI: 10.1016/j.ijimpeng.2022.104324.

[62] PJ Tan et al. "Dynamic compressive strength properties of aluminium foams. Part I – Experimental data and observations." *Journal of the Mechanics and Physics of Solids* 53.10 (2005), pp. 2174–2205. ISSN: 00225096. DOI: 10.1016/j.jmps.2005.05.007.

[63] PJ Tan et al. "Dynamic compressive strength properties of aluminium foams. Part II – 'Shock' theory and comparison with experimental data and numerical models." *Journal of the Mechanics and Physics of Solids* 53.10 (2005), pp. 2206–2230. ISSN: 00225096. DOI: 10.1016/j.jmps.2005.05.003.

[64] Sergey L. Lopatnikov et al. "High-velocity plate impact of metal foams." *International Journal of Impact Engineering* 30.4 (2004), pp. 421–445. ISSN: 0734743X. DOI: 10.1016/S0734-743X(03)00066-6.

[65] Lee Davison. *Fundamentals of Shock Wave Propagation in Solids*. Shock Wave and High Pressure Phenomena. Berlin, Heidelberg: Springer Berlin Heidelberg, 2008. ISBN: 978-3-540-74568-6. DOI: 10.1007/978-3-540-74569-3.

[66] Lis Mosekilde. "Consequences of the remodelling process for vertebral trabecular bone structure: A scanning electron microscopy study (uncoupling of unloaded structures)." *Bone and Mineral* 10.1 (1990), pp. 13–35. ISSN: 01696009. DOI: `10.1016/0169-6009(90)90046-I`.

[67] Yasuaki Seki, Matthew S. Schneider, and Marc A. Meyers. "Structure and mechanical behavior of a toucan beak." *Acta Materialia* 53.20 (2005), pp. 5281–5296. ISSN: 13596454. DOI: `10.1016/j.actamat.2005.04.048`.

[68] Li Zhen Wang, Hong Quan Zhang, and Yubo Fan. "Comparative study of the mechanical properties, micro-structure, and composition of the cranial and beak bones of the great spotted woodpecker and the lark bird." *Science China Life Sciences* 54.11 (2011), pp. 1036–1041. ISSN: 16747305. DOI: `10.1007/s11427-011-4242-2`.

[69] Tobias A. Schaedler et al. "Ultralight metallic microlattices." *Science* 334.6058 (2011), pp. 962–965. ISSN: 10959203. DOI: `10.1126/science.1211649`.

[70] Jens Bauer et al. "High-strength cellular ceramic composites with 3D microarchitecture." *Proceedings of the National Academy of Sciences of the United States of America* 111.7 (2014), pp. 2453–2458. ISSN: 00278424. DOI: `10.1073/pnas.1315147111`.

[71] Lauren C. Montemayor et al. "Insensitivity to Flaws Leads to Damage Tolerance in Brittle Architected Meta-Materials." *Scientific Reports* 6.February (2016), pp. 1–9. ISSN: 20452322. DOI: `10.1038/srep20570`.

[72] Xuan Zhang et al. "Lightweight, flaw-tolerant, and ultrastrong nanoarchitected carbon." *Proceedings of the National Academy of Sciences of the United States of America* 116.14 (2019), pp. 6665–6672. ISSN: 10916490. DOI: `10.1073/pnas.1817309116`.

[73] Lu Liu et al. "Elastic and failure response of imperfect three-dimensional metallic lattices: the role of geometric defects induced by Selective Laser Melting." *Journal of the Mechanics and Physics of Solids* 107 (2017), pp. 160–184. ISSN: 00225096. DOI: `10.1016/j.jmps.2017.07.003`.

[74] Andrew Gross et al. "Correlation between topology and elastic properties of imperfect truss-lattice materials." *Journal of the Mechanics and Physics of Solids* 124 (2019), pp. 577–598. ISSN: 00225096. DOI: `10.1016/j.jmps.2018.11.007`.

[75] Lucas R. Meza et al. "Reexamining the mechanical property space of three-dimensional lattice architectures." *Acta Materialia* 140 (2017), pp. 424–432. ISSN: 13596454. DOI: `10.1016/j.actamat.2017.08.052`.

[76] J. Jefferson Andrew, Pawan Verma, and Shanmugam Kumar. "Impact behavior of nanoengineered, 3D printed plate-lattices." *Materials and Design* 202 (2021), p. 109516. ISSN: 18734197. DOI: `10.1016/j.matdes.2021.109516`.

[77] Roy M. Sullivan, Louis J. Ghosn, and Bradley A. Lerch. "A general tetrakaidec-ahedron model for open-celled foams." *International Journal of Solids and Structures* 45.6 (2008), pp. 1754–1765. ISSN: 00207683. DOI: `10.1016/j.ijsolstr.2007.10.028`.

[78] Kaliat T. Ramesh. "High strain rate and impact mechanics." *Handbook of Experimental Solid Mechanics* (2008), pp. 929–960. DOI: `10.1007/978-0-387-30877-7_33`.

[79] Christophe Bacon. "An experimental method for considering dispersion and attenuation in a viscoelastic Hopkinson bar." *Experimental Mechanics* 38.4 (1998), pp. 242–249. ISSN: 0014-4851. DOI: `10.1177/001448519803800402`.

[80] Neal R. Brodnik et al. "Guiding and trapping cracks with compliant inclusions for enhancing toughness of brittle composite materials." *Journal of Applied Mechanics* 87.3 (2020). ISSN: 0021-8936. DOI: `10.1115/1.4045682`.

[81] Clive R. Siviour and Jennifer L. Jordan. "High strain rate mechanics of polymers: A review." *Journal of Dynamic Behavior of Materials* 2.1 (2016), pp. 15–32. ISSN: 21997454. DOI: `10.1007/s40870-016-0052-8`.

[82] Dong Ruan et al. "In-plane dynamic crushing of honeycombs—a finite element study." *International Journal of Impact Engineering* 28.2 (2003), pp. 161–182. DOI: `10.1016/S0734-743X(02)00056-8`.

[83] Tobias Maconachie et al. "SLM lattice structures: Properties, performance, applications and challenges." *Materials and Design* 183 (2019), p. 108137. ISSN: 18734197. DOI: `10.1016/j.matdes.2019.108137`.

[84] Xueyang Li et al. "Rate- and temperature-dependent plasticity of additively manufactured stainless steel 316L: Characterization, modeling and application to crushing of shell-lattices." *International Journal of Impact Engineering* 145 (2020), p. 103671. ISSN: 0734743X. DOI: `10.1016/j.ijimpeng.2020.103671`.

[85] Xiu Yun Yap et al. "Mechanical properties and failure behaviour of architected alumina microlattices fabricated by stereolithography 3D printing." *International Journal of Mechanical Sciences* 196 (2021), p. 106285. ISSN: 00207403. DOI: `10.1016/j.ijmecsci.2021.106285`.

[86] Jens Bauer et al. "Approaching theoretical strength in glassy carbon nanolattices." *Nature Materials* 15.4 (2016), pp. 438–443. ISSN: 14764660. DOI: `10.1038/nmat4561`.

[87] Yanchu Zhang et al. "Mechanics of stretchy elastomer lattices." *Journal of the Mechanics and Physics of Solids* 159 (2022), p. 104782. ISSN: 00225096. DOI: `10.1016/j.jmps.2022.104782`.

[88] Eric C. Clough et al. "Elastomeric microlattice impact attenuators." *Matter* 1.6 (2019), pp. 1519–1531. ISSN: 25902385. DOI: `10.1016/j.matt.2019.10.004`.

[89] Yaodong Liu et al. "A numerical study on the rate sensitivity of cellular metals." *International Journal of Solids and Structures* 46.22-23 (2009), pp. 3988–3998. ISSN: 00207683. DOI: `10.1016/j.ijsolstr.2009.07.024`.

[90] Ronald E. Winter et al. "Plate-impact loading of cellular structures formed by selective laser melting." *Modelling and Simulation in Materials Science and Engineering* 22.2 (2014). ISSN: 1361651X. DOI: `10.1088/0965-0393/22/2/025021`.

[91] Sheng-Nian Luo et al. "Gas gun shock experiments with single-pulse x-ray phase contrast imaging and diffraction at the Advanced Photon Source." *Review of Scientific Instruments* 83.7 (2012), p. 073903. DOI: `10.1063/1.4733704`.

[92] Hubert Schreier, Jean-José Orteu, Michael A. Sutton, et al. *Image correlation for shape, motion and deformation measurements: Basic concepts, theory and applications*. Vol. 1. Springer, 2009. ISBN: 978-0-387-78747-3. DOI: `10.1007/978-0-387-78747-3`.

[93] Suraj Ravindran et al. "Experimental characterization of compaction wave propagation in cellular polymers." *International Journal of Solids and Structures* 139-140 (2018), pp. 270–282. ISSN: 00207683. DOI: `10.1016/j.ijsolstr.2018.02.003`.

[94] Patrick Köhnen et al. "Mechanical properties and deformation behavior of additively manufactured lattice structures of stainless steel." *Materials and Design* 145 (2018), pp. 205–217. ISSN: 18734197. DOI: `10.1016/j.matdes.2018.02.062`.

[95] John S. Weeks and Guruswami Ravichandran. "High strain-rate compression behavior of polymeric rod and plate Kelvin lattice structures." *Mechanics of Materials* 166 (2022), p. 104216. ISSN: 01676636. DOI: `10.1016/j.mechmat.2022.104216`.

[96] William D. Callister, David G. Rethwisch, et al. *Materials science and engineering: An introduction*. Vol. 10. Wiley New York, 2018. ISBN: 9781119405436.

[97] Zuhal Ozdemir et al. "Energy absorption in lattice structures in dynamics: Nonlinear FE simulations." *International Journal of Impact Engineering* 102 (2017), pp. 1–15. ISSN: 0734743X. DOI: `10.1016/j.ijimpeng.2016.11.016`.

[98] Jochen Mueller et al. "Energy absorption properties of periodic and stochastic 3D lattice materials." *Advanced Theory and Simulations* 2.10 (2019), pp. 1–11. ISSN: 25130390. DOI: `10.1002/adts.201900081`.

[99] Nan Jin et al. "Failure and energy absorption characteristics of four lattice structures under dynamic loading." *Materials and Design* 169 (2019), p. 107655. ISSN: 18734197. DOI: `10.1016/j.matdes.2019.107655`.

[100] John J. Harrigan, Stephen R. Reid, and Ali Seyed Yaghoubi. "The correct analysis of shocks in a cellular material." *International Journal of Impact Engineering* 37.8 (2010), pp. 918–927. ISSN: 0734743X. DOI: `10.1016/j.ijimpeng.2009.03.011`.

[101] Stavros Gaitanaros and Stelios Kyriakides. "On the effect of relative density on the crushing and energy absorption of open-cell foams under impact." *International Journal of Impact Engineering* 82 (2015), pp. 3–13. ISSN: 0734743X. DOI: `10.1016/j.ijimpeng.2015.03.011`.

[102] Dana M. Dattelbaum and Joshua D. Coe. "Shock-driven decomposition of polymers and polymeric foams." *Polymers* 11.3 (2019), pp. 1–23. ISSN: 20734360. DOI: `10.3390/polym11030493`.

[103] Brittany A. Branch et al. "A comparison of shockwave dynamics in stochastic and periodic porous polymer architectures." *Polymer* 160 (2019), pp. 325–337. ISSN: 00323861. DOI: `10.1016/j.polymer.2018.10.074`.

[104] Jonathan Lind, Andrew K. Robinson, and Mukul Kumar. "Insight into the coordinated jetting behavior in periodic lattice structures under dynamic compression." *Journal of Applied Physics* 128.1 (2020). ISSN: 10897550. DOI: `10.1063/5.0003776`.

[105] Stephen W. Hughes. "Archimedes revisited: A faster, better, cheaper method of accurately measuring the volume of small objects." *Physics Education* 40.5 (2005), pp. 468–474. ISSN: 00319120. DOI: `10.1088/0031-9120/40/5/008`.

[106] Caroline A. Schneider, Wayne S. Rasband, and Kevin W. Eliceiri. "NIH Image to ImageJ: 25 years of image analysis." *Nature Methods* 9.7 (2012), pp. 671–675. ISSN: 15487091. DOI: `10.1038/nmeth.2089`.

[107] Zhongji Sun et al. "Simultaneously enhanced strength and ductility for 3D-printed stainless steel 316L by selective laser melting." *NPG Asia Materials* 10.4 (2018), pp. 127–136. ISSN: 18844057. DOI: `10.1038/s41427-018-0018-5`.

[108] Gordon R. Johnson and William H. Cook. "Fracture characteristics of three metals subjected to various strains, strain rates, temperatures and pressures." *Engineering Fracture Mechanics* 21.1 (1985), pp. 31–48. ISSN: 00137944. DOI: `10.1016/0013-7944(85)90052-9`.

[109] Philip D. Harvey. *Engineering properties of steel*. American Society for Metals (ASM), 1982. ISBN: 9780871701442.

[110] Domenico Umbrello, Rachid M'Saoubi, and José C. Outeiro. "The influence of Johnson-Cook material constants on finite element simulation of machining of AISI 316L steel." *International Journal of Machine Tools and Manufacture* 47.3-4 (2007), pp. 462–470. ISSN: 08906955. DOI: `10.1016/j.ijmachtools.2006.06.006`.

[111] Pawel Platek et al. "Investigations on mechanical properties of lattice structures with different values of relative density made from 316L by selective laser melting (SLM)." *Materials* 13.9 (2020). ISSN: 19961944. DOI: `10.3390/ma13092204`.

[112] Ganesh U. Patil and Kathryn H. Matlack. "Effective property evaluation and analysis of three-dimensional periodic lattices and composites through Bloch-wave homogenization." *The Journal of the Acoustical Society of America* 145.3 (2019), pp. 1259–1269. ISSN: 0001-4966. DOI: `10.1121/1.5091690`.

[113] Brittany Branch et al. "Controlling shockwave dynamics using architecture in periodic porous materials." *Journal of Applied Physics* 121.13 (2017). ISSN: 10897550. DOI: `10.1063/1.4978910`.

[114] Sangryun Lee, Zhizhou Zhang, and Grace X. Gu. "Generative machine learning algorithm for lattice structures with superior mechanical properties." *Materials Horizons* 9.3 (2022), pp. 952–960. ISSN: 20516355. DOI: `10.1039/d1mh01792f`.

[115] Jan Hendrik Bastek et al. "Inverting the structure–property map of truss metamaterials by deep learning." *Proceedings of the National Academy of Sciences of the United States of America* 119.1 (2022). ISSN: 10916490. DOI: `10.1073/pnas.2111505119`.

[116] Cihan Tekoğlu et al. "Size effects in foams: Experiments and modeling." *Progress in Materials Science* 56.2 (2011), pp. 109–138. ISSN: 00796425. DOI: `10.1016/j.pmatsci.2010.06.001`.

[117] Marcus Yoder, Lonny Thompson, and Joshua Summers. "Size effects in lattice structures and a comparison to micropolar elasticity." *International Journal of Solids and Structures* 143 (2018), pp. 245–261. ISSN: 00207683. DOI: `10.1016/j.ijsolstr.2018.03.013`.

Appendix A

A.1   3D Printer Manufacturing Parameters

Table A.1: Autodesk Ember DLP 3D Printer parameters used for manufacturing polymeric lattice structure specimens in Chapters 2 and 3.

Wait time (before exposure) [s]	Exposure time [s]	Layer thickness [μm]
1.5	2.8	25
Separation slide velocity [rpm]	*Approach slide velocity* [rpm]	*Angle of rotation* [deg]
8.0	12.0	60.0
Separation Z-axis velocity [mm/s]	*Approach Z-axis velocity* [mm/s]	*Z-axis overlift* [mm]
1.5	1.5	0.75
Overpress [mm]	*Separation slide maximum jerk* $[deg/s^2 (x10^3)]$	
0.0	4630	

A.2   Viscoelastic Parameters for Polycarbonate SHPB Correction

Wave propagation coefficient, $\gamma(\omega)$, as a function of frequency (ω) used for dispersion and attenuation corrections of viscoelastic strain measurements of the polycarbonate split-Hopkinson (Kolsky) pressure bar (SHPB) system used in this thesis. $\gamma(\omega)$ can be decomposed into the attenuation coefficient, $\alpha(\omega)$, and phase velocity, $c(\omega)$, as in Eq. (2.3) and may be experimentally determined using a one-point measurement technique [79]. Figure A.1 shows the experimental results and average values of $\alpha(\omega)$ and $c(\omega)$. Strains and striker velocities of wave propagation coefficient experiments were comparable to that of high strain-rate experiments on lattice specimens.
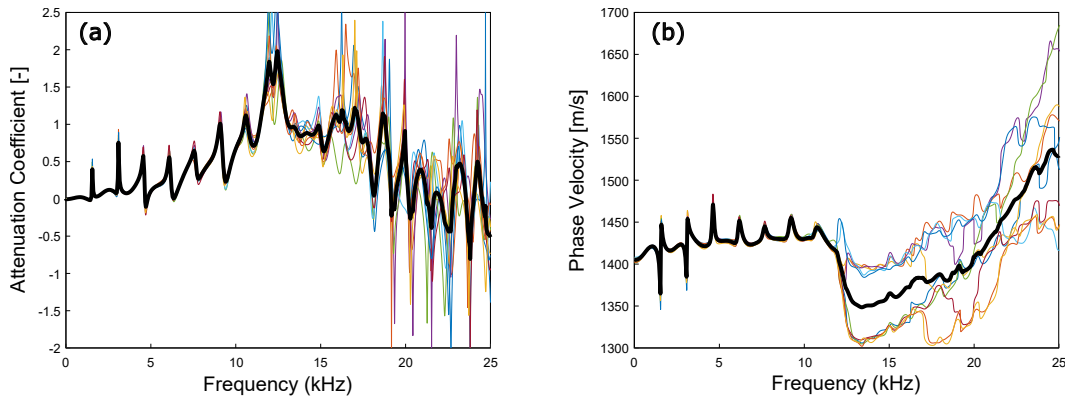

Figure A.1: Wave propagation coefficient for the polycarbonate SHPB system realized through (a) attenuation coefficient, $\alpha(\omega)$, and (b) phase velocity, $c(\omega)$, as a function of frequency, ω. The dark solid lines represent the averaged value of the measurements.

A p p e n d i x   B

SUPPLEMENTARY VIDEOS

The following supplementary videos are included:

Chapter 2:

Supplementary Video S1: Low strain-rate experimental deformation videos of rod-like and plate-like photopolymer lattice structures coupled with instantaneous stress-strain response.

Supplementary Video S2: High strain-rate experimental deformation videos of rod-like and plate-like photopolymer lattice structures coupled with instantaneous stress-strain response.

Chapter 4:

Supplementary Video S3: Full-field deformation videos for shock compression experiments on stainless steel 316L octet-truss lattice structures ($\#OT10_2$, $\#OT15_2$, and $\#OT30_1$) and the corresponding numerical simulations.

Supplementary Video S4: Full-field deformation video of shock compression experiment on stainless steel 316L octet-truss lattice structure ($\#OT15_2$) with relevant wave front positions marked and tracked.